

Characterization of Porous Solids and Powders: Surface Area, Pore Size and Density

by

S. LOWELL

Quantachrome Instruments, Boynton Beach, U.S.A.

JOAN E. SHIELDS

C.W. Post Campus of Long Island University, U.S.A.

MARTIN A. THOMAS

Quantachrome Instruments, Boynton Beach, U.S.A.

and

MATTHIAS THOMMES

Quantachrome Instruments, Boynton Beach, U.S.A.



KLUWER ACADEMIC PUBLISHERS

DORDRECHT / BOSTON / LONDON

A C.I.P. Catalogue record for this book is available from the Library of Congress.

ISBN 1-4020-2302-2 (HB)
ISBN 1-4020-2303-0 (e-book)

Published by Kluwer Academic Publishers,
P.O. Box 17, 3300 AA Dordrecht, The Netherlands.

Sold and distributed in North, Central and South America
by Kluwer Academic Publishers,
101 Philip Drive, Norwell, MA 02061, U.S.A.

In all other countries, sold and distributed
by Kluwer Academic Publishers,
P.O. Box 322, 3300 AH Dordrecht, The Netherlands.

Printed on acid-free paper

All Rights Reserved

© 2004 Kluwer Academic Publishers

No part of this work may be reproduced, stored in a retrieval system, or transmitted in any form or by any means, electronic, mechanical, photocopying, microfilming, recording or otherwise, without written permission from the Publisher, with the exception of any material supplied specifically for the purpose of being entered and executed on a computer system, for exclusive use by the purchaser of the work.

Printed in the Netherlands.

STATE COLLEGE
UNIVERSITY LIBRARY

Contents

PART 1 THEORETICAL

1 Introduction

1.1	Real Surfaces	1
1.2	Factors Affecting Surface area	1
1.3	Surface Area from Particle Size Distributions	3
1.4	References	4

2 Gas Adsorption

2.1	Introduction	5
2.2	Physical and Chemical Adsorption	6
2.3	Physical Adsorption Forces	7
2.4	Physical Adsorption on a Planar Surface	8
2.5	References	10

3 Adsorption Isotherms

3.1	Pore Size and Adsorption Potential	11
3.2	Classification of Adsorption Isotherms	12
3.3	References	14

4 Adsorption Mechanism

4.1	Langmuir and BET Theories (Kinetic Isotherms)	15
4.1.1	The Langmuir Isotherm	15
4.1.2	The Brunauer, Emmett, and Teller (BET) Theory	18
4.2	The Frenkel-Halsey-Hill (FHH) Theory of Multilayer Adsorption	24
4.3	Adsorption in Microporous Materials	26
4.3.1	Introduction	26
4.3.2	Aspects of Classical, Thermodynamic Theories for Adsorption in Micropores: Extension of Polanyi's Theory	29
4.3.3	Aspects of Modern, Microscopic Theories for Adsorption in Micropores: Density Functional Theory and Molecular Simulation	33
4.3.3.1	Density Functional Theory (DFT)	34
4.3.3.2	Computer Simulation Studies: Monte Carlo Simulation and Molecular Dynamics	35

4.3.3.3	NLDFT and Monte Carlo Simulation for Pore Size Analysis	36
4.4	Adsorption in Mesopores	37
4.4.1	Introduction	37
4.4.2	Multilayer Adsorption, Pore Condensation and Hysteresis	37
4.4.3	Pore Condensation: Macroscopic, Thermodynamic Approaches	40
4.4.3.1	Classical Kelvin Equation	40
4.4.3.2	Modified Kelvin Equation	42
4.4.4	Adsorption Hysteresis	43
4.4.4.1	Classification of Hysteresis Loops	43
4.4.4.2	Origin of Hysteresis	45
4.4.5	Effects of Temperature and Pore Size: Experiments and Predictions of Modern, Microscopic Theories	49
4.5	References	55
5	Surface Area from the Langmuir and BET Theories	
5.1	Specific Surface Area from the Langmuir Equation	58
5.2	Specific Surface Area from the BET Equation	59
5.2.1.	BET-Plot and Calculation of the Specific Surface Area	59
5.2.2	The Meaning of Monolayer Coverage	60
5.2.3	The BET Constant and Site Occupancy	61
5.2.4	The Single Point BET Method	62
5.2.5	Comparison of the Single Point and Multipoint Methods	63
5.2.6	Applicability of the BET Theory	67
5.2.7	Importance of the Cross-Sectional Area	71
5.2.8	Nitrogen as the Standard Adsorptive for Surface Area Measurements	78
5.2.9	Low Surface Area Analysis	79
5.3	References	80
6	Other Surface Area Methods	
6.1	Introduction	82
6.2	Gas Adsorption: Harkins and Jura Relative Method	82
6.3	Immersion Calorimetry: Harkins and Jura Absolute Method	85
6.4	Permeametry	86
6.5	References	92

7	Evaluation of the Fractal Dimension by Gas Adsorption	
7.1	Introduction	94
7.2	Method of Molecular Tiling	94
7.3	The Frenkel-Halsey-Hill Method	95
7.4	The Thermodynamic Method	96
7.5	Comments About Fractal Dimensions Obtained from Gas Adsorption	97
7.6	References	100
8	Mesopore Analysis	
8.1	Introduction	101
8.2	Methods based on the Kelvin equation	101
8.3	Modelless Pore Size Analysis	109
8.4	Total Pore Volume and Average Pore Size	111
8.5	Classical, Macroscopic Thermodynamic Methods versus Modern, Microscopic Models for Pore Size Analysis	112
8.6	Mesopore Analysis and Hysteresis	117
8.6.1	Use of Adsorption or Desorption Branch for Pore Size Calculation?	117
8.6.2	Lower Limit of the Hysteresis Loop- Tensile Strength Hypothesis	121
8.7	Adsorptives other than Nitrogen for Mesopore Analysis	123
8.8	References	126
9	Micropore Analysis	
9.1	Introduction	129
9.2	Micropore Analysis by Isotherm Comparison	129
9.2.1	Concept of V-t curves	129
9.2.2	The t- Method	130
9.2.3	The α_s method	139
9.3	The Micropore Analysis (MP) Method	140
9.4	Total Micropore Volume and Surface Area	143
9.5	The Dubinin-Radushkevich (DR) Method	143
9.6	The Horvath-Kawazoe (HK) Approach and Related Methods	145
9.7	Application of NLDFT: Combined Micro/Mesopore Analysis With a Single Method	148
9.8	Adsorptives other than Nitrogen for Super- and Ultramicroporosimetry	152
9.9	References	154

10	Mercury Porosimetry: Non-Wetting Liquid Penetration	
10.1	Introduction	157
10.2	Young-Laplace Equation	158
10.3	Contact Angles and Wetting	160
10.4	Capillarity	162
10.5	The Washburn Equation	164
10.6	Intrusion – Extrusion Curves	166
10.7	Common Features of Porosimetry Curves	170
10.8	Hysteresis, Entrapment and Contact Angle	171
10.9	Contact Angle Changes	173
10.10	Porosimetric Work	175
10.12	Theory of Porosimetry Hysteresis	177
10.13	Pore Potential	179
10.14	Other Hysteresis Theories (Throat-Pore Ratio Network Model)	182
10.15	Equivalency of Mercury Porosimetry and Gas Sorption	184
10.16	References	187
11	Pore Size and Surface Characteristics of Porous Solids by Mercury Porosimetry	
11.1	Application of The Washburn Equation	189
11.2	Pore Size and Pore Size Distribution from Mercury Porosimetry	190
11.2.1	Linear Pore Volume Distribution	190
11.2.2	Logarithmic Pore Volume Distribution	192
11.2.3	Pore Number Distributions	194
11.2.4	Pore Length Distribution	194
11.2.5	Pore Population (Number Distribution)	195
11.2.6	Surface Area and Surface Area Distribution from Intrusion Curves	196
11.2.7	Pore Area Distributions	197
11.3	Pore Shape from Hysteresis	197
11.4	Fractal Dimension	197
11.5	Permeability	200
11.6	Tortuosity	202
11.7	Particle Size Distribution	204
11.7.1	Mayer & Stowe Approach	204
11.7.2	Smith & Stermer Approach	206
11.8	Comparison of Porosimetry and Gas Sorption	208
11.9	Solid Compressibility	210
11.10	References	212

12 Chemisorption: Site Specific Gas Adsorption

12.1	Chemical Adsorption	213
12.2	Quantitative Measurements	218
12.3	Stoichiometry	218
12.4	Monolayer Coverage	220
12.4.1	Extrapolation	220
12.4.2	Irreversible Isotherm and Bracketing	220
12.4.3	Langmuir Theory	221
12.4.4	Temperature Dependent Models	223
12.4.5	Temkin Method	223
12.4.6	Freundlich Method	226
12.4.7	Isotherm Subtraction – Accessing Spillover	227
12.4.8	Surface Titration	227
12.5	Active Metal Area	228
12.6	Dispersion	229
12.7	Crystallite (Nanoparticle) Size	229
12.8	Heats of Adsorption and Activation Energy	230
12.8.1	Differential Heats of Adsorption	230
12.8.2	Integral Heat of Adsorption	231
12.8.3	Activation Energy	231
12.9	References	232

PART 2 EXPERIMENTAL**13 Physical Adsorption Measurements – Preliminaries**

13.1	Experimental Techniques for Physical Adsorption Measurements	234
13.2	Reference Standards	235
13.3	Representative Samples	236
13.4	Sample Conditioning: Outgassing of the Adsorbent	238
13.5	Elutriation and Its Prevention	240
13.6	References	240

14 Vacuum Volumetric Measurements (Manometry)

14.1	Basics of Volumetric Adsorption Measurement	242
14.2	Deviations from Ideality	245
14.3	Void Volume Determination	246
14.4	Coolant Level and Temperature Control	247

14.5	Saturation Vapor Pressure, P_0 and Temperature of the Sample Cell	248
14.6	Sample Cells	250
14.7	Low Surface Area	250
14.8	Micro- and Mesopore Analysis	251
14.8.1	Experimental Requirements	251
14.8.2	Micropore Analysis and Void Volume Determination	252
14.8.3	Thermal Transpiration Correction	253
14.8.4	Adsorptives other than Nitrogen for Micro- and Mesopore Analysis - Experimental Aspects	254
14.9	Automated Instrumentation	256
14.9.1	Multistation Sorption Analyzer	256
14.9.2	The NOVA Concept	257
14.10	References	258
15	Dynamic Flow Method	
15.1	Nelson and Eggertsen Continuous Flow Method	260
15.2	Carrier Gas (Helium) and Detector Sensitivity	262
15.3.	Design Parameters for Continuous Flow Apparatus	266
15.4	Signals and Signal Calibration	270
15.5	Adsorption and Desorption Isotherms by Continuous Flow	273
15.6	Low Surface Areas Measurement	276
15.7	Data Reduction - Continuous Flow Method	279
15.8	Single Point Method	280
15.9	References	282
16	Volumetric Chemisorption: Catalyst Characterization by Static Methods	
16.1	Applications	283
16.2	Sample Requirements	283
16.3	General Description of Equipment	284
16.4	Measuring System	285
16.4.1	Pressure Measurement	286
16.4.2	Valves	286
16.4.3	Vacuum	287
16.4.4	Sample Cell	287
16.4.5	Heating System	287
16.4.6	Gases and Chemical Compatibilities	288
16.5	Pretreatment	289
16.5.1	Heating	289
16.5.2	Atmosphere	290
16.6	Isotherms	292

16.6.1	Reactive Gas	292
16.6.2	The Combined Isotherm	293
16.6.3	The Weak Isotherm	295
16.6.4	The Strong Isotherm	295
16.6.5	Multiple Isotherms	295
16.7	References	295

17 Dynamic Chemisorption: Catalyst Characterization By Flow Techniques

17.1	Applications	297
17.2	Sample Requirements	297
17.3	General Description of Equipment	297
17.3.1	Flow Path	298
17.3.2	Sample Cell	299
17.3.3	Gases	299
17.3.4	Heating	300
17.3.5	Pulse Injection	300
17.3.6	Detector	300
17.4	Pretreatment	301
17.5	Pulse Titration	301
17.6	Additional Requirements for Temperature Programmed Methods	303
17.6.1	Programmed Heating	303
17.6.2	Sample Temperature	304
17.7	Temperature Programmed Reduction	304
17.8	Temperature Programmed Oxidation	305
17.9	Temperature Programmed Desorption	306
17.9.1	Some Specific Applications	306
17.8.1.1	Acid/Base	306
17.8.1.2	Oxidizers	307
17.8.1.3	Reducers	308
17.10	Mass Spectrometry	308
17.11	Metal Parameters	309
17.11	References	309

18 Mercury Porosimetry: Intra and Inter-Particle Characterization

18.1	Applications	311
18.2	Working with Mercury	311
18.3	Experimental Requirements	312
18.4	Sample Cell	312
18.5	Volume Measurement	313

18.6	Contact Angle	313
18.6.1	Dynamic Contact Angle	314
18.6.2	Static Contact Angle	316
18.7	A Modern Porosimeter	318
18.8	Low Pressure Measurements	318
18.8.1	Sample Cell Evacuation	319
18.8.2	Filling with Mercury	319
18.8.3	Low Pressure Intrusion-Extrusion	319
18.9	High Pressure Measurements	320
18.10	Scanning Method	321
18.11	Stepwise Method	322
18.12	Mercury Entrapment	322
18.13	Working with Powders	323
18.14	Inter/Intra Particle Porosity	324
18.15	Isostatic Crush Strength	324
18.16	References	325
19	Density Measurement	
19.1	Introduction	326
19.2	True Density	326
19.3	Apparent Density	330
19.4	Open-Closed Porosity	330
19.5	Bulk Density	331
19.6	Tap Density	331
19.7	Envelope or Geometric Density	332
19.8	Effective Density	333
19.9	Density by Mercury Porosimetry	333
19.10	Standard Methods	337
19.11	References	338
Index		339

1 Introduction

1.1 REAL SURFACES

There is a convenient mathematical idealization which asserts that a cube of edge length, ℓ cm, possesses a surface area of $6\ell^2$ cm² and that a sphere of radius r cm exhibits $4\ell r^2$ cm² of surface. In reality, however, mathematical, perfect or ideal geometric forms are unattainable since under microscopic examinations all real surfaces exhibit flaws. For example, if a 'super microscope' were available one would observe surface roughness due not only to voids, pores, steps, and other surface imperfections but also due to the atomic or molecular orbitals at the surface. These surface irregularities will always create a real surface area greater than the corresponding theoretical area.

1.2 FACTORS AFFECTING SURFACE AREA

When a cube, real or imaginary, of one meter edge length is subdivided into smaller cubes each one micrometer (10^{-6} meter) in length there will be formed 10^{18} particles, each exposing an area of 6×10^{12} square meters (m²). Thus, the total area of all the particles is 6×10^6 m². This million-fold increase in exposed area is typical of the large surface areas exhibited by fine powders when compared to undivided material. Whenever matter is divided into smaller particles, new surfaces must be produced with a corresponding increase in surface area.

In addition to particle size, the particle shape contributes to the surface area of the powder. Of all geometric forms, a sphere exhibits the minimum area-to-volume ratio while a chain of atoms, bonded only along the chain axis, will give the maximum area-to-volume ratio. All particulate matter possesses geometry and, therefore, surface areas between these two extremes. The dependence of surface area on particle shape is readily shown by considering two particles of the same composition and of equal mass, M , one particle a cube of edge length ℓ and the other spherical with radius r . Since the particle density, ρ , is independent of particle shape[†] one can write

[†] For sufficiently small particles the density can vary slightly with changes in the area to volume ratio. This is especially true if particles are ground to size and atoms near the surface are disturbed from their equilibrium position.

$$M_{cube} = M_{sphere} \quad (1.1)$$

$$(V\rho)_{cube} = (V\rho)_{sphere} \quad (1.2)$$

$$\ell_{cube}^3 = \frac{4}{3}\pi r_{sphere}^3 \quad (1.3)$$

$$\frac{S_{cube}\ell_{cube}}{6} = S_{sphere} \frac{r_{sphere}}{3} \quad (1.4)$$

$$\frac{S_{cube}}{S_{sphere}} = \frac{2r_{sphere}}{\ell_{cube}} \quad (1.5)$$

Thus, for particles of equal weight, the cubic area, S_{cubes} , will exceed the spherical area, S_{sphere} , by a factor of $2r/\ell$.

The range of specific surface area[‡] can vary widely depending upon the particle's size, shape, and porosity.[§] The influence of pores can often overwhelm the size and external shape factors. For example, a powder consisting of spherical particles exhibits a total surface area, S_t , as described by equation (1.6):

$$S_t = 4\pi(r_1^2 N_1 + r_2^2 N_2 + \dots + r_i^2 N_i) = 4\pi \sum_{i=1} r_i^2 N_i \quad (1.6)$$

where r_i and N_i are the average radii and numbers of particles respectively in the size range i . The volume of the same powder sample is

$$V = \frac{4}{3}\pi(r_1^3 N_1 + r_2^3 N_2 + \dots + r_i^3 N_i) = \frac{4}{3}\pi \sum_{i=1} r_i^3 N_i \quad (1.7)$$

Replacing V in equation (1.7) by the ratio of mass to density, M/ρ , and dividing equation (1.6) by (1.7) gives the specific surface area

$$S = \frac{S_t}{M} = \frac{3 \sum_i N_i r_i^2}{\rho \sum_i N_i r_i^3} \quad (1.8)$$

For spheres of uniform radius equation (1.8) becomes

[‡] The area exposed by one gram of powder is called the 'specific surface area'.

[§] Porosity is defined here as surface features that are deeper than they are wide.

$$S = \frac{3}{\rho r} \quad (1.9)$$

Thus, powders consisting of spherical particles of 0.1 micrometer (μm) radius with densities near 3 g cm^{-3} will exhibit surface areas about $10^5 \text{ cm}^2 \text{ g}^{-1}$ ($10 \text{ m}^2 \text{ g}^{-1}$). Similar particles with radii of $1.0 \mu\text{m}$ would exhibit a tenfold decrease in surface area. However, if the same $1.0 \mu\text{m}$ radius particles contained extensive porosity they could exhibit specific surface areas well in excess of $1,000 \text{ m}^2 \text{ g}^{-1}$. This clearly indicates the significant contribution that pores can make to the surface area.

1.3 SURFACE AREA FROM PARTICLE SIZE DISTRIBUTIONS

Although particles can assume all regular geometric shapes, and in most instances highly irregular shapes, most particle size measurements are based on the so-called 'equivalent spherical diameter'. This is the diameter of a sphere that would behave in the same manner as the test particle being measured in the same instrument. For example, the electrical sensing zone method [1] is a commonly used technique for determining particle sizes. Its principle is based on the momentary increase in the resistance of an electrolyte solution that results when a particle passes through a narrow aperture between two electrodes. The resistance change is registered in the electronics as a rapid pulse. The pulse height is proportional to the particle volume and therefore, the particles are sized as equivalent spheres.

Stokes' law [2] is another concept around which several instruments are designed to give particle size or size distributions. Stokes' law is used to determine the settling velocity of particles in a fluid medium as a function of their size. Equation (1.10) is a useful form of Stokes' law

$$D = \sqrt{\frac{18\eta v}{(\rho_s - \rho_f)g}} \quad (1.10)$$

where D is the particle diameter, η is the coefficient of viscosity, v is the settling velocity, g is the gravitational constant, and ρ_s and ρ_f are the densities of the solid and the fluid, respectively. Allen [3] gives an excellent discussion of the various experimental methods associated with sedimentation size analysis. Regardless of the experimental method employed, nonspherical particles will be measured as larger or smaller equivalent spheres depending on whether the particles settle faster or more

slowly than spheres of the same mass. Modifications of Stokes' law have been used in centrifugal devices to enhance the settling rates but are subject to the same limitations of yielding only the equivalent spherical diameter.

Optical devices, based upon particle attenuation of a light beam or measurement of scattering angles and intensity, also give equivalent spherical diameters.

Permeametric methods, discussed in chapter 6, are often used to determine average particle size. The method is based upon the impedance offered to the fluid flow by a packed bed of powder. Again, equivalent spherical diameter is the calculated size.

Sieving is another technique that sizes particles according to their smallest dimension but gives no information on particle shape.

Electron microscopy techniques can be used to estimate particle shape. A limitation is that only relatively few particles can be viewed.

Attempts to measure surface area based on any of the above methods will give results significantly less than the true value, in some cases by factors of 10^3 or greater depending upon particle shape, surface irregularities and porosity. At best, surface areas calculated from particle size will establish the lower limit by the implicit assumptions of sphericity or some other regular geometric shape, and by ignoring the highly irregular nature of real surfaces.

1.4 REFERENCES

1. ISO 13319 (2000) *Determination of particle size distributions – Electrical sensing zone method*, International Organization for Standardization, Geneva, Switzerland.
2. Orr Jr. C. and DallaValle J.M. (1959) *Fine Particle Measurement*, Macmillan, New York.
3. Allen T. (1981) *Particle Size Measurement*, Chapman and Hall, London.

2 Gas Adsorption

2.1 INTRODUCTION

Gas adsorption is one of many experimental methods available for the surface and pore size characterization of porous materials. These include small angle x-ray and neutron scattering (SAXS and SANS), mercury porosimetry, electron microscopy (scanning and transmission), thermoporometry, NMR-methods, and others. Each method has a limited length scale of applicability for pore size analysis. An overview of different methods for pore size characterization and their application range was recently given by IUPAC [1]. Among these methods gas adsorption is the most popular one because it allows assessment of a wide range of pore sizes (from 0.35 nm up to > 100 nm), including the complete range of micro- and mesopores and even macropores. In addition, gas adsorption techniques are convenient to use and are not that cost intensive as compared to some of the other methods. A combination of mercury porosimetry and gas adsorption techniques allows even performing a pore size analysis over a range from ca. 0.35 nm up to ca. 400 μm .

Adsorption can be understood as the enrichment of one or more components in an interfacial layer; in gas adsorption we consider the gas/solid interface. The solid is called the adsorbent and the gas, which is capable of being adsorbed, is called the adsorptive. The fluid in the adsorbed state is called adsorbate [2].

Invariably the amount adsorbed on a solid surface will depend upon the absolute temperature T , the pressure P , and the interaction potential E between the vapor (adsorbate) and the surface (adsorbent). Therefore, at some equilibrium pressure and temperature the weight W of gas adsorbed on a unit weight of adsorbent is given by

$$W = F(P, T, E) \quad (2.1)$$

Usually the quantity adsorbed is measured at constant temperature and equation (2.1) reduces to

$$W = F(P, E) \quad (2.2)$$

A plot of W versus P , at constant T , is referred to as the sorption isotherm of a particular gas-solid interface.

2.2 PHYSICAL AND CHEMICAL ADSORPTION

Depending upon the strength of the interaction, all adsorption processes can be divided into the two categories of chemical and physical adsorption. The former, also called irreversible adsorption or chemisorption, is characterized mainly by large interaction potentials, which lead to high heats of adsorption often approaching the value of chemical bonds. This fact, coupled with other spectroscopic, electron spin resonance, and magnetic susceptibility measurements confirms that chemisorption involves true chemical bonding of the gas or vapor with the surface. Because chemisorption occurs through chemical bonding it is often found to occur at temperatures above the critical temperature of the adsorbate. Strong bonding to the surface is necessary in the presence of higher thermal energies, if adsorption is to occur at all. In addition, chemisorption is usually associated with an activation energy, as is true for most chemical reactions. Furthermore, chemisorption is necessarily restricted to, at most, a single layer of chemically bound adsorbate on the surface. Another important feature of chemisorption is that the adsorbed molecules are more localized on the surface when compared to physical adsorption. Because of the formation of a chemical bond between an adsorbate molecule and a specific site on the surface the adsorbate is less free to migrate about the surface. This fact often enables the number of active sites on catalysts to be determined by simply measuring the quantity of chemisorbed gas.

The second category, reversible or physical adsorption, is a general phenomenon, which occurs whenever an absorbable gas (the adsorptive) is brought in contact with the surface of the solid adsorbent. Physisorption exhibits characteristics that make it most suitable for surface area-determinations as indicated by the following:

1. Physical adsorption is accompanied by low heats of adsorption with no violent or disruptive structural changes occurring to the surface during the adsorption measurement.
2. Unlike chemisorption, physical adsorption may lead to surface coverage by more than one layer of adsorbate.
3. Pores can be filled completely by the adsorptive for pore volume measurements. Such pore condensation phenomena can be used also to calculate the pore size and its distribution.
4. Physical adsorption equilibrium is achieved rapidly since no activation energy is required as is generally true in chemisorption. An exception here is adsorption in small pores where diffusion can limit the adsorption rate.
5. Physical adsorption is fully reversible, enabling both the adsorption and desorption processes to be studied.

molecular dispersion of light due to the light's electromagnetic field interaction with the oscillating dipole.

It is evident from the above that adsorption forces are similar in nature and origin to the forces that lead to liquefaction of vapors and that the same intermolecular interactions are responsible for both phenomena.

2.4 PHYSICAL ADSORPTION ON A PLANAR SURFACE

The London-van der Waals' interaction energy $U_s(z)$ of a gas molecule with a planar surface is given by

$$U_s(z) = C_1 z^{-9} - C_2 z^{-3} \quad (2.4)$$

where C_1 and C_2 are constants, and z is the distance of the gas molecule from the surface. The first term describes the repulsive forces that occur when the location of the molecule is too close to the surface (so-called Born repulsion). The second term represents the attractive fluid-wall interactions. The interaction potential $U_s(z)$ exhibits a minimum relatively close to the surface of the adsorbent and tends to zero for large distances from the surface (see Fig. 2.1). The (attractive) interaction energy at the minimum of the gas-solid potential is typically ten times greater than the thermal energy $k_b T$, where k_b is the Boltzmann constant and T is the absolute temperature. As a consequence, gas molecules will accumulate in the vicinity of the surface (see Fig.2.1).

At sufficiently low temperatures (typically around the boiling temperature of the adsorptive) a dense monolayer of molecules is formed at pressures P far below the saturation pressure P_0 and a multilayer adsorbed film of increasing thickness and liquid like density builds up on strongly adsorbing substrates as P_0 is approached. In this low-temperature region the adsorption of gases can be analyzed in terms of a two-phase model, in which an adsorbed phase coexists with the bulk phase [5]:

$$n^g = n_{\text{ads}} + n_{\text{bulk}} \quad (2.5)$$

$$V^g = V_{\text{ads}} + V_{\text{bulk}} \quad (2.6)$$

where n^g is the amount of gas and V^g the overall macroscopic volume accessible to the gas molecules; n_{ads} represents the amount and V_{ads} the volume of the adsorbed phase.

$\frac{1}{kT} \approx 2.5 \times 10^{20} \text{ mol}^{-1}$

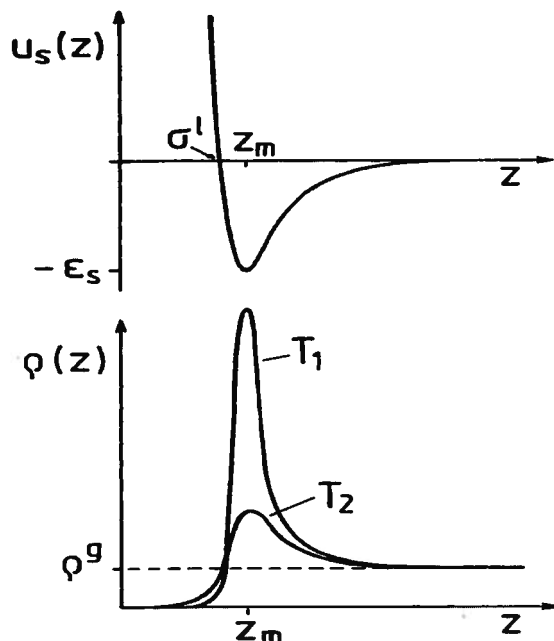


Figure 2.1 Gas-solid interaction potential $U_s(z)$ (upper graph) and density profile $\rho(z)$ of an ideal adsorbed gas at a flat, homogeneous surface for two temperatures $T_2 > T_1$. From [5].

However, at higher temperatures the model of an adsorbed phase becomes progressively unrealistic because (i) the tendency of molecules to accumulate near the surface of the adsorbent becomes less pronounced and (ii) due to the weaker physisorption at elevated temperatures higher pressures have to be applied in order to reach significant surface coverage [5]. As a consequence the density of the bulk gas phase is no longer negligible relative to the density near the surface and a clear separation between adsorbed phase and bulk gas phase is not possible, i.e. the profile of the local density $\rho(z)$ exhibits a smooth transition from the surface into the bulk gas. For this situation the definition of the adsorbed amount, i.e., the adsorption space, becomes problematic and other concepts have to be applied. One possibility is to express the adsorbed amount in terms of the surface excess, a concept that was first introduced by Gibbs [6].

The surface excess (not the adsorbed amount) is the quantity that is actually determined when using the volumetric or gravimetric technique (see chapters 13 and 14) to measure adsorption isotherms. Here a known amount of gas, n^g , is contained in a volume V^g in contact with the solid adsorbent. The experimentally determined adsorbed amount represents the excess

amount over and above the amount that would be present if the density of the gas remained constant and equal to that of the bulk fluid up to the surface [7]. Accordingly, experimentally the surface excess n^σ instead of the adsorbed amount n^a is determined

$$n^\sigma = n^b - \rho^b V^b \quad (2.7)$$

where ρ^b is the (molar) density of the bulk gas at the experimental temperature and pressure. Combining equations (2.5) – (2.7) leads to

$$n^\sigma = n_{\text{ads}} - \rho^b V_{\text{ads}} = (\rho_{\text{ads}} - \rho^b) V_{\text{ads}} \quad (2.8)$$

where the term $\rho^b V_{\text{ads}}$ represents the amount of gas in a volume equal to V_{ads} somewhere in the bulk phase and $\rho_{\text{ads}} = n_{\text{ads}}/V_{\text{ads}}$ is the mean density of the adsorbed phase.

At sufficiently low temperatures and pressures, the gas density is negligibly small against the density near the surface ($\rho^b \ll \rho_{\text{ads}}$) and thus the surface excess n^σ corresponds to the adsorbed amount n_{ads} , i.e. $n^\sigma \approx n_{\text{ads}}$. This is the typical situation encountered for nitrogen and argon adsorption at their boiling temperatures (77.35 K and 87.27 K, respectively), which is used for the surface and pore size characterization of solids and finely divided matter.

In contrast, adsorption in significant amounts occurs close to the critical point and in particular above the critical temperature (supercritical adsorption) only at higher pressures [5]. The bulk gas density is here so high that it cannot be neglected anymore, and as indicated before adsorption data are therefore usually given in terms of the surface excess.

2.4 REFERENCES

1. Rouquerol J., Avnir D., Fairbridge C.W., Everett D.H., Haynes J.H., Pernicone N., Ramsay J.D.F., Sing K.S.W. and Unger K.K. (1994) *Pure Appl. Chem.* **66**, 1739.
2. Sing K.S.W., Everett D.H., Haul R.A.W., Moscou L., Pierotti R.A., Rouquerol J. and Siemieniowska T. (1985) *Pure Appl. Chem.* **57**, 603.
3. Israelachvili J.N. (1985) *Intermolecular and Surface Forces*, Academic Press, London.
4. London F. (1930) *Z. Phys.* **63**, 245.
5. Findenegg G.H. and Thommes M. (1997) In *Physical Adsorption: Experiment, Theory and Application* (Fraissard J. and Conner W.C., eds), Kluwer, Dordrecht.
6. Gibbs J.W. (1957) *The Collected Works, Vol.1*, Yale University Press, New Haven, p219.
7. Everett D.H. (1972) *Pure Appl. Chem.* **31**, 579.

3 Adsorption Isotherms

3.1 PORE SIZE AND ADSORPTION POTENTIAL

The shape of sorption isotherms of pure fluids on planar surfaces and porous materials depends on the interplay between the strength of fluid-wall and fluid-fluid interactions as well as the effects of confined pore space on the state and thermodynamic stability of fluids confined to narrow pores. The International Union of Pure and Applied Chemistry [1] proposed to classify pores by their internal pore width (the pore width defined as the diameter in case of a cylindrical pore and as the distance between opposite walls in case of a slit pore), i.e., *Micropore*: pore of internal width less than 2 nm; *Mesopore*: pore of internal width between 2 and 50 nm; *Macropore*: pore of internal width greater than 50 nm.

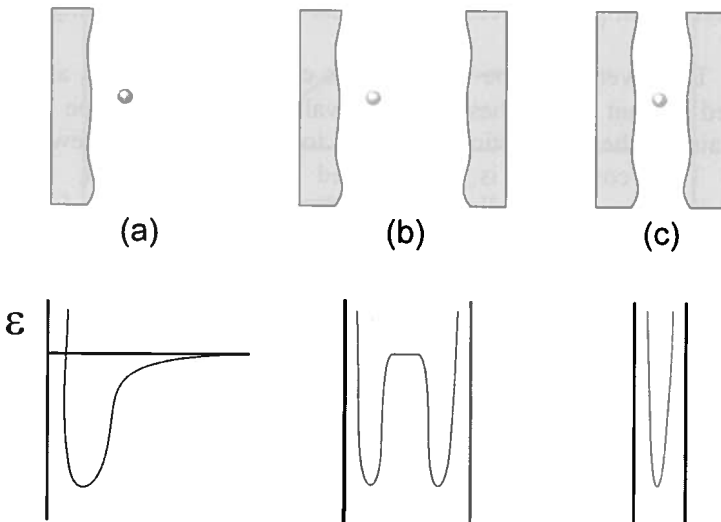


Figure 3.1 Schematic illustration of adsorption potential, ϵ , on (a) planar, nonporous surface; (b) mesopore; (c) micropore.

The sorption behavior in macropores is distinct from that of mesopores and micropores. Whereas macropores are so wide that they can be considered as nearly flat surfaces (see Fig. 3.1a) the sorption behavior in micropores is dominated almost entirely by the interactions between fluid

molecules and the pore walls; in fact the adsorption potentials of the opposite pore walls are overlapping. Hence the adsorption in micropores (i.e., micropore filling) is distinct from the adsorption phenomena occurring in mesopores. As illustrated in Fig. 3b, the pore potential in mesopores is not dominant anymore in the core of the pores. Hence, the adsorption behavior in mesopores does not depend only on the fluid-wall attraction, but also on the attractive interactions between fluid molecules, which may lead to the occurrence of capillary (pore) condensation. Pore condensation represents a phenomenon whereby gas condenses to a liquid-like phase in pores at a pressure less than the saturation pressure P_0 of the bulk fluid. It represents an example of a shifted bulk transition under the influence of the attractive fluid-wall interactions.

3.2. CLASSIFICATION OF ADSORPTION ISOTHERMS

Based upon an extensive literature survey, performed by Brunauer, Demming, Demming and Teller (BDDT)[2], the IUPAC published in 1985 a classification of six sorption isotherms [1], which reflects the situation discussed above in connection with figure 3.1. The appropriate IUPAC classification is shown in Fig. 3.2. Each of these six isotherms and the conditions leading to its occurrence are now discussed according to Sing *et al* [1].

The reversible type I isotherm is concave to the P/P_0 axis and the adsorbed amount approaches a limiting value as $P/P_0 \rightarrow 1$. Type I isotherms are obtained when adsorption is limited to, at most, only a few molecular layers. This condition is encountered in chemisorption, where the asymptotic approach to a limiting quantity indicates that all of the surface sites are occupied. In the case of physical adsorption, sorption isotherms obtained on microporous materials are often of type I. Micropore filling and therefore high uptakes are observed at relatively low pressures, because of the narrow pore width and the high adsorption potential. The limiting uptake is being governed by the accessible micropore volume rather than by the internal surface area.

Type II sorption isotherms are typically obtained in case of non-porous or macroporous adsorbent, where unrestricted monolayer-multilayer adsorption can occur. The inflection point or knee of the isotherm is called point B. This point indicates the stage at which monolayer coverage is complete and multilayer adsorption begins to occur.

The reversible type III isotherm is convex to the P/P_0 axis over its entire range and therefore does not exhibit a point B. This indicates that the attractive adsorbate-adsorbent interactions are relatively weak and that the adsorbate-adsorbate interactions play an important role. Isotherms of this type are not common, but an example is nitrogen adsorption on polyethylene

or the adsorption of water vapor on the clean basal plane of graphite.

Type IV isotherms are typical for mesoporous materials. The most characteristic feature of the type IV isotherm is the hysteresis loop, which is associated with the occurrence of pore condensation. The limiting uptake over a range of high P/P_0 results in a plateau of the isotherm, which indicates complete pore filling. The initial part of the type IV can be attributed to monolayer-multilayer adsorption as in case of the type II isotherm.

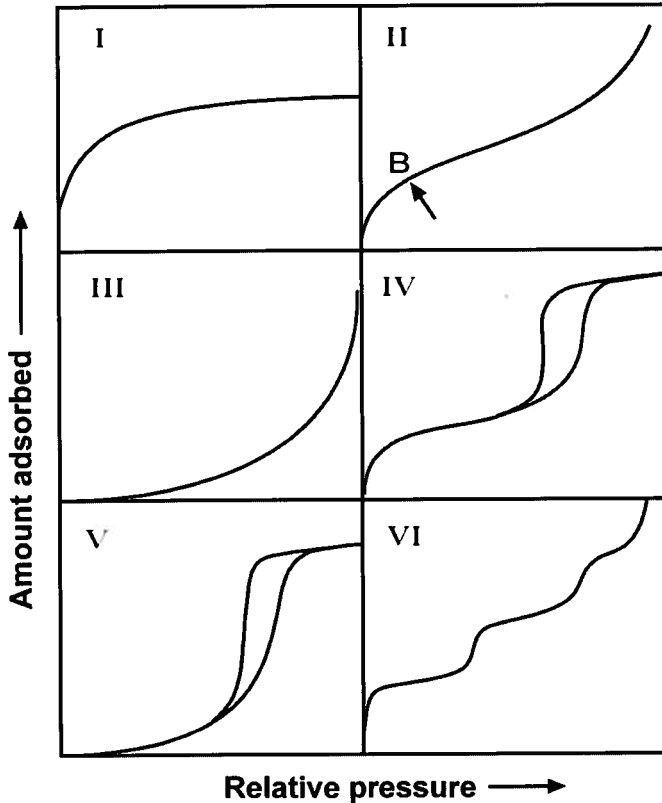


Figure 3.2 IUPAC classification of sorption isotherms. From [1].

Type V isotherms show pore condensation and hysteresis. However, in contrast to type IV the initial part of this sorption isotherm is related to adsorption isotherms of type III, indicating relatively weak attractive interactions between the adsorbent and the adsorbate.

The type VI isotherm is a special case, which represents stepwise

multilayer adsorption on a uniform, non-porous surface [3], particularly by spherically symmetrical, non-polar adsorptives. The sharpness of the steps depends on the homogeneity of the adsorbent surface, the adsorptive and the temperature. Type VI isotherms were for example obtained with argon [4] and krypton [5] on graphitized carbons at liquid nitrogen temperature.

3.3 REFERENCES

1. Sing K.S.W., Everett D.H., Haul R.A.W., Moscou L., Pierotti R.A., Rouquerol J. and Siemieniowska T. (1985) *Pure Appl. Chem.* **57**, 603.
2. Brunauer S., Deming L.S., Deming W.S. and Teller E. (1940) *J. Am. Chem. Soc.* **62**, 1723.
3. Hill. T.L. (1955) *J. Phys. Chem.* **59**, 1065.
4. Polley M.H., Schaeffer W.D. and Smith W.R. (1953) *J. Phys. Chem.* **57**, 469.
5. Greenhalgh E. (1967) *J. Phys. Chem.* **71**, 1151.

4 Adsorption Mechanism

4.1 LANGMUIR AND BET THEORIES (KINETIC ISOTHERMS)

The success of kinetic theories directed toward the measurements of surface areas depends upon their ability to predict the number of adsorbate molecules required to cover the solid with a single molecular layer. Equally important is the cross-sectional area of each molecule or the effective area covered by each adsorbed molecule on the surface. The surface area then, is the product of the number of molecules in a completed monolayer and the effective cross-sectional area of an adsorbate molecule. The number of molecules required for the completion of a monolayer will be considered in this chapter and aspects of the adsorbate cross-sectional area will be discussed in chapter 5.

4.1.1 *The Langmuir Isotherm*

The asymptotic approach of the quantity adsorbed toward a limiting value indicates that type I isotherms are limited to, at most, a few molecular layers. In the case of chemisorption, only one layer can be bonded to the surface and, therefore, true chemisorption always exhibits a type I isotherm. Although it is possible to calculate the number of molecules in the monolayer from the type I chemisorption isotherm, some serious difficulty is encountered when attempts are made to apply the cross-sectional adsorbate area. This difficulty arises because chemisorption tightly binds and localizes the adsorbate to a specific surface site so that the spacing between adsorbed molecules will depend upon the adsorbent surface structures as well as the size of the adsorbed molecules or atoms. In those cases where the surface sites are widely separated, the calculated surface area will be smaller than the actual values because the number of molecules in the monolayer will be less than the maximum number which the surface can accommodate. Nevertheless, it will be instructive to consider the type I isotherm in preparation for the more rigorous requirements of the other five types.

Using a kinetic approach, Langmuir [1] was able to describe the type I isotherm with the assumption that adsorption was limited to a monolayer. According to the kinetic theory of gases, the number of molecules N striking unit area of surface per second is given by

$$N = \frac{\bar{N}P}{\sqrt{2\pi\bar{M}RT}} \quad (4.1)$$

where \bar{N} is Avogadro's number, P is the adsorbate pressure, \bar{M} is the adsorbate molecular weight, R is the gas constant and T is the absolute temperature. If θ_0 is the fraction of the surface unoccupied (*i.e.*, with no adsorbed molecules) then the number of collisions with bare or uncovered surface per unit area of surface each second is

$$\frac{dN}{dt} = kP\theta_0 \quad (4.2)$$

where k is $\bar{N}/\sqrt{2\pi\bar{M}RT}$. The number of molecules striking and adhering to each unit area of surface is

$$N_{ads} = kP\theta_0 A_1 \quad (4.3)$$

where A_1 is the condensation coefficient and represents the probability of a molecule's being adsorbed upon collision with the surface.

The rate at which adsorbed molecules leave each unit area of surface is given by

$$N_{des} = N_m \theta_1 \nu_1 e^{-E/RT} \quad (4.4)$$

where N_m is the number of adsorbate molecules in a completed monolayer of unit area, θ_1 is the fraction of the surface occupied by the adsorbed molecules, E is the energy of adsorption and ν_1 is the vibrational frequency of the adsorbate normal to the surface when adsorbed. The product $N_m \theta_1$ is the number of molecules adsorbed per unit area. Multiplication by ν_1 converts this number of molecules to the maximum rate at which they can leave the surface. The term $e^{-E/RT}$ represents the probability that an adsorbed molecule possesses adequate energy to overcome the net attractive potential of the surface. Thus, equation (4.4) contains all the parameters required to describe the rate at which molecules leave each unit area of surface.

At equilibrium the rates of adsorption and desorption are equal. Thus equating (4.3) and (4.4):

$$N_m \theta_1 \nu_1 e^{-E/RT} = kP\theta_0 A_1 \quad (4.5)$$

Recognizing that $\theta_0 = 1 - \theta_1$, one obtains

$$N_m \theta_1 v_1 e^{-E_i/RT} = kPA_1 - \theta_1 kPA_1 \quad (4.6)$$

then

$$\theta_1 = \frac{kPA_1}{N_m v_1 e^{-E_i/RT} + kPA_1} \quad (4.7)$$

Allowing

$$K = \frac{kA_1}{N_m v_1 e^{-E_i/RT}} \quad (4.8)$$

Substitution of equation (4.8) into (4.7) gives

$$\theta_1 = \frac{KP}{1 + KP} \quad (4.9)$$

The assumption implicit in equation (4.8) is that the adsorption energy E is constant, which implies an energetically uniform surface. Up to and including one layer of coverage one can write

$$\theta_1 = \frac{N}{N_m} = \frac{W}{W_m} \quad (4.10)$$

where N and N_m are the number of molecules in the incomplete and complete monolayer, respectively, and W/W_m is the weight adsorbed relative to the weight adsorbed in a completed monolayer. Substituting W/W_m for θ_1 in equation (4.9) yields

$$\frac{W}{W_m} = \frac{KP}{1 + KP} \quad (4.11)$$

Equation (4.11) is the Langmuir equation for Type I isotherms. Rearrangement of equation (4.11) gives

$$\frac{P}{W} = \frac{1}{KW_m} + \frac{P}{W_m} \quad (4.12)$$

A plot of P/W versus P will give a straight line of slope $1/W_m$ and intercept $1/KW_m$ from which both K and W_m can be calculated. Having established W_m , the sample surface area S_t can then be calculated from equation (4.13):

$$S_t = N_m A_x = \frac{W_m \bar{N} A_x}{\bar{M}} \quad (4.13)$$

where A_x and \bar{M} are the cross-sectional area and the molecular weight of the adsorbate, respectively, and \bar{N} is Avogadro's number.

Although the Langmuir equation describes type I and sometimes chemisorption isotherms, it fails to be adequately general to treat physical adsorption and the type II-type V isotherms. In addition, surface area measurements obtained from type I isotherms are subject to uncertainties, regardless of whether chemisorption or physical adsorption is occurring. In chemisorption, localization of the adsorbate molecules leaves the value of A_x seriously in question, since the adsorbate will adsorb only at active surface sites, leaving an unspecified area around each chemisorbed molecule. When applied to physical adsorption, the type I isotherm is associated with the pore filling of micropores with no clearly defined region of monolayer coverage.

4.1.2 The Brunauer, Emmett and Teller (BET) Theory [2]

During the process of physical adsorption, at very low relative pressure, the first sites to be covered are the more energetic ones. Those sites with higher energy on a chemically pure surface reside within narrow pores where the pore walls provide overlapping potentials. Other high-energy sites lie between the horizontal and vertical edges of surface steps where the adsorbate can interact with surface atoms in two planes. In general, wherever the adsorbate is afforded the opportunity to interact with overlapping potentials, or an increased number of surface atoms, there will be a higher energy site. On surfaces consisting of heteroatoms, such as organic solids or impure materials, there will be variations in adsorption potential depending upon the nature of the atoms of functional groups exposed at the surface.

That the more energetic sites are covered first as the pressure is increased does not imply that no adsorption occurs on sites of lower potential. Rather, it implies that the average residence time of a physically adsorbed molecule is longer on the higher-energy sites. Accordingly, as the adsorbate pressure is allowed to increase, the surface becomes progressively coated and the probability increases that a gas molecule will strike and be adsorbed on a previously bound molecule. Clearly then, prior to complete surface coverage the formation of second and higher adsorbed layers will

commence. In reality, there exists no pressure at which the surface is covered with exactly a completed physically adsorbed monolayer. The effectiveness of the Brunauer, Emmett and Teller (BET) theory is that it enables an experimental determination of the number of molecules required to form a monolayer despite the fact that exactly one monomolecular layer is never actually formed.

Brunauer, Emmett, and Teller, in 1938, extended Langmuir's kinetic theory to multilayer adsorption. The BET theory assumes that the uppermost molecules in adsorbed stacks are in dynamic equilibrium with the vapor. This means that where the surface is covered with only one layer of adsorbate, an equilibrium exists between that layer and the vapor; where two layers are adsorbed, the upper layer is in equilibrium with the vapor, and so forth. Since the equilibrium is dynamic, the actual location of the surface sites covered by one, two or more layers may vary but the number of molecules in each layer will remain constant.

Using the Langmuir theory and equation (4.5) as a starting point to describe the equilibrium between the vapor and the adsorbate in the first layer,

$$N_m \theta_1 v_1 e^{-E_1/RT} = kP\theta_0 A_1 \quad (\text{cf. 4.5})$$

By analogy, for the fraction of surface covered by only two layers one may write

$$N_m \theta_2 v_2 e^{-E_2/RT} = kP\theta_1 A_2 \quad (4.14)$$

In general, for the n th layer one obtains

$$N_m \theta_n v_n e^{-E_n/RT} = kP\theta_{n-1} A_n \quad (4.15)$$

The BET theory assumes that the terms v , E , and A remain constant for the second and higher layers. This assumption is justifiable only on the grounds that the second and higher layers are all equivalent to the liquid state. This undoubtedly approaches reality as the layers proceed away from the surface but is somewhat questionable for the layers nearer the surface because of polarizing forces. Nevertheless, using this assumption one can write a series of equations, using L as the heat of liquefaction

$$N_m \theta_1 v_1 e^{-E_1/RT} = kP\theta_0 A_1 \quad (\text{cf. 4.5})$$

$$N_m \theta_2 v e^{-L/RT} = kP\theta_1 A \quad (4.16a)$$

$$N_m \theta_3 v e^{-L/RT} = kP \theta_2 A \quad (4.16b)$$

and, in general, for the second and higher layers

$$N_m \theta_n v e^{-L/RT} = kP \theta_{n-1} A \quad (4.16c)$$

From these equations, it follows that

$$\frac{\theta_1}{\theta_0} = \frac{kPA_1}{N_m v_1 e^{-E_1/RT}} = \alpha \quad (4.17a)$$

$$\frac{\theta_2}{\theta_1} = \frac{kPA}{N_m v e^{-L/RT}} = \beta \quad (4.17b)$$

$$\frac{\theta_3}{\theta_2} = \frac{kPA}{N_m v e^{-L/RT}} = \beta \quad (4.17c)$$

$$\frac{\theta_n}{\theta_{n-1}} = \frac{kPA}{N_m v e^{-L/RT}} = \beta \quad (4.17d)$$

then

$$\theta_1 = \alpha \theta_0 \quad (4.18a)$$

$$\theta_2 = \beta \theta_1 = \alpha \beta \theta_0 \quad (4.18b)$$

$$\theta_3 = \beta \theta_2 = \alpha \beta^2 \theta_0 \quad (4.18c)$$

$$\theta_n = \beta \theta_{n-1} = \alpha \beta^{n-1} \theta_0 \quad (4.18d)$$

The total number of molecules adsorbed at equilibrium is

$$N = N_m \theta_1 + 2N_m \theta_2 + \dots + nN_m \theta_n = N_m (\theta_1 + 2\theta_2 + \dots + n\theta_n) \quad (4.19)$$

Substituting for $\theta_1, \theta_2, \dots$ from equations (4.18 a-d) gives

$$\frac{N}{N_m} = \alpha\theta_0 + 2\alpha\beta\theta_0 + 3\alpha\beta^2\theta_0 + \dots + n\alpha\beta^{n-1}\theta_0 \quad (4.20a)$$

$$= \alpha\theta_0(1 + 2\beta + 3\beta^2 + \dots + n\beta^{n-1}) \quad (4.20b)$$

Since both α and β are assumed to be constants, one can write

$$\alpha = C\beta \quad (4.21)$$

This defines C by using equations (4.17a) and (4.17b-d) as

$$\frac{A_1 V_2}{A_2 V_1} e^{(E_1 - E)/RT} = C \quad (4.22)$$

Substituting $C\beta$ for α in equation (4.20) yields

$$\frac{N}{N_m} = C\theta_0(\beta + 2\beta^2 + 3\beta^3 + \dots + n\beta^n) \quad (4.23)$$

The preceding summation is just $\beta/(1-\beta)^2$. Therefore,

$$\frac{N}{N_m} = \frac{C\theta_0\beta}{(1-\beta)^2} \quad (4.24)$$

Necessarily

$$1 = \theta_0 + \theta_1 + \theta_2 + \dots + \theta_n \quad (4.25)$$

Then

$$\theta_0 = 1 - (\theta_1 + \theta_2 + \dots + \theta_n) = 1 - \sum_{n=1}^{\infty} \theta_n \quad (4.26)$$

Substituting equation (4.26) into (4.24) gives

$$\frac{N}{N_m} = \frac{C\beta}{(1-\beta)^2} \left(1 - \sum_{n=1}^{\infty} \theta_n \right) \quad (4.27)$$

Replacing θ_n in equation (4.27) with $\alpha\beta^{n-1}\theta_0$ from equation (4.18d)

yields

$$\frac{N}{N_m} = \frac{C\beta}{(1-\beta)^2} \left(1 - \alpha\theta_0 \sum_{n=1}^{\infty} \beta^{n-1} \right) \quad (4.28)$$

and introducing $C\beta$ from equation (4.21) in place of α gives

$$\frac{N}{N_m} = \frac{C\beta}{(1-\beta)^2} \left(1 - C\theta_0 \sum_{n=1}^{\infty} \beta^n \right) \quad (4.29)$$

The summation in equation (4.29) is

$$\sum_{n=1}^{\infty} \beta^n = \beta + \beta^2 + \dots + \beta^n = \frac{\beta}{1-\beta} \quad (4.30)$$

Then

$$\frac{N}{N_m} = \frac{C\beta}{(1-\beta)^2} \left(1 - C\theta_0 \frac{\beta}{1-\beta} \right) \quad (4.31)$$

From equation (4.24) we have

$$\frac{C\beta}{(1-\beta)^2} = \frac{N}{N_m} \frac{1}{\theta_0} \quad (\text{cf. 4.24})$$

Then equation (4.31) becomes

$$1 = \frac{1}{\theta_0} \left(1 - C\theta_0 \frac{\beta}{1-\beta} \right) \quad (4.32)$$

and

$$\theta_0 = \frac{1}{1 + C\beta/(1-\beta)} \quad (4.33)$$

Introducing θ_0 from equation (4.33) into (4.24) yields

$$\frac{N}{N_m} = \frac{C\beta}{(1-\beta)(1-\beta+C\beta)} \quad (4.34)$$

When β equals unity, N/N_m becomes infinite. This can physically occur when adsorbate condenses on the surface or when $P/P_0 = 1$.

Rewriting equation (4.17d) for $P = P_0$, gives

$$1 = \frac{kAP_0}{N_m v e^{-L/RT}} \quad (4.35)$$

but

$$1 = \frac{kAP}{N_m v e^{-L/RT}} \quad (\text{cf. 4.17d})$$

then

$$\beta = \frac{P}{P_0} \quad (4.36)$$

Introducing this value for β into (4.34) gives

$$\frac{N}{N_m} = \frac{C(P/P_0)}{(1-P/P_0)[1-P/P_0+C(P/P_0)]} \quad (4.37)$$

Recalling that $N/N_m = W/W_m$ (equation 4.10) and rearranging equation (4.37) gives the BET equation in final form,

$$\frac{1}{W[P/P_0-1]} = \frac{1}{W_m C} + \frac{C-1}{W_m C} \left(\frac{P}{P_0} \right) \quad (4.38)$$

If adsorption occurs in pores limiting the number of layers then the summation in equation (4.37) is limited to n and the BET equation takes the form

$$\frac{W}{W_m} = \frac{C}{[P/P_0-1]} \frac{[1-(n+1)(P/P_0)^n + n(P/P_0)^{n+1}]}{[1+(C-1)P/P_0 - C(P/P_0)^{n+1}]} \quad (4.39)$$

Equation (4.39) reduces to (4.38) with $n = \infty$ and to the Langmuir equation with $n = 1$.

The application of the BET (essentially equation (4.38)) and the Langmuir approach (essentially equation (4.11)) for the determination of the specific surface area will be discussed in chapter 5.

4.2 THE FRENKEL-HALSEY-HILL (FHH) THEORY OF MULTILAYER ADSORPTION

Physisorption at temperatures below the critical temperature T_c and in the complete wetting regime leads to the development of multilayer adsorption by approaching the saturation pressure P_0 . The BET theory describes adsorption of the first two or three layers in a satisfying way, but fails to assess correctly the range of the adsorption isotherm, which is associated with the development of thick multilayer films.

Beyond a film thickness of two or three molecular layers, the effect of surface structure is largely smoothed out and close to the saturation pressure the adsorbed layer has a thickness, which allows to consider the adsorbed film as a slab of liquid. It is assumed that here the adsorbed film has the same properties (i.e., density etc.) as the bulk liquid would have at this temperature. This is the basic assumption of the slab approximation, which was first proposed by Frenkel [3] and was later also derived independently by Halsey [4] and Hill [5]. The only modification to its free energy of the adsorbed liquid slab arises from the interaction with the solid, i.e., the adsorption forces (dispersion forces). The interaction energy $U_s(z)$ of a gas molecule at distance z from a solid surface is approximately given as

$$U_s(z) \approx C_{sf}\rho_s/z^3 \quad (4.40)$$

where C_{sf} is a measure for the strength of attractive fluid-wall interactions and ρ_s represents the solid density.

Within the spirit of the FHH approach, the chemical potential difference $\Delta\mu = \mu_a - \mu_0$ between an adsorbed, liquid-like film (μ_a) of thickness $z = l$ and the value (μ_0) at gas-liquid coexistence of the bulk fluid is given by

$$\Delta\mu = \mu_a - \mu_0 = -RT \ln(P/P_0) = u(z) = -\alpha l^3 \quad (4.41)$$

The more general equation (4.41) is known as the Frenkel-Halsey-Hill (FHH) equation:

$$\Delta\mu = \mu_a - \mu_0 = -RT \ln(P/P_0) = -\alpha l^m \quad (4.42)$$

where α is an empirical parameter, characteristic for the gas-solid interaction. For non-retarded van-der-Waals' interactions (i.e., dispersion forces), one expects $m = 3$ (as expected from equation (4.41)). According to equation 4.42, the FHH-equation predicts that the thickness of a film l ($z = l$) adsorbed on a solid surface is expected to increase without limit ($l \rightarrow \infty$) for $\mu_a \rightarrow \mu_0$, i.e. by approaching $P/P_0 = 1$.

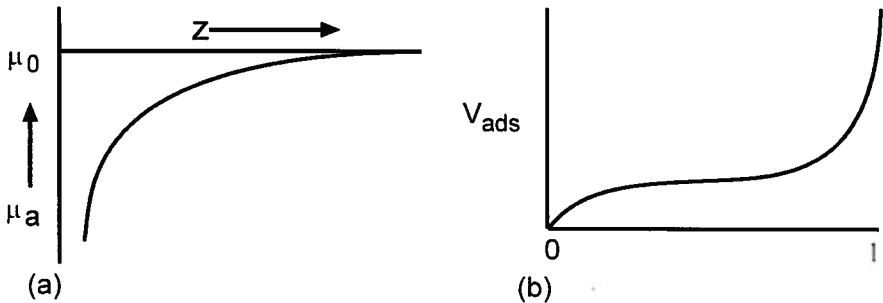


Figure 4.1 (a) Chemical potential difference of an adsorbed film as function of distance z (i.e. film thickness l) from the adsorbent surface. The film thickness diverges by approaching μ_0 , which corresponds to a relative pressure $P/P_0 = 1$. (b) Corresponding adsorption isotherm revealing the diverging of the film thickness (and V_{ads} for $P/P_0 \rightarrow 1$).

In the case of low temperature adsorption (e.g. adsorption of nitrogen and argon at their boiling temperatures) the adsorption can be analyzed in terms of a two-phase model in which a clearly defined adsorbed phase coexists with a bulk gas phase of low density (see chapter 2). In this case the thickness of the adsorbed liquid-like multilayer, l , can be related to the volume V_{liq} of the adsorbed phase, viz

$$l = V_{\text{liq}}/S \quad (4.43)$$

where S is the total surface area. Inserting this expression into the equation (4.42) gives

$$\ln(P/P_0) = -\alpha (V_{\text{liq}}/S)^m \quad (4.44)$$

The validity of the FHH equation can be tested by plotting $\log\log(P/P_0)$ against $\log(V_{\text{liq}}/S)$ (the classical FHH plot). In the multilayer region of the sorption isotherm a straight line should be obtained; the slope is indicative of Frenkel-Halsey-Hill exponent m . Experimental values usually found for

m are often significantly smaller than the theoretical values of 3, i.e., values of $m = 2.5-2.7$ are found even for strongly attractive adsorbents like graphite [6], as well as for samples with oxidic surfaces like silica, alumina, rutile etc. [7]. The deviations from the theoretical value $m = 3$ were often attributed to interparticle condensation (in case of powders [6,8]), which overlaps with multilayer adsorption, as well as to surface roughness and fractality of the adsorbent surface (see chapter 7). In addition it was found that the relative pressure range over which a linear FHH plot is achieved seems to depend on the nature of the adsorbent-adsorbate interaction [7]. Please note also that the FHH theory is only applicable in the regime of high relative pressures, where the assumption that the adsorbate can be considered as slab of liquid with bulk-like properties can be indeed justified. Accordingly, when the FHH theory is applied to the low or middle range of isotherms the values obtained for m etc. can only be considered as empirical.

The temperature dependence of the FHH-equation was tested by Findenegg and co-workers [6,8,9] over a large temperature up to the critical temperature T_c . In the region of higher temperatures and pressures the relative pressure P/P_0 has to be replaced by the ratio of appropriate fugacities f/f_0 . The correspondent FHH equation can then be written in the form: $\ln(f/f_0) = -\alpha r^m$ [10] and it could be concluded that the simple FHH-equation remains indeed applicable up to nearly the critical point.

4.3 ADSORPTION IN MICROPOROUS MATERIALS

4.3.1 Introduction

According to IUPAC [11] pores are classified as macropores for pore widths greater than 500 Å, mesopores for the pore range 20 to 500 Å and micropores for pore widths less than 20 Å. Because of the intense potential fields in very narrow pores (overlapping fields from opposite pore walls), the mechanism of pore filling is different as in mesopores. Mesopores fill via pore condensation (see chapter 4.4), which represents a first order gas-liquid phase transition. In contrast the filling of micropores reflects in most cases a continuous process. The micropore range is subdivided into those smaller than about 7 Å (ultramicro-pores) and those in the range from 7 to 20 Å (supermicro-pores). The filling of ultramicro-pores (pore width smaller < 7 Å) occurs at very low relative pressures and is entirely governed by the enhanced gas-solid interactions. However, in addition to the strong adsorption potential a cooperative mechanism may play a role in the pore filling process of so-called supermicro-pores [12]. The relative pressure where micropore filling occurs is dependent on a number of factors including the size and nature of the molecules of the adsorptive, the pore shape and the effective pore width. The pore filling capacity depends essentially on the accessibility of the pores for the probe molecules, which is

determined by the size of the molecule and the chosen experimental conditions.

In an ideal case microporous materials exhibit type I isotherms (see IUPAC classification, i.e., Fig. 3.2 in chapter 3). However, many microporous adsorbents (e.g., active carbons) contain pores over a wide range of pore sizes, including micro- and mesopores. Accordingly, the observed adsorption isotherm reveals features from both type I and type IV isotherms. An example is shown in Fig. 4.2, which shows the nitrogen isotherm (at ~ 77 K) on a disordered active carbon sample. The observed hysteresis loop is indicative of mesoporosity, whereas the type I behavior is clearly visible in the lower relative pressure range. Another example is shown in Fig. 4.3, which shows the adsorption isotherm at 87 K (i.e., liquid argon temperature) in a faujasite zeolite. In order to reveal details of the adsorption isotherm (in particular in the range of the low relative pressures where micropore filling occurs), the isotherm is favorably represented in a semi-logarithmic scale of the relative pressure. The strong increase of the adsorbed amount close to saturation pressure results from pore condensation into large meso- and macropores.

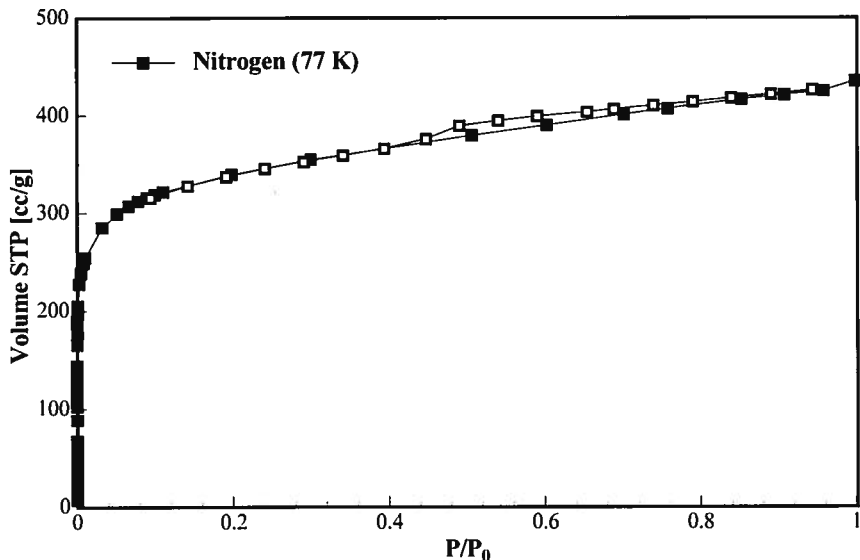


Figure 4.2 Nitrogen adsorption at 77.35 K on an active carbon sample, which contains, in addition to its microporosity, some mesoporosity indicated by the occurrence of hysteresis and the fact that the adsorption isotherm does not reveal a truly horizontal plateau at relative pressures > 0.1 ; the observed slope being associated with the filling of mesopores.

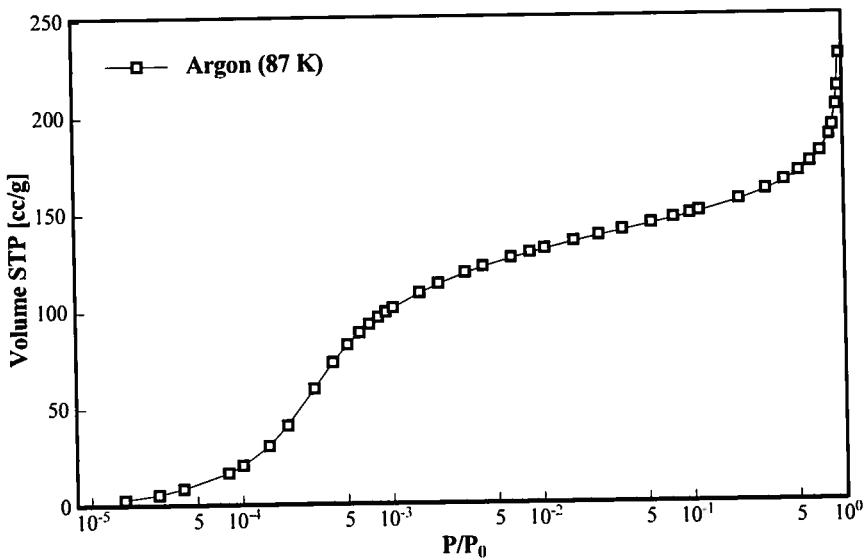


Figure 4.3 Semi-logarithmic isotherm plot of argon at 87K on a faujasite zeolite which clearly resolves the micropore filling in the low relative pressure range. The steep increase close to the saturation pressure represents the pore filling of large meso- and macro-pores.

In order to interpret sorption isotherms measured on microporous materials various methods and theories have been developed. The so-called 'classical methods' are based on macroscopic, thermodynamic assumption, i.e., they assume that the adsorbed pore fluid is liquid-like and that it reveals essentially the same properties as a bulk liquid at the same temperature.

Such classical approaches are, for instance, the theories for micropore characterization by Polanyi [13], Dubinin [14-16], Stoeckli [17] including the more recent approaches by Horvath-Kawazoe (HK) [18] and related methods [19]. In contrast to these macroscopic approaches, methods like the Density Functional Theory (DFT) [20] or methods of molecular simulation (e.g., Monte Carlo simulation methods (MC), Molecular Dynamics methods (MD)) [21,22] provide not only a microscopic model of adsorption but lead also to a better assessment of the thermodynamic properties of the pore fluid. These theories, which are based on statistical mechanics, connect macroscopic properties to the molecular behavior allowing a much more realistic description of micropore filling, which is the prerequisite for an accurate and comprehensive pore size analysis.

In chapter 4.3.2 we will discuss some aspects of macroscopic, classical theories for adsorption in microporous materials. In chapter 4.3.3, we focus on some aspects of the microscopic methods (e.g., Density Functional Theory (DFT) and Molecular Simulation), which are meanwhile frequently used to describe adsorption in micropores.

4.3.2 Aspects of Classical, Thermodynamic Theories for Adsorption in Micropores: Extensions of Polanyi's Theory

Polanyi's potential theory of adsorption [13] views the area immediately above an adsorbent's surface as containing equipotential lines that follow the contour of the surface potential. When a molecule is adsorbed, it is considered trapped between the surface and the limiting potential plane at which the 'adsorption potential' has fallen to zero. Fig. 4.4 illustrates these equipotential planes. In the diagram, Y represents a pore and X depicts some surface impurity.

According to the potential theory, the volume \tilde{V} , defined by the adsorbent's surface and the equipotential plane, E_n , can contain adsorbate in three different conditions, depending upon temperature. Above the critical temperature, the adsorbate cannot be liquefied and the gas in the adsorption volume, \tilde{V} , simply becomes more dense near the surface.

At temperatures just below the critical temperature, the adsorbate is viewed as a liquid near the surface and a vapor of decreasing density away from the surface.

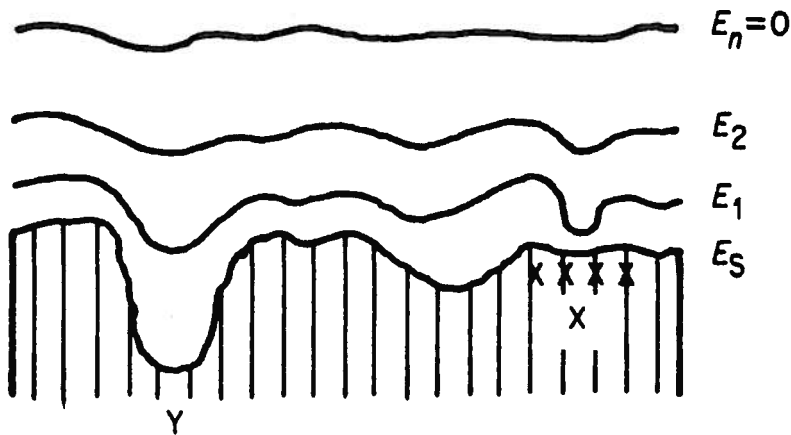


Figure 4.4 Polanyi's potential planes.

At temperatures much less than the critical temperature ($T \leq 0.8T_c$), the adsorption volume is considered to contain only liquid. Under the latter conditions one can write

$$\tilde{V} = \frac{W}{\rho} \quad (4.45)$$

where W and ρ are the adsorbate weight and density, respectively.

The potential theory asserts that when the adsorbate is in the liquid state, the adsorption potential is given by

$$E = RT \ln \frac{P_0}{P} \quad (4.46)$$

According to the preceding equation, E is the isothermal work required to compress the vapor from its equilibrium pressure, P , to the saturated pressure, P_0 , of the liquid in the adsorption volume.

Using equations (4.45) and (4.46), both \tilde{V} and E can be calculated from an experimental isotherm. Therefore,

$$\tilde{V} = F(E) \quad (4.47)$$

Plots of \tilde{V} versus E take the form shown in Fig.4.5 and are called 'characteristic curves'. If two adsorbates fill the same adsorption volume, as shown by the vertical dotted line in Fig. 4.5, their adsorption potentials, E and E_0 , will differ only because of differences in their molecular properties. Consequently, the ratio of adsorption potentials is assumed by Dubinin [14,15] to be constant. Dubinin calls E/E_0 the 'affinity coefficient', which, for an adsorbate pair, is a measure of their relative affinities for a surface. Using the adsorption for one vapor, say E_0 , as a reference value, the ratio of potentials can be written as

$$\frac{E}{E_0} = \beta \quad (4.48)$$

Substitution into equation (4.47) then gives, for the reference vapor,

$$\tilde{V} = F\left(\frac{E}{\beta}\right) \quad (4.49)$$

Using benzene as the reference or standard vapor ($\beta = 1$), Dubinin and Timofeev [14a] were able to calculate values of β for other adsorbents. The characteristic curves, shown in Fig. 4.5, appear similar to the positive side of a Gaussian curve.

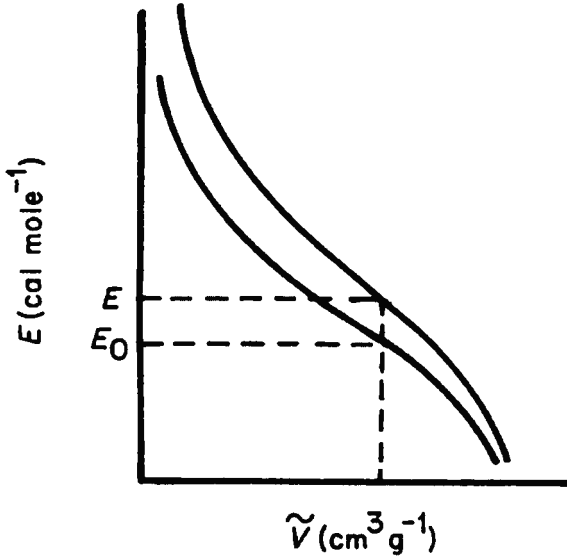


Figure 4.5 Characteristic curves for two vapors.

These similarities led Dubinin and Radushkevich (“DR”) [14b] to postulate that the fraction of the adsorption volume, \tilde{V} , occupied by liquid adsorbate at various values of adsorption potentials, E , can be expressed as a Gaussian function. Thus,

$$\tilde{V} = \tilde{V}_0 \exp(-KE^2) \quad (4.50)$$

where K is a constant, determined by the shape of the pore size distribution, and \tilde{V}_0 is the total adsorption volume or the microporous volume. Substituting the value for E_0 from equation (4.48) gives

$$\tilde{V} = \tilde{V}_0 \exp(-K(E/\beta)^2) \quad (4.51)$$

Equation (4.51) is applicable to micropores, rather than larger pores, because the overlapping potential from the walls of pores only slightly larger than an adsorbate molecule will considerably enhance the adsorption potential. Substituting for E in equation (4.51) using equation (4.46) yields

$$\tilde{V} = \tilde{V}_0 \exp \left[-K \left(\frac{RT}{\beta} \ln \frac{P_0}{P} \right)^2 \right] \quad (4.52)$$

which can be rewritten as

$$\log W = \log(\tilde{V}_0 \rho) - 2.303K \left[\frac{RT}{\beta} \log \left(\frac{P_0}{P} \right) \right]^2 \quad (4.53)$$

where W and ρ are the weight adsorbed and the liquid adsorbate density, respectively. Simplifying equation (4.53) yields

$$\log W = \log(\tilde{V}_0 \rho) - k \left[\log \left(\frac{P_0}{P} \right) \right]^2 \quad (4.54)$$

where

$$k = 2.303K \left(\frac{RT}{\beta} \right)^2 \quad (4.55)$$

A plot of $\log W$ versus $[\log(P_0/P)]^2$ should give a straight line with an intercept of $\log(\tilde{V}_0 \rho)$, from which \tilde{V}_0 , the micropore volume, can be calculated. Linear DR plots over a large relative pressure range can be found for a number of microporous carbons. For many other adsorbents (zeolites are particularly problematic) the linear range is limited over a very narrow relative pressure range. The DR equation often fails in the case where the microporous adsorbent is very heterogeneous with regard to surface chemistry and texture. In such cases the application of a generalized form of the DR equation, i.e., the Dubinin-Asthakov ("DA") equation [16] is of advantage (see chapter 9).

$$\tilde{V} = \tilde{V}_0 \exp(-A/E)^n \quad (4.56)$$

where $A = -RT \ln(P/P_0)$ and n is the Dubinin-Asthakov parameter, which depends not only on the heterogeneity of the adsorbent but of course also on the relative pressure range of the sorption isotherm, where the DA-equation was applied. Further improvements were made by Stoeckli and co-workers, who introduced an alternative to the DA-equation [17]. However, details of the interactions of the adsorptive molecules with the porous material, and their impact on micropore filling (and thus the shape of the adsorption isotherm) were not considered until the Horvath-Kawazoe (HK) theory [18] and related approaches [19] were published (see chapter 9.5 for more details). Although the HK-related methods take into account the effect of pore geometry, and the strength of the attractive adsorptive-adsorbent

interaction on the adsorption potential, they still assume incorrectly that the thermophysical properties of the strongly confined liquid-like pore fluid does not differ from the properties of the corresponding bulk liquid. These obstacles can be overcome by applying modern methods of statistical mechanics, which we discuss in the following section, 4.3.3.

4.3.3 Aspects of Modern, Microscopic Theories for Adsorption in Micropores: Density Functional Theory and Molecular Simulation

Density functional theory and computer simulation methods have been developed into powerful methods for the description of the sorption and phase behavior of fluids, confined to porous materials. These methods allow equilibrium density profiles of a fluid adsorbed on surfaces and in pores to be calculated, from which properties such as the adsorption/desorption isotherm, heats of adsorption, neutron scattering patterns and transport properties for model systems can be derived.

Pioneering studies on the application of density functional theory and molecular modeling by computer simulation in order to study the sorption and phase behavior of fluids in pores were performed by Evans and Tarazona [20], Gubbins et al. [21,22], Quirke et al. [23] and Fischer et al. [24] in the time period from 1985 to 1989. Seaton et al. [25] were the first to apply Density Functional Theory to calculate the pore size distribution in both the meso- and micropore range. In their approach, the so-called Local Density Functional Theory (LDFT) approach was used, which still represents a significant improvement over the macroscopic, thermodynamic descriptions of pore filling, but is inaccurate for narrow micropores – mainly because LDFT fails to take into account the short-range correlations in these pores. In contrast, the Non-Local Density Functional Theory (NLDF) and Monte Carlo computer simulation techniques provide a much more accurate description of a fluid confined to narrow pores and both are able to produce the strong oscillation characteristics of a fluid density profile at a solid fluid interface (see Fig. 4.6). The first paper where the non-local density functional theory was used for pore size analysis (of microporous carbons) was published in 1993 by Lastoskie *et al.* [26]. Since then, the Non-Local Density Theory was quite often employed to calculate the pore size distribution of micro- and mesoporous materials. In order to do so, NLDF methods dedicated to specific adsorptive/adsorbent pairs had to be developed [27,28]. In particular, Neimark and Ravikovitch [28] confirmed the validity of NLDF by comparing the calculated pore size distribution curves for mesoporous molecular sieves (e.g., MCM 41, which consist of an array of independent pores) and zeolites (e.g., ZSM 5) with pore size results obtained from other techniques, (e.g., methods based on like XRD, TEM etc.), which are independent of the position of the pore filling step in the adsorption isotherm.

4.3.3.1 Density Functional Theory (DFT). In experimental systems the adsorbed fluid in a pore is in equilibrium with a bulk gas phase. For such a system the grand canonical ensemble provides the appropriate description of the thermodynamics. The local density $\rho(r)$ of the pore fluid is therefore determined by minimizing of the correspondent grand potential $\Sigma[\rho(r)]$. Once $\rho(r)$ is known, other thermodynamic properties, such as the adsorption isotherm, heat of adsorption, free energies, phase transitions, etc. can be calculated. The grand potential function $\Sigma[\rho(r)]$ is given by the following term

$$\Omega[\rho(r)] = F[\rho(r)] - \int dr \rho(r)(\mu - V_{ext}(r)) \quad (4.57)$$

where $F[\rho(r)]$ is the intrinsic Helmholtz free energy functional in the absence of any external field and $V_{ext}(r)$ is the potential imposed by the walls, i.e., $\Sigma[\rho(r)]$ depends of course on all the interactions.

The parameters of the fluid-fluid interactions are usually determined in a way that they allow to reproduce the bulk properties (e.g., surface tension, gas-liquid coexistence curve etc.). Parameters of the solid-fluid interactions can then be obtained by fitting the calculated adsorption isotherms on a planar surface to the standard (e.g., nitrogen) isotherm. In addition, it is assumed that the fluid is contained in individual pores of simple geometry (e.g., slits or cylinders). For instance, an individual slit pore can be represented as two infinite, parallel graphitic slabs, separated by a width W , the distance between the centers of carbon atoms (for a carbon slit-pore).

Fig. 4.6 shows NLDFT density profiles of a fluid confined to a slit-pore of pore width ca. 5σ , where σ is the diameter of one molecule. The fluid shows the characteristic density oscillations (which reflect adsorbed layers) throughout the complete narrow pore space, which demonstrates the strong adsorption potential (in contrast, mesopores reveal a bulk-fluid like region in the core of the pore, see Fig. 4.10). It is also clearly visible that in such a small pore only two adsorbed layers can build up on each pore wall.

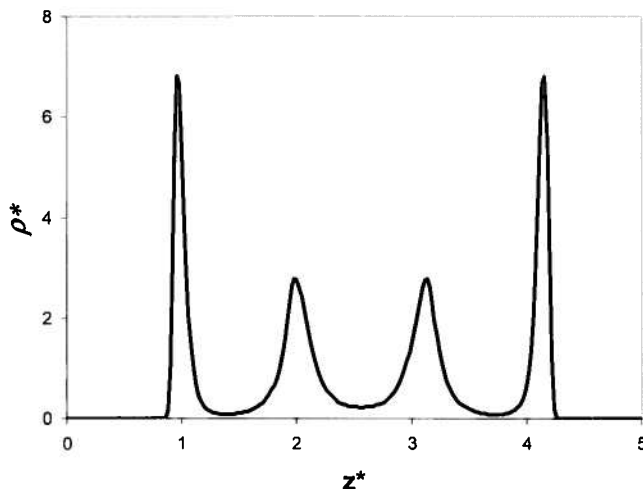


Figure 4.6 Characteristic density profile of a Lennard-Jones fluid in a slit pore of width 5σ , where σ is the diameter of one molecule [29a].

4.3.3.2 Computer Simulation Studies: Monte Carlo Simulation and Molecular Dynamics. The most prominent computer simulation method for the study of adsorption and wetting phenomena of fluids on planar surfaces and in pores is the Grand Canonical Monte Carlo simulation method (GCMC). This technique simulates the situation of an adsorbed fluid (or mixture) in equilibrium with a bulk fluid reservoir, which reflects usually the situation encountered in experimental studies of confined systems. A random number generator is used to move and rotate the molecules in a random fashion, which leads to particular configurations. Such movements and the resulting configurations are then accepted or rejected according to thermodynamic criteria (i.e., based on the temperature and chemical potential). After generating a long sequence of such moves (so-called Markov chain, typically in the order of several millions), they can be averaged (based on equations of statistical mechanics) to obtain the equilibration density profiles and, hence, the adsorption isotherm.

The molecular dynamics (MD) method applies Newton's equations of motion in order to obtain the trajectories and velocities of molecules. This method allows determining the transport as well as equilibrium properties of the system. The method is not as frequently used as GCMC, but some excellent work was performed using this method to study the adsorption and phase behavior of fluids in pores [e.g., 24].

4.3.3.3 NLDFT and Monte Carlo Simulation for Pore Size Analysis.

NLDFT and GCMC are considered to be the most advanced methods with regard to pore size analysis of micro- and mesoporous materials. For very narrow micropores the Monte Carlo simulation is considered to be the most accurate method. In both techniques, a set of isotherms calculated for a set of pore sizes in a given range for a given adsorptive constitutes the model database (these isotherms are calculated by integrating the equilibrium density profiles, $\rho(r)$, of the fluid in the model pore). Such a set of isotherms, called a kernel, is the basis for pore size analysis by Density Functional Theory [e.g., 28]. The calculation of the pore size distribution is based on a solution of the Generalized Adsorption Isotherm equation (GAI), which correlates the kernel of theoretical adsorption/desorption isotherms with the experimental sorption isotherm:

$$N(P/P_0) = \int_{W_{MIN}}^{W_{MAX}} N(P/P_0, W) f(W) dW \quad (4.58)$$

where $N(P/P_0)$ = experimental adsorption isotherm data, W = pore width, $N(P/P_0, W)$ = isotherm on a single pore of width W and $f(W)$ = pore size distribution function.

The GAI equation reflects the assumption that the total isotherm consists of a number of individual "single pore" isotherms multiplied by their relative distribution, $f(W)$, over a range of pore sizes. The set of $N(P/P_0, W)$ isotherms (kernel) for a given system (adsorptive/adsorbent) can be obtained, as indicated above, by either Density Functional Theory or by Monte Carlo computer simulation. The pore size distribution is then derived by solving the GAI equation numerically. In general, the solution of the GAI represents an ill-posed problem, which requires some degree of regularization. However meaningful and stable solutions of this equation can be obtained by existing regularization algorithms [e.g., 26- 29]. Because the equilibrium density profiles are known for each pressure along an isotherm no assumptions about the pore filling mechanism are required as in case of the macroscopic, thermodynamic methods. Hence, NLDFT and GCMC allow describing the adsorption isotherm over the complete range, and it is possible to obtain with a single method a pore size distribution which extends over the complete micro-mesopore range.

The application of these advanced methods for micro- and mesopore size analysis is discussed in chapters 8 and 9.

4.4 ADSORPTION IN MESOPORES

4.4.1 Introduction

The sorption behavior in mesopores (2- 50 nm) depends not only on the fluid-wall attraction, but also on the attractive interactions between fluid molecules. This leads to the occurrence of multilayer adsorption and capillary (pore) condensation. Pore condensation is the phenomenon whereby a gas condenses to a liquid-like phase in a pore at a pressure P less than the saturation pressure P_0 of the bulk liquid. Typically, type IV and V sorption isotherms according to the IUPAC classification (see chapter 3) can be observed. Significant progress was achieved during the last decade with regard to the understanding of sorption phenomena in narrow pores and the subsequent improvement in the pore size analysis of porous materials (which will be discussed in chapter 8). This progress can be primarily attributed to: (i) the discovery of novel ordered mesoporous materials, such as MCM-41, MCM-48, SBA-15 [30], which exhibit a uniform pore structure and morphology and could therefore be used as model adsorbents to test theories of gas adsorption; (ii) carefully performed adsorption experiments and (iii) the development of microscopic methods, such as the Non-Local-Density Functional Theory (NLDFT) or computer simulation methods (e.g. Monte-Carlo – and Molecular-Dynamic simulations), which allow to describe the configuration of adsorbed molecules in pores on a molecular level. In the following chapter we discuss the most important phenomena occurring in mesopores, i.e. multilayer adsorption, phase transition (e.g., pore condensation) and sorption hysteresis in the context of classical approaches and the most recent developments.

4.4.2 Multilayer Adsorption, Pore Condensation and Hysteresis

As described in §4.2, in the complete wetting range a multilayer adsorbed film is produced at the pore walls. For fluids in contact with a planar surface the thickness l of the adsorbed film is expected to increase without limit, i.e., $l \rightarrow \infty$ for $P/P_0 \rightarrow 1$.

$$\Delta\mu_a = \mu_a - \mu_0 = -RT \ln(P/P_0) = -\alpha l^m \quad (\text{cf } 4.42)$$

where α is the fluid-wall interaction parameter, and the l^m law results from the long-range van der Waals' interactions between a fluid molecule and a semi-infinite planar wall. In the case of non-retarded van der Waals' fluid-wall interactions, the exponent m has a theoretical value of 3. However, experimental values for m are often significantly smaller than the theoretical value, even for strongly attractive adsorbents like graphite, i.e., $m = 2.5 - 2.7$ (see chapter 4.2 for a more detailed discussion).

In pores, however, the film thickness cannot grow unlimited. The stability of this film is determined by the attractive fluid-wall interactions, the surface tension and curvature of the liquid-vapor interface. In this case the difference in chemical potential $\Delta\mu = \mu - \mu_0$ between the adsorbed liquid-like film (μ) and the value at gas-liquid coexistence (μ_0) of the bulk fluid is given by

$$\Delta\mu = \Delta\mu_a + \Delta\mu_c \quad (4.59)$$

For small film thickness the first term $\Delta\mu_a$ (equation cf. (4.43)) associated with multilayer adsorption dominates:

$$\Delta\mu_a = -\alpha l^m \quad (\text{cf. 4.42})$$

When the adsorbed film becomes thicker, the adsorption potential will become less important, and $\Delta\mu$ will be dominated almost entirely by the curvature contribution $\Delta\mu_c$ (i.e., the Laplace term), which is given for cylindrical pores by

$$\Delta\mu_c = -(\gamma/a \Delta\rho) \quad (4.60)$$

where a is the core radius ($a = r - l$; r is the pore radius), γ is the surface tension of the adsorbed liquid-like film (which is assumed to be identical with the liquid), $\Delta\rho = \rho^l - \rho^g$, describes the density difference between the liquid like film and the vapor phase. At a critical thickness, l_c , pore condensation occurs in the core of the pore, controlled by intermolecular forces in the core fluid. Pore condensation represents a first-order phase transition from a gas-like state to a liquid-like state of the pore fluid, occurring at a chemical potential μ less than the value of μ_0 at gas-liquid coexistence of the bulk fluid.

These phenomena are illustrated in Fig.4.7, which depicts a sorption isotherm as it is expected for adsorption/desorption of a pure fluid in a single mesopore of cylindrical shape in combination together with a schematic representation of the appropriate sorption and phase phenomena occurring in the pore. Please note, that the schematic isotherm reveals a vertical pore condensation step; however, a truly vertical step in the adsorption isotherm is not to be expected for any real porous material with a non-vanishing pore-size distribution, i.e. the wider the pore size distribution, the less sharp is the pore condensation step. At lower relative pressures the adsorption mechanism in mesopores is comparable to that on planar surfaces. After completion of the monolayer formation (**A**), multilayer adsorption commences (**B**). After reaching a critical film thickness (**C**), capillary condensation occurs essentially in the core of the pore (transition

from configuration **C** to **D**). The plateau region of the isotherm reflects the situation where the pore is completely filled with liquid and separated from the bulk gas phase by a hemispherical meniscus. Pore evaporation therefore occurs by a receding meniscus (**E**) at a pressure, which is less than the pore condensation pressure. The pressure where the hysteresis closes corresponds again to the situation of an adsorbed multilayer film which is in equilibrium with a vapor in the core of the pore and the bulk gas phase. In the relative pressure range between (**F**) and (**A**) adsorption and desorption are reversible.

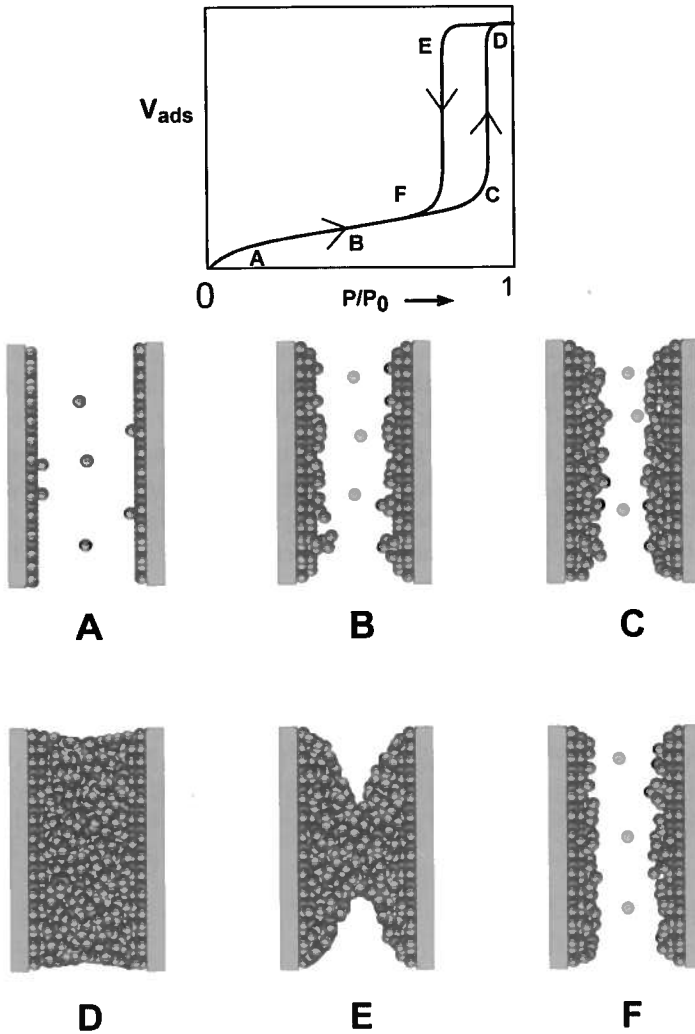


Figure 4.7 Schematic representation of multilayer adsorption, pore condensation and hysteresis in a single cylindrical pore. From [43b].

4.4.3 Pore Condensation: Macroscopic, Thermodynamic Approaches

4.4.3.1 *Classical Kelvin Equation.* For pores of uniform shape and width pore condensation can be treated on the basis of the Kelvin approach, which relates the shift from bulk coexistence, $\Delta\mu = \mu - \mu_0 = -RT \ln(P/P_0)$, to macroscopic properties such as surface tension, the densities of the bulk gas and liquid and the contact angle θ of the liquid meniscus against the pore wall. The condition for the coexistence of liquid and gas in a cylindrical pore of radius r and temperature T is then given by the Kelvin equation [31]:

$$\Delta\mu = \mu - \mu_0 = -RT \ln(P/P_0) = -\frac{2\gamma \cos\theta}{r_m \Delta\rho} \quad (4.61)$$

where R is the universal gas constant, γ is again the surface tension of the liquid, θ the contact angle of the liquid against the pore wall, $\Delta\rho = \rho^l - \rho^g$, where ρ^l represents the orthobaric liquid density at bulk coexistence and ρ^g is the gas density, and r_m is the mean radius of curvature of the meniscus of the pore liquid. In a cylindrical pore the condensed liquid reveals a hemispherical meniscus and the mean radius of curvature corresponds to the pore radius (i.e., the Kelvin radius).

The contact angle θ can be considered as a measure of the relative strength of fluid-wall and fluid-fluid interactions, i.e., the relative strength of fluid-wall and fluid-fluid interactions enters implicitly through the contact angle θ . One would expect the occurrence of pore condensation as long as the contact angle is $< 90^\circ$. For fluids in contact with a single planar wall, one expects complete wetting in the temperature range between the so-called wetting temperature T_w and the critical temperature T_C of the fluid. At temperatures below the wetting temperature incomplete wetting ($\cos\theta < 1$) is observed.

In the case of nitrogen adsorption at 77 K the gas density is small against the liquid density, and ρ^g can be neglected. The liquid density is often given as $1/\rho^l = \bar{V}$, where \bar{V} is the molar volume of the condensed liquid. In addition it is assumed that we have the situation of complete wetting, i.e., the contact angle is assumed to be zero. In this case the Kelvin equation is stated as

$$\ln P/P_0 = \frac{-2\gamma\bar{V}}{rRT} \quad (4.62)$$

The Kelvin equation relates the equilibrium vapor pressure exerted from the curved meniscus of the pore liquid to the equilibrium pressure of the same liquid on a plane surface. The difference in vapor pressure between

the flat and the curved surface is related to the phenomenon of a (mechanical) pressure drop across an interface (having two principal radii of curvature of the surface r_1 and r_2) as described by the Young-Laplace equation, viz $\Delta P = 2\gamma/r_m$, where r_m is the radius of mean curvature, which is given by $1/r_m = 1/2 [1/r_1 + 1/r_2]$. For a spherical surface $r_m = r_2 = r_1$, and the Laplace equation becomes $\Delta P = 2\gamma/r$, where r is the radius of the spherical surface. The Kelvin equation can be derived by using thermodynamics to assess the effect of a change in mechanical pressure, ΔP , on the molar free energy, which leads to an expression where ΔP is replaced by a function of relative vapor pressures (see for instance derivation in ref. [32]).

An alternative way to derive the Kelvin equation on purely thermodynamic grounds is based on the following: Consider the transfer of ∂n molecules of vapor in equilibrium with the bulk liquid at pressure P_0 into a pore where the equilibrium pressure is P . This process consists of three steps: evaporation from the bulk liquid, expansion of the vapor from P_0 to P , and condensation into the pore. The first and third steps are equilibrium processes and are therefore accompanied by zero free energy change, $\partial G = 0$. The free energy change for the second step is described by

$$\partial G = \left(RT \ln \frac{P}{P_0} \right) \partial n \quad (4.63)$$

When the adsorbate condenses in the pore, it does so on a previously adsorbed film, thereby decreasing the film-vapor interfacial area. The free energy change associated with the filling of the pore is given by

$$\partial G = -(\gamma \cos \theta) \partial S \quad (4.64)$$

where γ is again the surface tension of the adsorbed film (assumed to be identical with that of the liquid), ∂S is the change in interfacial area, and θ is again the contact angle, which is taken to be zero, since the liquid is assumed to wet completely the adsorbed film.

Equations (4.59) and (4.60), when combined using the assumption of a zero wetting angle, yield

$$\frac{\partial n}{\partial S} = \frac{-\gamma}{RT \ln P/P_0} \quad (4.65)$$

The volume of liquid adsorbate that condenses in a pore of volume V_p is given by

$$\partial V_p = \bar{V} \partial n \quad (4.66)$$

where \bar{V} is the molar volume of the liquid adsorbate. Substituting equation (4.61) into equation (4.62) gives

$$\frac{\partial V_p}{\partial S} = \frac{-\gamma \bar{V}}{RT \ln P/P_0} \quad (4.67)$$

The ratio of volume to area within a pore depends upon the pore geometry. For example, the volume to area ratios for cylinders, parallel plates, and spheres are, respectively, $r/2$, $r/2$, and $r/3$, where r is the cylinder radius, the sphere radius, or the separation distance between parallel plates. If the pore shapes are highly irregular or consist of a mixture of regular geometries, the volume to area ratio can be too complex to express mathematically. In these cases, or in the absence of specific knowledge of the pore geometry, the assumption of cylindrical pores is usually made. Then equation (4.67) becomes the Kelvin equation

$$\ln P/P_0 = \frac{-2\gamma \bar{V}}{rRT} \quad (\text{cf } 4.62)$$

The Kelvin equation provides a correlation between pore diameter and pore condensation pressure, i.e., the smaller the radius, the lower is the P/P_0 value at which pore condensation occurs. In case of real porous materials consisting of pores of different sizes, condensation will occur first in the pores of smaller radii and will progress into the larger pores, at a relative pressure of unity condensation will occur on those surfaces where the radius of curvature is essentially infinite. Conversely, as the relative pressure is decreases evaporation will occur progressively out of pores with decreasing radii.

4.4.3.2 Modified Kelvin Equation. The original Kelvin equation (equation 4.62) does not take into account any fluid-wall interaction parameter, and consequently not the existence of an adsorbed multilayer film prior to pore condensation as illustrated in Fig.4.7. Taking into account that in case of complete wetting the pore walls are covered by a multilayer adsorbed film at the onset of pore condensation, one obtains the modified Kelvin equation [33], which is given for cylindrical pores by:

$$\ln(P/P_0) = \frac{-2\gamma \cos \theta}{RT\Delta\rho(r_p - t_c)} \quad (4.68)$$

where t_c describes the (critical) statistical thickness (see chapter 8) prior to condensation (all other symbols are the same as in case of equation 4.61).

The modified Kelvin equation serves as the basis for many methods applied for pore size analysis of mesoporous materials including the Barrett-Joyner-Halenda method (BJH) [34], which is widely used. In order to account for the preadsorbed multilayer film, the Kelvin equation is combined with a standard isotherm or a so-called t-curve, which usually refers to adsorption measurements on a non-porous solid. Accordingly, the preadsorbed multilayer film is assessed by the statistical (mean) thickness of an adsorbed film on a nonporous solid of a surface similar to that of the sample under consideration (such statistical thickness equations were derived for instance by Halsey, Harkins & Jura and de-Boer (see chapters 8 and 9 for a discussion of these equations)). The application of the modified Kelvin equation for mesopore size analysis and its limitations will be discussed in chapter 8.

In contrast to the Kelvin approach, more sophisticated approaches such as the Broeckhoff and de Boer [35] as well as the Cole-Saam theory [36] capture essentially the mechanism of pore condensation and hysteresis as it is described above. These theories take into account the (i) influence of the adsorption potential on the chemical potential where pore condensation occurs in the pores and (ii) the effect of curvature on the thickness of the adsorbed multilayer film. In agreement with experimental observations, these theories predict that an increase in the strength of the attractive fluid-wall interaction, a lowering of the experimental temperature as well as decreasing the pore size will shift the occurrence of pore condensation to lower relative pressures. However all these thermodynamic, macroscopic theories do not take into account the peculiarities of the critical region. In contrast, microscopic theories, such as NLDFT or molecular simulation allow a much more accurate description of the state of the pore fluid, also close to the critical point. This will be discussed in more detail in section 4.4.7.

4.4.4 Adsorption Hysteresis

4.4.4.1. Classification of Hysteresis Loops. It is widely accepted that there is a correlation between the shape of the hysteresis loop and the texture (e.g., pore size distribution, pore geometry, connectivity) of a mesoporous adsorbent. An empirical classification of hysteresis loops was given by the IUPAC [11], which is based on an earlier classification by de Boer [37]. The IUPAC classification is shown in Fig 4.8. According to the IUPAC classification type H1 is often associated with porous materials consisting of

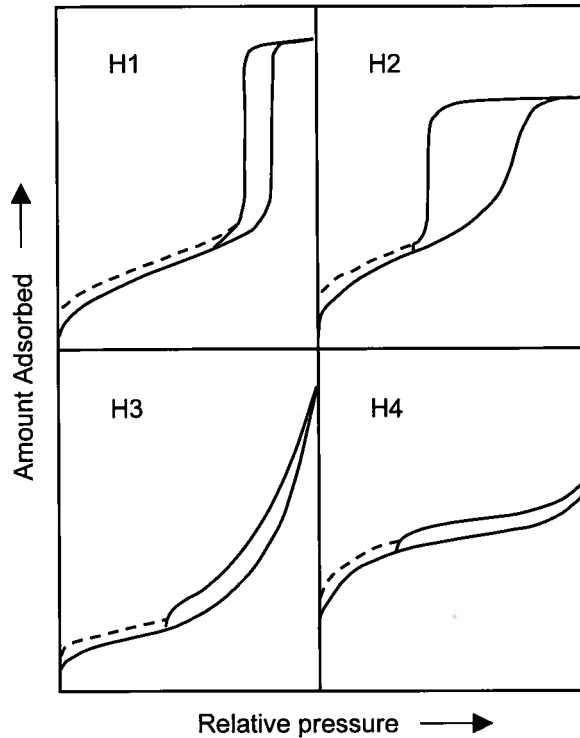


Figure 4.8 IUPAC classifications of hysteresis loops. From [11].

well-defined cylindrical-like pore channels or agglomerates of compacts of approximately uniform spheres. It was found that materials that give rise to H2 hysteresis are often disordered and the distribution of pore size and shape is not well defined. Isotherms revealing type H3 hysteresis do not exhibit any limiting adsorption at high P/P_0 , which is observed with non-rigid aggregates of plate-like particles giving rise to slit-shaped pores. The desorption branch for type H3 hysteresis contains also a steep region associated with a (forced) closure of the hysteresis loop, due to the so-called tensile strength effect. This phenomenon occurs for nitrogen at 77K in the relative pressure range from 0.4 – 0.45 (see chapter 8.6.2 for a detailed discussion). Similarly, type H4 loops are also often associated with narrow slit pores, but now including pores in the micropore region (see for instance Fig. 4.3, which depicts the nitrogen sorption isotherm on activated carbon).

The dashed curves in the hysteresis loops shown in Fig. 4.8 reflect low-pressure hysteresis, which may be observable down to very low relative pressure. Low-pressure hysteresis may be associated with the change in volume of the adsorbent, i.e. the swelling of non-rigid pores or with the irreversible uptake of molecules in pores of about the same width as that of

the adsorptive molecule. In addition chemisorption will also lead to such "open" hysteresis loops. An interpretation of sorption isotherms showing low-pressure hysteresis is difficult and an accurate pore size analysis is not possible anymore. But also the hysteresis loops usually associated with pore condensation imposes, of course, a difficulty to the pore size analysis of the porous materials and the decision whether the adsorption –or desorption branch should be taken for calculation of the pore size distribution curve depends very much on the reason(s) which caused the hysteresis. Hence, we discuss the origin of pore condensation hysteresis in the following section, 4.4.4.2.

4.4.4.2 Origin of Hysteresis As mentioned before the occurrence of pore condensation/evaporation in mesoporous adsorbents is often accompanied by hysteresis. However, the mechanism and origin of sorption hysteresis is still a matter of discussion. There are essentially three models that contribute to the understanding of sorption hysteresis: (a) *independent (single) pore model* (b) *network model*, and (c) *disordered porous material model*. In the following we will discuss some aspects of these models.

(a) *Independent Pore Model*. Sorption hysteresis is considered as an intrinsic property of a phase transition in a single, idealized pore, reflecting the existence of metastable gas states. The hysteresis loop expected for this case is of type H1, according to the IUPAC classification.

Different approaches, which would explain the occurrence of hysteresis in a single pore, can be found in the literature since *ca.* 1900. Cohan [32] assumed that pore condensation occurs by filling the pore from the wall inward (for a cylindrical pore model). It was suggested that pore condensation would be controlled by a cylindrical meniscus once the pore is filled, whereas evaporation of the liquid would occur from a hemispherical meniscus, which would lead according to the Kelvin equation to different values of P/P_0 for condensation and evaporation.

Theories by Foster [38], Cassell [39], Everett [40], Cole and Saam (CS) [35] and Ball and Evans [41] suggested that hysteresis may be caused by the development of metastable states of the pore fluids associated with the capillary condensation transition in a manner analogous to superheating or supercooling of a bulk fluid. These ideas could be essentially confirmed by recent theoretical studies based on Non Local Density Functional Theory (NLDFT) [42]. These studies revealed that the H1 hysteresis can indeed be attributed to the existence of metastable states of the pore fluid, associated with the nucleation of the liquid phase, i.e., pore condensation is delayed. In principle, both pore condensation and pore evaporation can be associated with metastable states of the pore fluid [49]. This is consistent with the classical van der Waals picture, which predicts that the metastable adsorption branch terminates at a vapor-like spinodal, where the limit of stability for the metastable states is achieved and the fluid spontaneously

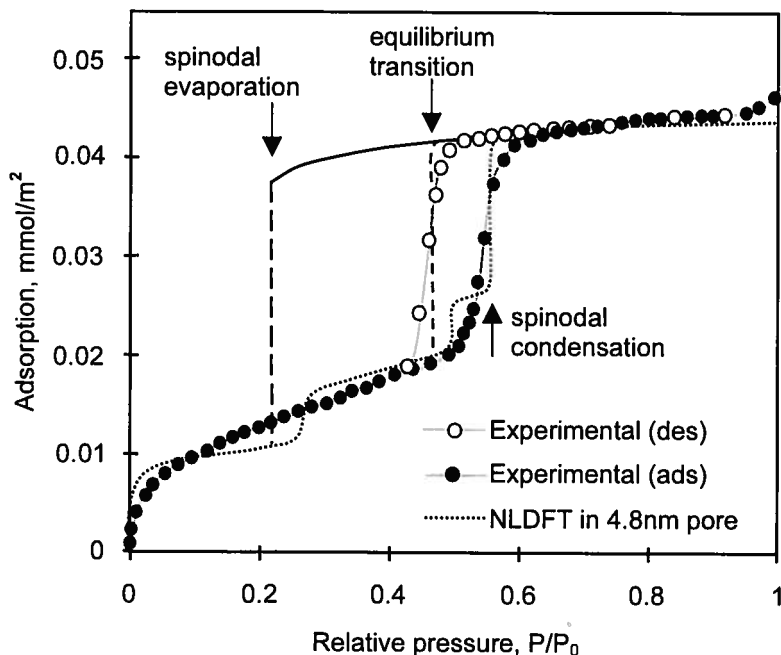


Figure 4.9 NLDFT adsorption isotherm of argon at 87K in a cylindrical pore of diameter 4.8 nm in comparison with the appropriate experimental sorption isotherm on MCM-41. It can be clearly seen that the experimental desorption branch is associated with the equilibrium gas-liquid phase transition, whereas the condensation step corresponds to the spinodal spontaneous transition. From [42].

condenses into a liquid-like state (so-called spinodal condensation). Accordingly, the desorption branch would terminate at a liquid-like spinodal, which corresponds to spontaneous evaporation (spinodal evaporation) In practice however, metastabilities occur only on the adsorption branch. Assuming a pore of finite length (which is always the case in real adsorbents) evaporation can occur via a receding meniscus (see Fig.4.5) and therefore metastability is not expected to occur during desorption. The NLDFT prediction for pore condensation and hysteresis in comparison with the correspondent experimental sorption isotherm of argon at 87 K in MCM-41 silica is shown in Fig. 4.9 (from ref. [42]). The experimental isotherm and the NLDFT isotherm agree quite well and the theoretical prediction for the position of the equilibrium liquid-gas transition (which corresponds to the condition at which the two states have equal grand potential) agrees quite well with the experimentally observed evaporation transition, i.e. the position of the desorption branch of the hysteresis loop. Hence, it was concluded that the desorption branch is associated with the equilibrium gas-liquid phase transition. In such a case the desorption branch

should be chosen for pore size analysis if theories/methods are applied which describe the equilibrium transition (e.g., BJH, conventional NLDFT). This will be discussed in more detail in chapter 8.

The small steps in the theoretical isotherm are a consequence of assuming a structureless (i.e., chemically and geometrically smooth) pore wall model, which neglects the heterogeneity of the MCM-41 pore walls.

There is also some evidence that type H1 hysteresis as observed in ordered three dimensional pore systems such as MCM-48 silica [43a] but also in highly ordered porous glasses (such as sol-gel glasses [44] and controlled pore glasses [45]) is predominantly caused by the existence of metastable states associated with pore condensation. The hysteresis loops could be described by applying models based on the independent pore model (e.g., Cole-Saam theory [44,45] NLDFT [43a] etc.). Accordingly, classical networking and pore blocking effects are not necessarily present in an (ordered) interconnected pore system (please see also chapter 8.6).

(b) *Network Model.* Sorption hysteresis is explained as a consequence of the interconnectivity of a real porous network with a wide distribution of pore sizes. If network and pore blocking effects are present typically a hysteresis loop of type H2 (IUPAC classification) is expected.

Network models take into account that in many materials the pores are connected and form a three-dimensional network. An important feature of the network model is the possibility of pore blocking effects during evaporation, which occurs if a pore has access to the external gas phase only via narrow constrictions (e.g., an ink-bottle pore). The basis for the understanding of sorption hysteresis in inkbottle pores and networks can be found in the work of McBain [46]. The wide inner portion of an inkbottle pore is filled at high relative pressures, but it cannot empty during desorption until the narrow neck of a pore first empties at lower relative pressure. Thus, in a network of inkbottle pores the capillary condensate in the pores is obstructed by liquid in the necks. The relative pressure at which a pore empties now depends on the size of the narrow neck, the connectivity of the network and the state of neighboring pores. Hence, the desorption branch of the hysteresis loops does not (in contrast to the single pore model) occur at thermodynamic equilibrium, but reflects a percolation transition instead. In such a case the desorption branch of the hysteresis loop is much steeper (compared to the adsorption branch) leading to H2 hysteresis according to the IUPAC classification.

Work by Everett [40] and others have led to the development of several specific network models. Advanced network or percolation models were introduced for instance by Mason [47] Wall and Brown [48], Neimark [49], Parlari and Yortsos [50], Ball and Evans [41], Seaton et al. [51] and Rojas et al. [52].

Type H2 hysteresis is observed in many disordered porous materials such as, for instance, porous Vycor® glass, or disordered sol-gel glasses. By

combining different experimental techniques such as adsorption measurements (volumetric, gravimetric), ultrasound and light scattering [53] or gas adsorption and *in situ* neutron scattering [54] some evidence for a percolation mechanism associated with pore evaporation could be obtained.

However, the existence of the conventional pore blocking mechanism as described above is under discussion. Sarkisov and Monson [55] concluded that the H₂ hysteresis loop (obtained from a molecular dynamics study of adsorption of a simple fluid) typically observed in inkbottle pores is not necessarily caused by the occurrence of conventional pore blocking. The large cavities could be emptied by a diffusional mass transport process from the fluid in the large cavity to the narrow neck and from there into the gas phase, hence the pore body can empty even while the pore neck remains filled. Further experimental and theoretical work by Ravikovitch *et al.* [56] suggests that both conventional pore blocking and so-called cavitation can occur in inkbottle type pores depending on temperature and pore size.

Cavitation corresponds to the situation of spinodal evaporation, i.e., the condensed liquid evaporates when the limit of stability of metastable pore liquid is achieved and the pore fluid spontaneously evaporates into a vapour-like state as shown in Fig. 4.9. In such a case the desorption branch does not reflect the thermodynamic equilibrium liquid-gas transition. The cavitation effect is correlated with the occurrence of a lower limit of hysteresis in the sorption isotherm, which is within the classical picture correlated with the so-called tensile strength effect. This effect is believed to be the cause for the observation that for many disordered porous materials the hysteresis loop for nitrogen adsorption at 77.35 K is forced to close at relative pressure at or above 0.42, apparently independent of the porous material [57, 58]. The existence of a lower closure point affects primarily the position of the desorption branch with regard to its position and steepness. Despite the fact that the reasons for this phenomenon are still not sufficiently understood, it is clear that it leads to complications for pore size calculation, which we will discuss in chapter 8.

(c) *Disordered Porous Material Model.* A more realistic picture takes into account that the thermodynamics of the pore fluid is determined by phenomena spanning the complete pore network. Even with the incorporation of network and percolation effects the adsorption thermodynamics is still modeled at a single pore level, i.e., the behavior of the fluid in the entire pore space is not assessed. In order to achieve this one needs to consider models which attempt to describe the microstructure of porous materials at length scales beyond that of a single pore. According to Gubbins *et al.* [59] there are two general approaches to construct a model of nanoporous materials by methods of molecular simulation. The first is the so-called mimetic simulation, and involves the development of a simulation strategy, that mimics the development of the pore structure in the materials preparation. In fact, Gelb and Gubbins [60] have reproduced the complex

network structure of porous glasses such as Vycor® and controlled-pore glass by applying molecular simulation and have studied the sorption and hysteresis behavior of xenon in such systems. Grand Canonical Monte Carlo simulation results for xenon adsorption in these systems suggest strongly that the shape of the adsorption/desorption hysteresis does not depend on the connectivity of the material model, supporting the hypothesis that in materials of this type (e.g., a porous Vycor® glass with a porosity of 30%) the fluid in different pores behaves quasi-independently, and that no system-spanning phase transitions occur during adsorption or desorption.

The second approach is the reconstruction method. Here one seeks a molecular model, whose structure matches available experimental structure data. Monson and co-workers investigated by Monte Carlo simulation the condensation and hysteresis phenomena of a Lennard-Jones fluid in a reconstructed model of silica xerogel [61]. Their adsorption isotherms exhibited hysteresis loops of type H1 and H2 in agreement with experimental results obtained on the same type of material. The observed hysteresis was attributed with thermodynamic metastability of the low and high density phases of the adsorbed fluid – however these phases span the entire void space of the porous material and are therefore not associated with the individual pores.

However, it was also suggested that in disordered porous glass materials (e.g., porous Vycor® glass) the origin of the hysteresis is associated with long time dynamics, which is so slow that on (experimentally) accessible time scales, the systems appear to be equilibrated, which leads to the observed reproducible results in the observation of the hysteresis loop [62, 63].

Theoretical and experimental work is necessary to (i) clarify what determines the shape of the hysteresis loop in such disordered systems and (ii) to obtain a clearer picture of the nature of phase behavior of fluids in disordered porous systems.

4.4.5 Effects of Temperature and Pore Size: Experiments and Predictions of Modern, Microscopic Theories

As discussed before, the Kelvin approach considers pore condensation as a gas-liquid phase transition in the core of the pore between two homogenous, bulk-like gas and liquid phases. The density difference $\Delta\rho = \rho^l - \rho^g$ is considered to be equal to the difference in orthobaric densities of coexisting bulk phases, i.e., pore condensation and hysteresis are expected to occur up to the bulk critical point, where $\Delta\rho = 0$.

In contrast, microscopic theories such as density functional theory, molecular simulation and lattice model calculations [22-24, 64-68] predict that a fluid confined to a single pore can exist with two possible density profiles corresponding to inhomogeneous gas- and liquid configurations in

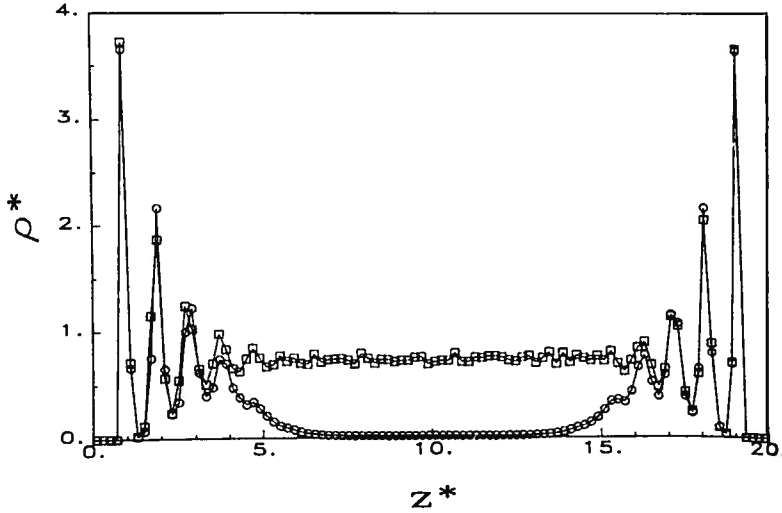


Figure 4.10 Density profiles of coexisting gas (circles)- and liquid configurations (squares) in a slit pore of pore width 20σ , where σ denotes the molecular diameter obtained by Monte-Carlo simulation; z^* is the reduced distance from the pore wall and ρ^* is the reduced density From [23].

the pore. Corresponding density profiles obtained by Grand Canonical Monte Carlo Simulation (GCMC) for a Lennard-Jones fluid confined to mesoscopic slit-pore are shown in Fig. 4.10. The fluid in the core of pore (in gas and liquid configuration) is – in contrast to the situation in micropores (see Chapter 4.3, Fig. 4.6)- almost structureless, i.e. it does not show the characteristic oscillations observed closer to the pore walls. Hence, in wide mesopores the core fluid can indeed be considered to be bulk-like.

Pore condensation is now understood as first order phase transition between an inhomogeneous gas configuration, which consists of vapor in the core region of the pore in equilibrium with a liquid like adsorbed film (corresponds to configuration C in Fig 4.7), and a liquid configuration, where the pore is filled with liquid (corresponds to configuration D in Fig. 4.7). At the pore critical point of the confined fluid, these two hitherto distinct fluid configurations will become indistinguishable, i.e., a pore condensation step cannot be observed anymore. The suggested order parameter for this phase transition is the difference in surface excess (or adsorbed amounts at low bulk gas densities, i.e., $\Delta V_{(l,g)} = V_{\text{ads(liquid)}} - V_{\text{ads(gas)}}$) between the two inhomogeneous gas and liquid phases and not the difference in orthobaric densities $\Delta\rho$ as it is the case for the corresponding bulk phase transition, which occurs between homogeneous gas and liquid phases.

Accordingly, at the pore critical point $\Delta V_{(l,g)} = 0$ and pore condensation cannot be observed anymore. The critical temperature of the

confined fluid is shifted to lower temperatures, i.e., in contrast to the predictions of the Kelvin equation pore condensation and hysteresis will vanish already at temperatures below T_c . The shift of the critical temperature can be rationalized by the argument that a fluid in narrow pores is an intermediate between a three-dimensional fluid and a one-dimensional fluid for which no critical point exists at $T > 0$. Hence, the shift of the pore critical temperature is correlated with the pore width, i.e., the more narrow the pore, the lower the pore critical temperature. Consequently, at a given subcritical temperature pore condensation is only possible in pores which are wider than the critical pore size W_c .

Adsorption experiments of pure fluids in porous glasses [67-69], silica gel [70] and MCM-41-type of materials [71-73] revealed that pore condensation and hysteresis indeed disappears below the bulk critical temperature. Furthermore, systematic adsorption studies of SF_6 in controlled-pore glasses indicated that hysteresis already disappears below the capillary critical temperature T_{cc} , i.e., reversible pore condensation could be observed (the criterion applied here to determine pore criticality was the disappearance of the pore condensation step) [69].

An experimental study on nitrogen adsorption in MCM-41 silica in combination with the application of density functional theory clearly revealed that the experimental disappearance of hysteresis at the so-called hysteresis critical temperature T_h is indeed not identical with having achieved the pore critical point [71]. Nitrogen sorption hysteresis (at 77K) disappears when the pore diameter is smaller than 4 nm (see Fig. 8.3, chapter 8), however based on the theoretical results the (pseudo)-pore critical point is achieved at a much smaller pore diameter, i.e. 1.8 nm (the bulk critical temperature of nitrogen is 126.2K). This picture was supported by subsequent experimental sorption studies of pure fluids in ordered mesoporous silica materials [72-74]. For instance, experiments to study the temperature dependence of argon adsorption in MCM-41 materials with pore channels of 2.2 nm diameter revealed a hysteresis critical temperature T_h of ca. 62K. In contrast, the pore critical temperature was located at ca. 98K (the bulk critical temperature T_c for argon is 150.7K), i.e., substantial downward shifts in the pore critical and hysteresis critical temperatures are observed for such narrow pores [73].

These systematic studies also revealed that temperature and pore size can be considered as complementary variables with regard to their influence on the occurrence of hysteresis: an increase in temperature has qualitatively a similar effect as a decrease in pore size. Both lead to a decrease in the width of the hysteresis loop, which eventually disappears at a certain critical pore size and temperature (T_h), which is illustrated in Fig 4.11.

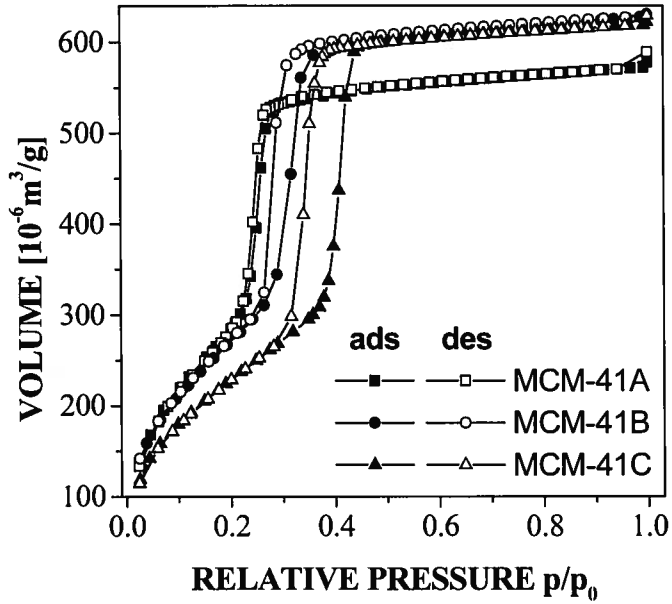


Figure 4.11a Adsorption of argon at 77 K in MCM-41 silica as a function of pore diameter: MCM-41A, $d_p = 3.30$ nm; MCM-41B, $d_p = 3.66$ nm; MCM-41C, $d_p = 4.25$ nm. From [80a].

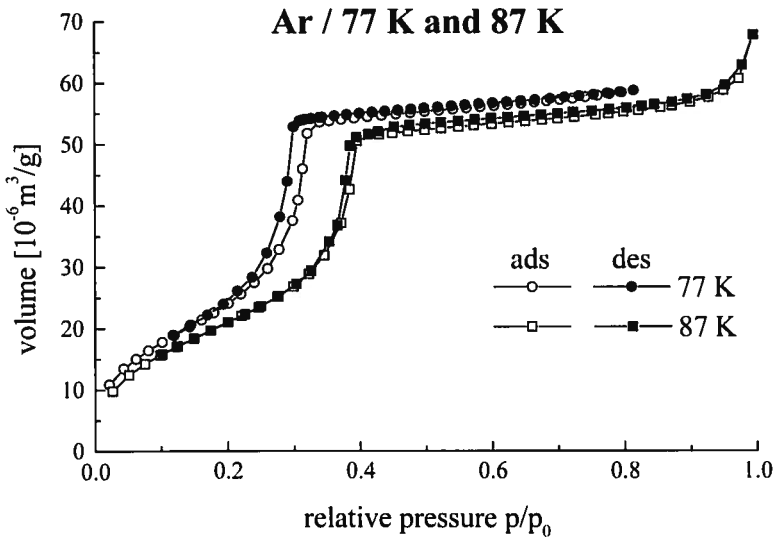


Figure 4.11b. Effect of temperature on hysteresis. Argon sorption at 77K and 87K on MCM-48 silica ($d_p = 4.01$ nm). From [80b].

The effect of pore size on hysteresis is shown in Fig. 4.11a, where the hysteresis behavior of argon adsorption isotherms at 77.35K is shown for various MCM-41 silica samples, which exhibit different mode pore diameter (MCM-41A: 3.30 nm, MCM-41 B: 3.66 nm, MCM-41 C: 4.25 nm). It can be clearly seen that the width of the hysteresis loop decreases with decreasing pore size and disappears for the MCM-41 silica A. Fig. 4.11b shows the effect of temperature on hysteresis. Argon adsorption was measured at 77 K and 87 K on an MCM-48 silica sample of pore diameter 4.01 nm. The width of the hysteresis decreases significantly as the temperature is increased from 77 K to 87 K.

In addition to the shift in critical temperature, experiments and theory indicate that as a result of the combined effects of fluid-wall forces and finite-size the freezing temperature and triple point of the pore fluid may also be shifted to lower temperature relative to the bulk triple point if the wall-fluid attraction is not too strong, i.e., the pore wall does not prefer the solid phase [75-79]. This is for instance the case for silica materials. The amount of the shift depends again on the pore size, i.e., the more narrow the pore size the larger the shift of the pore triple point region. Hence, pore condensation can also be observed at temperatures below the bulk triple point temperature [44,88], as it is shown in Figure. 4.11 for argon sorption at 77 K in the narrow pores of MCM-48 and MCM-41 silica. However, systematic sorption experiments of nitrogen and argon adsorption at 77 K and 87 K in mesoporous molecular sieves and controlled pore glasses by Thommes et al. [43a,80] indicate that pore condensation of argon adsorption at 77.35 K cannot be observed anymore if the pore diameter exceeds *ca.* 15 nm, which limits the range for pores size analysis with argon at 77K. This behavior could be related to confinement effects on the location of the (quasi)-triple point of the pore fluid. The effect of confinement on the phase behavior of a pore fluid is also important for thermoporometry, a technique where the effect of confinement on the suppression of the freezing or melting temperature is used to determine the pore size.

In summary, theoretical and experimental studies have led to the conclusion that the complete coexistence curve of a fluid confined for instance to mesoporous silica materials is shifted to lower temperature and higher mean density [67, 69, 71] (see also the review of Gelb et al [66]). Fig. 4.12 shows a schematic phase diagram of bulk- and pore fluid (confined to different sized, single pores) which illustrates the influence of confinement on the sorption and phase behavior as it can be found for instance in case of mesoporous silica. According to this phase diagram, one can separate the following regimes: (i) continuous pore filling without pore condensation step occurs below a certain critical pore width (w_c) at a given temperature $T < T_c$. For a given pore size (w) continuous pore filling can be observed above the pore critical temperature T_{wc} . (and, of course, above the bulk critical temperature); (ii) Reversible pore condensation occurs for pore sizes

between the critical pore size w_c and the pore size where hysteresis disappears (w_h), i.e., in the pore size range $w_c < w < w_h$; or in case of fixed pore size in the temperature range between the hysteresis critical temperature T_h and the pore critical temperature T_{wc} ; (iii) Pore condensation with hysteresis occurs for pore sizes larger than w_h at temperatures below T_h .

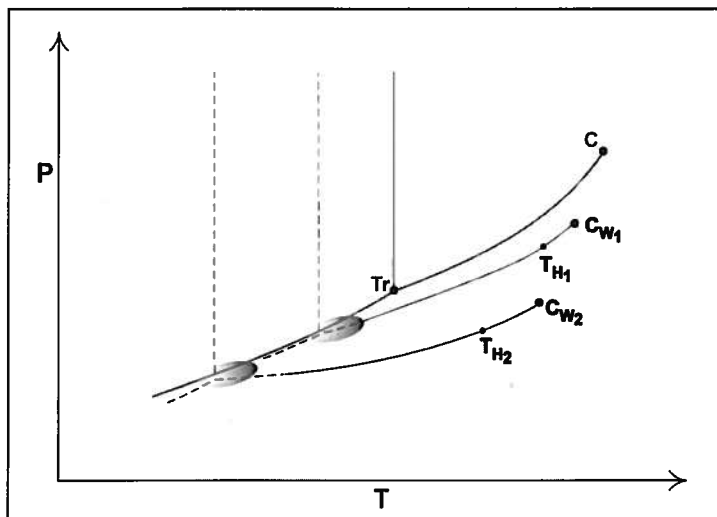


Figure 4.12 Schematic phase diagram of a bulk and pore fluid confined to different sized, single pores of widths $w_1 > w_2$. From [43a]. The pore condensation lines, i.e., the locus of states of the unsaturated vapor at which pore condensation will occur end in the appropriate pore critical points C_{w1} and C_{w2} , with $T_{Cw1} > T_{Cw2}$. For a given experimental temperature, pore condensation will occur first in the pore of width w_2 , and a higher (relative) pressure in the larger pore w_1 . The temperatures T_{H1} and T_{H2} are the so-called hysteresis critical temperatures, where experimental hysteresis disappears. Details of the sorption and phase behavior below the bulk triple point (Tr) as well as the nature of quasi-triple points is still under investigation [76-81] and these regions of the phase diagram are indicated by dashed lines and the grey areas. Please note, that from a theoretical point of view, real phase transitions and therefore real criticality cannot occur in pseudo-one dimensional cylindrical pores, i.e., pore condensation and the pore critical point should therefore be considered here as pseudo-phase transition and pseudo-critical point, respectively.

These observations clearly reveal that the shape of sorption isotherms does not depend only on the texture of the porous material, but also on the difference of thermodynamic states between the confined fluid and bulk fluid phase. This has to be taken into account for the characterization of porous media by gas adsorption. However, macroscopic, thermodynamic approaches related to the Kelvin equation do not account for these effect (these approaches predict the occurrence of pore condensation

up to the bulk critical temperature) and therefore fail to describe correctly the position of the pore condensation step in narrow mesopores, in particular in a temperature and pore size range where hysteresis disappears. In combination with other deficiencies of the Kelvin equation based methods, this leads to significant errors in the pore size analysis (see chapter 8, Fig. 8.3).

4.5 REFERENCES

1. Langmuir I. (1918) *J. Am. Chem. Soc.* **40**, 1368.
2. Brunauer S., Emmett P.H. and Teller E. (1938) *J. Am. Chem. Soc.* **60**, 309.
3. Frenkel J. (1946) *Kinetic Theory of Liquids*, Oxford University Press.
4. Halsey G.D. (1948) *J. Chem. Phys.* **16**, 931.
5. Hill T.L. (1952) *Advances in Catalysis IV*, Academic Press, N.Y., 236.
6. Loering R. and Findenegg G.H. (1984) *J. Chem. Phys.* **81**, 3270.
7. Carrott P.J., McLeod A.I. and Sing K.S.W. (1982) In *Adsorption at the Gas-Solid and Liquid-Solid Interface* (Rouquerol J. and Sing K.S.W., eds.) Elsevier, Amsterdam.
8. Loering R. and Findenegg G.H. (1981) *J. Colloid Interface Sci.* **84**, 355.
9. Findenegg G.H. and Thommes M. (1997) In *Physical Adsorption: Experiment, Theory, and Application* (Fraissard J. and Conner C., eds.) Kluwer, Dordrecht, Netherlands.
10. Steele W.A. (1974) *The Interaction of Gases with Solid Surfaces*, Chapter 5, Pergamon Press, Oxford.
11. Sing K.S.W., Everett D.H., Haul R.A.W., Moscou L., Pierotti R.A., Rouquerol J. and Siemieniowska T. (1985) *Pure Appl. Chem.* **57**, 603.
12. Marsh H. (1987) *Carbon* **25**, 49.
13. Polanyi M. (1914) *Verh. Dtsch. Phys. Ges.* **16**, 1012.
14. ^(a)Dubinin M.M. and Timofeev D.P. (1948) *Zh. Fiz. Khim.* **22**, 133; ^(b)Dubinin M.M. and Radushkevich L.V. (1947) *Dokl. Akad. Nauk. SSSR* **55**, 331.
15. Dubinin M.M. (1960) *Chem. Rev.* **60**, 235.
16. Dubinin M.M. and Astakhov V.A. (1970) *Adv. Chem. Series.* **102**, 69.
17. ^(a)Stoeckli F. (1977) *J. Colloid Interface Sci.* **59**, 184; ^(b)Dubinin M.M. and Stoeckli H.F. (1980) *J. Colloid Interface Sci.* **75**, 34; ^(c)Stoeckli F., Lavanchy A. and Kraehenbuehl F. (1982) In *Adsorption at the Gas-Solid and Liquid-Solid interface* (Rouquerol J. and Sing K.S.W., eds.) Elsevier, Amsterdam.
18. Horvath G. and Kawazoe K. (1983) *J. Chem. Eng. Japan.* **16**, 474.
19. ^(a)Saito A. and Foley H.C. (1991) *Am. Inst. Chem. Eng. J.* **37**, 429; ^(b)Saito A. and Foley H.C. (1995) *Microporous Materials* **3**, 531; ^(c)Cheng L.S. and Yang R.T. (1994) *Chem. Eng. Sci.* **49**, 2599.
20. ^(a)Evans R., Marconi U.M.B., and Tarazona P. (1986) *J. Chem. Soc. Faraday Trans.* **82**, 1763; ^(b)Tarazona P., Marconi U.M.B. and Evans R. (1987) *Mol. Phys.* **60**, 573.
21. Peterson B.K., Walton J.P.R.B. and Gubbins K.E. (1986) *J. Chem. Soc. Faraday Trans.* **82**, 1789.
22. ^(a)Gubbins K.E. (1997) In *Physical Adsorption: Experiment, Theory and Applications* (Fraissard J., ed.) Kluwer, Dordrecht, Netherlands; ^(b)Peterson B.K., Gubbins K.E., Heffelfinger G.S., Marconi U.M.B. and van Swol F. (1988) *J. Chem. Phys.* **88**, 6487.
23. Walton J.P.R.P. and Quirke N. (1989) *Mol. Simul.* **2**, 361.
24. Heinbuch U. and Fischer J. (1987) *Chem. Phys. Lett.* **135**, 587.
25. Seaton N.A., Walton J.R.B. and Quirke N. (1989) *Carbon* **27**, 853.
26. Lastoskie C.M., Gubbins K. and Quirke N. (1993) *J. Phys. Chem.* **97**, 4786.
27. Olivier J.P., Conklin W.B. and v. Szombathley M. (1994) *Stud. Surf. Sci. Catal.* **87**, 81.
28. Neimark A.V. (1995) *Langmuir* **11**, 4183; Neimark A.V., Ravikovitch P.I., Grün M.,

- Schüth F. and Unger K.K. (1998) *J. Colloid Interface Sci.* **207**, 159; Ravikovitch P.I., Vishnyakov A. and Neimark A.V. (2001) *Phys. Rev. E*, **64**, :011602.
29. ^(a)Jagiello J. (2003) *personal communication*, ^(b)Jagiello J. (1998) In *Fundamentals of Adsorption* **6**, (Meunier F.D., ed.) Elsevier, Amsterdam.
 30. Linden M., Schacht S., Schueth F., Steel A. and Unger K. (1998) *J. Porous Mater.* **5**, 177.
 31. ^(a)Thompson W.T. (1871) *Philos. Mag.* **42**, 448; ^(b)Zsigmondy Z. (1911) *Anorg. Chem.* **71**, 356.
 32. Adamson A.W. and Gast A.P. (1997) *Physical Chemistry of Surfaces*, 6th edn, Wiley-Interscience, New York.
 33. Cohan L.H. (1938) *J. Am. Chem. Soc.* **60**, 433; Cohan L.H. (1944) *J. Am. Chem. Soc.* **66**, 98.
 34. Barrett E.P., Joyner L.G. and Halenda P.P. (1951) *J. Am. Chem. Soc.* **73**, 373.
 35. ^(a)Broekhoff J.C.P. and de Boer J.H. (1967) *J. Catal.* **9**, 8; ^(b)Broekhoff J.C.P. and de Boer J.H. (1967) *J. Catal.* **9**, 15; ^(c)Broekhoff J.C.P. and de Boer J.H. (1968) *J. Catal.* **10**, 377; ^(d)Broekhoff J.C.P. and de Boer J.H. (1968) *J. Catal.* **10** 368.
 36. Cole M.W. and Saam W.F. (1974) *Phys. Rev. Lett.* **32**, 985.
 37. De Boer J.H. (1958) *The Structure and Properties of Porous Materials*, Butterworths, London.
 38. Foster A.G. (1932) *Trans. Faraday Soc.* **28**, 645.
 39. Cassell H.M. (1944) *J. Phys. Chem.* **48**, 195.
 40. Everett D.H. (1967) In *The Solid-Gas Interface Vol.2* (Flood E.A., ed.) Marcel Decker, New York.
 41. Ball P.C. and Evans R. (1989) *Langmuir* **5**, 714.
 42. ^(a)Neimark A.V., Ravikovitch P.I. and Vishnyakov A. (2000) *Phys. Rev. E* **62**, R1493; ^(b)Neimark A.V. and Ravikovitch P.I. (2001) *Microporous and Mesoporous Materials* **44-56**, 697.
 43. ^(a)Thommes M., Koehn R. and Froeba M. (2002) *Appl. Surf. Sci.* **196**, 239; ^(b) Thommes M. (in press) In *Nanoporous Materials: Science and Engineering* (Max Lu, ed.) World Scientific, chapter 11.
 44. Awschalom D.D., Warnock J. and Shafer M.W. (1986) *Phys. Rev. Lett.* **57**, 1607.
 45. Findenegg G.H., Gross S. and Michalski T. (1994) *Stud. Surf. Sci. Catal.* **87**, 71.
 46. Mc Bain J.W. (1932) *J. Am. Chem. Soc.* **57**, 699.
 47. Mason G. (1982) *J. Colloid Interface Sci.* **88**, 36.
 48. Wall G.C. and Brown R.J.C. (1981) *J. Colloid Interface Sci.* **82**, 141.
 49. Neimark A.V. (1991) *Stud. Surf. Sci. Catal.* **62**, 67.
 50. Parlar M. and Yortsos Y.C. (1988) *J. Colloid Interface Sci.* **124**, 162.
 51. ^(a)Zhu H., Zhang L. and Seaton N.A. (1993) *Langmuir* **9**, 2576; ^(b)Liu, H. and Seaton N.A. (1994) *Chem. Eng. Sci.* **49**, 1869.
 52. Rojas F., Kornhauser I., Felipe C., Esparza J.M., Cordero S., Dominguez A. and Riccardo J.L. (2002) *Phys. Chem. Chem. Phys.* **4**, 2346.
 53. Page J.H., Liu L., Abeles B., Herbolzheimer E., Deckmann H.W. and Weitz D.A. (1995) *Phys. Rev. E.* **52**, 2763.
 54. Hoinkis E. and Roehl-Kuhn B. (1992) In *Fundamentals of Adsorption* **7**, (Kaneko K., Kanoh H. and Hanzawa Y., eds.) IK International Ltd, Chiba City, Japan.
 55. Sarkisov L. and Monson P.A. (2001) *Langmuir* **17**, 7600.
 56. Ravikovitch P.I. and Neimark A.V. (2002) *Langmuir* **18**, 9830.
 57. Burgess C.G.V. and Everett D.H. (1970) *J. Colloid Interface Sci.* **33**, 611.
 58. Gregg S.J. and Sing K.S.W. (1982) *Adsorption, Surface Area and Porosity* 2nd edn, Academic Press, London.
 59. Gubbins K.E. (2002) In *Fundamentals of Adsorption* **7** (Kaneko K., Kanoh H. and Hanzawa Y., eds.) IK International Ltd, Chiba City, Japan.
 60. ^(a)Gelb L.D. and Gubbins K.E. (1998) *Langmuir* **14**, 2097; ^(b)Gelb L.D. (2002) In:

Fundamentals of Adsorption 7 (Kaneko K., Kanoh H. and Hanzawa Y., eds.) IK International Ltd, Chiba City, Japan.

61. Page K.S. and Monson P.A. (1996) *Phys. Rev. E* **54**, 6557.
62. Kierlik E., Rosinberg M.L., Tarjus G., and Viot P. (2001) *Phys. Chem. Chem. Phys.* **3**, 1201.
63. Woo H.J., Sarkisov L. and Monson P.A. (2001) *Langmuir* **17**, 7472.
64. Evans R.J. (1990) *Phys. Condens. Matter* **2**, 8989.
65. Votyakov E.V., Tovbin Y.U.K., MacElroy J.M.D. and Roche A. (1999) *Langmuir* **15**, 5713.
66. Celstini F. (1997) *Phys. Lett. A* **228** 84.
67. Gubbins K.E. (1997) In: *Physical Adsorption: Experiment, Theory and Application*, (Fraissard J., ed.) Kluwer, Dordrecht, Netherlands.
68. Gelb L.D., Gubbins K.E., Radhakrishnan R. and Sliwinska-Bartkowiak M. (1999) *Rep. Prog. Phys.* **62**, 1573.
67. Burgess C.G.V., Everett D.H. and Nuttall S. (1989) *Pure Appl. Chem.* **61**, 1845.
68. De Keizer A., Michalski T. and Findenegg G.H. (1991) *Pure Appl. Chem.* **63**, 1495.
69. Thommes M. and Findenegg G.H. (1994) *Langmuir* **10**, 4270.
70. Machin W.D. (1994) *Langmuir* **10**, 1235.
71. Groß S. and Findenegg G.H. (1997) *Ber. Bunsenges. Phys. Chem.* **101**, 1726.
72. Ravikovitch P.I., Domhnail S.C.O., Neimark A.V., Schueth F. and Unger K.K. (1995) *Langmuir* **11**, 4765.
73. ^(a)Morishige K. and Shikimi M. (1997) *Langmuir* **13**, 3494; ^(b)Morishige K. and Shikimi M. (1998) *J. Chem. Phys.* **108**, 7821.
74. ^(a)Sonwane C.G. and Bhatia S.K. (2000) *J. Phys. Chem B* **104**, 9099; ^(b)Bhatia S.K. and Sonwane C.G. (1998) *Langmuir* **14**, 1521.
75. Dominguez H., Allen M.P. and Evans R. (1998) *Mol. Phys.* **96**, 209.
76. Fretwell H.M., Duffy J.A., Clarke A.P., Alam M.A. and Evans R. (1995) *J. Phys. Condens. Matter* **7**, L717.
77. Coulomb J.P., Grillet Y., Lewellyn P.L., Martin C. and Andre G. (1998) In: *Fundamentals of Adsorption*, (Meunier F., ed.) Elsevier, Paris.
78. Morishige K., Kawano K. and Hayashigi T. (2000) *J. Phys. Chem B* **104**, 10298.
79. Huber P. and Knorr K. (1999) *Phys. Rev. B* **60**, 12657.
80. ^(a)Thommes M., Koehn R. and Froeba M. *to be published*; ^(b)Thommes M., Koehn R. and Froeba M. (2000) *J. Phys. Chem B* **104**, 7932.
81. Myahara M., Sakamoto M., Kandra H. and Higashitani K. (2002) *Stud. Surf. Sci. Catal.* **144**, 411.

5 Surface Area Analysis from the Langmuir and BET Theories

5.1 SPECIFIC SURFACE AREA FROM THE LANGMUIR EQUATION

The Langmuir [1] equation is more applicable to chemisorption (see chapter 12), where a chemisorbed monolayer is formed, but is also often applied to physisorption isotherms of type I. Although this type of isotherm is usually observed with microporous adsorbents, due to the high adsorption potential, a separation between monolayer adsorption and pore filling is not possible for many such adsorbents. A convenient form of the Langmuir equation is

$$\frac{P}{W} = \frac{1}{KW_m} + \frac{P}{W_m} \quad (\text{cf. 4.12})$$

where P is the adsorbate equilibrium pressure, and W and W_m are the adsorbed weight and monolayer weights, respectively. The term K is a constant discussed in §4.1.

For type I isotherms, a plot of P/W versus P should give a straight line with $1/W_m$ as the slope. The sample surface area, S_t , is calculated from equation (4.13):

$$S_t = N_m A_x = \frac{W_m \bar{N} A_x}{\bar{M}} \quad (\text{cf. 4.13})$$

where, A_x is the cross-sectional adsorbate area, \bar{M} is the adsorbate molecular weight, and \bar{N} is Avogadro's number. The fact that a Langmuir plot gives a straight line if applied to a type I isotherm is not at all indicative of its success. Without an understanding of the processes occurring within the micropores in terms of adsorption or pore filling, the Langmuir equation may be a correct mathematical description of the isotherm, but the determined monolayer capacity W_m and the corresponding specific surface does not reflect a true surface areas, but rather an equivalent or characteristic surface area.

5.2 SPECIFIC SURFACE AREA FROM THE BET EQUATION

5.2.1 BET-Plot and Calculation of the Specific Surface Area

Although derived over sixty-five years ago, the application of the BET equation is still the most popular approach for the calculation of the specific surface area. The determination of surface areas from the BET theory [2] is a straightforward application of the BET equation, which was derived in chapter 4.

$$\frac{1}{W[P/P_0 - 1]} = \frac{1}{W_m C} + \frac{C-1}{W_m C} \left(\frac{P}{P_0} \right) \quad (\text{cf. 4.38})$$

A plot of $1/W[P_0/P - 1]$ versus P/P_0 , as shown in Fig. 5.1, will yield a straight line usually in the range $0.05 \leq P/P_0 \leq 0.35$.

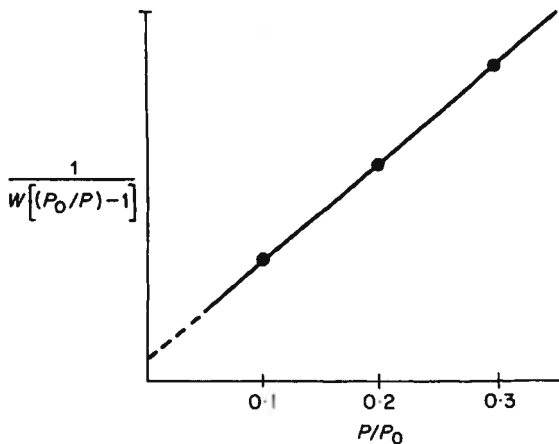


Figure 5.1 Typical BET plot.

The slope s and the intercept i of a BET plot are, respectively,

$$s = \frac{C-1}{W_m C} \quad (5.1)$$

$$i = \frac{1}{W_m C} \quad (5.2)$$

Solving the preceding equations for W_m , the weight adsorbed in a monolayer gives

$$W_m = \frac{1}{s+i} \quad (5.3)$$

and the solution for C , the BET constant, gives

$$C = \frac{s}{i} + 1 \quad (5.4)$$

The total surface area can be calculated from equation (4.13), viz.,

$$S_t = \frac{W_m \bar{N} A_x}{\bar{M}} \quad (\text{cf 4.13})$$

where, as before, A_x is the cross-sectional adsorbate area, \bar{M} is the adsorbate molecular weight, and \bar{N} is Avogadro's number. The specific surface area can be determined by dividing S_t by the sample weight.

5.2.2. The Meaning of Monolayer Coverage

Hill [3] has shown that when sufficient adsorption has occurred to cover the surface with exactly one layer of molecules, the fraction of surface, $(\theta_0)_m$, not covered by any molecule is dependent on the BET C value and is given by

$$(\theta_0)_m = \frac{\sqrt{C}-1}{C-1} \quad (5.5)$$

It is evident from equation (5.5) that when sufficient adsorption has occurred to form a monolayer there is still always some fraction of surface unoccupied. Indeed, only for C values approaching infinity will θ_0 approach zero and in such cases the high adsorbate-surface interaction can only result from chemisorption. For nominal C values, say near 100, the fraction of surface unoccupied, when exactly sufficient adsorption has occurred to form a monolayer, is 0.091. Therefore, on the average each occupied site contains about 1.1 molecules. The implication here is that the BET equation indicates the weight of adsorbate required to form a single molecular layer on the surface, although no such phenomenon as a uniform monolayer exists in the case of physical adsorption.

5.2.3 The BET Constant and Site Occupancy

Equation (5.5) is used to calculate the fraction of surface unoccupied when $W = W_m$, that is, when just a sufficient number of molecules have been adsorbed to give monolayer coverage. Lowell [4] has derived an equation that can be used to calculate the fraction of surface covered by adsorbed molecules of one or more layers in depth. Lowell's equation is

$$(\theta_i)_m = C \left(\frac{\sqrt{C} - 1}{C - 1} \right)^{i+1} \quad (5.6)$$

where θ_i represents the fraction of surface covered by layers i molecules deep. The subscript m denotes that equation is valid only when sufficient adsorption has occurred to make $W = W_m$. Table 5.1 shows the fraction of surface covered by layers of various depths, as calculated from equation for $i = 0$ and for $i \neq 0$, as a function of the BET C value.

Equations (5.5) and (5.6) should not be taken to mean that the adsorbate is necessarily arranged in neat stacks of various heights. Rather, it should be understood as an indication of the fraction of surface covered with the equivalent of i molecules regardless of their specific arrangement, lateral mobility, and equilibrium with the vapor phase.

Of further interest is the fact that when the BET equation is solved for the relative pressure corresponding to monomolecular coverage, ($W = W_m$), one obtains

$$\left(\frac{P}{P_0} \right)_m = \frac{\sqrt{C} - 1}{C - 1} \quad (5.7)$$

The subscript m above refers to monolayer coverage. Equating (5.6) and (5.7) produces the interesting fact that

$$\theta_0 = \left(\frac{P}{P_0} \right)_m \quad (5.8)$$

That is, the numerical value of the relative pressure required to make W equal to W_m is also the fraction of surface unoccupied by adsorbate.

Table 5.1 Values for $(\theta)_m$ from equations (5.5) and (5.6).

	C = 1000	C = 100	C = 10	C = 1
0	0.0307	0.0909	0.2403	0.5000
1	0.9396	0.8264	0.5772	0.2500
2	0.0288	0.0751	0.1387	0.1250
3	0.0009	0.0068	0.0333	0.0625
4		0.0006	0.0080	0.0313
5		0.0001	0.0019	0.0156
6			0.0005	0.0078
7			0.0001	0.0039
8				0.0019
9				0.0009
10				0.0005
11				0.0002
				0.0001

5.2.4 The Single Point BET Method

The BET theory requires that a plot of $1/W[(P_0/P)-1]$ versus P/P_0 be linear with a finite intercept (see equation (4.38) and Fig. 5.1). By reducing the experimental requirement to only one data point, the single point method offers the advantages of simplicity and speed often with little loss in accuracy. The slope s and the intercept i of a BET plot are

$$s = \frac{C-1}{W_m C} \quad (\text{cf. 5.1})$$

$$i = \frac{1}{W_m C} \quad (\text{cf. 5.2})$$

Then

$$\frac{s}{i} = C-1 \quad (5.9)$$

For reasonably high values of C the intercept is small compared to the slope and in many instances may be taken as zero. With this approximation, equation (4.38), the BET equation, becomes

$$\frac{1}{W[(P/P_0)-1]} = \frac{C-1}{W_m C} \left(\frac{P}{P_0} \right) \quad (5.10)$$

Since $1/W_m C$, the intercept, is assumed to vanish, equation (5.11) reduces to

$$W_m = W(1 - P/P_0) \quad (5.11)$$

The total surface area as measured by the single point method, is then calculated as:

$$S_t = W \left(1 - \frac{P}{P_0} \right) \frac{\bar{N}}{M} A_x \quad (5.12)$$

5.2.5 Comparison of the Single Point and Multipoint Methods

The error introduced by the single point method can be evaluated by examining the difference between W_m as determined by equations (5.11) and (4.38), the BET equation. Solving equation (4.38) for W_m gives

$$W_m = W \left(\frac{P_0}{P} - 1 \right) \left[\frac{1}{C} + \frac{C-1}{C} \left(\frac{P}{P_0} \right) \right] \quad (5.13)$$

Subtracting equation (5.11) from (5.13) and dividing by equation gives the relative error associated with the single point method, that is,

$$\frac{(W_m)_{mp} - (W_m)_{sp}}{(W_m)_{mp}} = \frac{1 - P/P_0}{1 + (C-1)P/P_0} \quad (5.14)$$

The subscripts *mp* and *sp* refer to the multi- and single point methods, respectively. Table 5.2 shows the relative error of the single point method compared to the multipoint method as a function of P/P_0 as calculated from equation (5.14). The last column of Table 5.2 is established by substituting equation (4.46) into equation (5.12) for the special case when $P/P_0 = (P/P_0)_m$, thus

$$\frac{(W_m)_{mp} - (W_m)_{sp}}{(W_m)_{mp}} = \frac{\sqrt{C}-1}{C-1} = \left(\frac{P}{P_0} \right)_m = \theta_0 \quad (5.15)$$

Table 5.2 Relative errors using the single point method at various relative pressures.

C	$P/P_0 = 0.1$	$P/P_0 = 0.2$	$P/P_0 = 0.3$	$(P/P_0)_m^*$
1	0.90	0.80	0.70	0.50
10	0.47	0.29	0.17	0.24
50	0.17	0.07	0.04	0.12
100	0.08	0.04	0.02	0.09
1000	0.009	0.004	0.002	0.003

* $(P/P_0)_m$ is the relative pressure that gives monolayer coverage according to a multipoint determination.

The surprising relationship above shows that when a single point analysis is made using the relative pressure that would give monolayer coverage according to the multipoint theory, the relative error will be equal to the relative pressure employed. The error will also, according to equation (4.44), be equal to the fraction of surface unoccupied. A more explicit insight into the mathematical differences of the multi- and single point methods is obtained by considering a single point analysis using a relative pressure of 0.3 with a corresponding multipoint C value of 100. From equation (5.11), the single point BET equation, one obtains

$$(W_m)_{sp} = 0.7W_{0.3} \quad (5.16)$$

The term $(W_m)_{sp}$ refers to the monolayer weight as determined by the single point method, and $W_{0.3}$ is the experimental weight adsorbed at a relative pressure of 0.3. From equation (4.46) the relative pressure required for monolayer coverage is

$$\left(\frac{P}{P_0}\right)_m = \frac{\sqrt{100-1}}{100-1} = 0.0909 \quad (5.17)$$

Using equation (5.13), the multipoint equation, to find W_m gives

$$W_m = W_{0.3}(3.33-1) \left[\frac{1}{100} + \frac{100-1}{100}(0.3) \right] = 0.715W_{0.3} \quad (5.18)$$

Comparison of equations (5.18) and (5.16) shows that the difference between the single and multipoint methods is identical to that shown in Table 5.2 for $P/P_0 = 0.3$ and $C = 100$; viz.,

$$\frac{0.715 - 0.700}{0.715} = 0.02 \quad (5.19)$$

The above analysis discloses that, when the BET C value is 100, the single point method using a relative pressure more than three times that required for monolayer coverage causes an error of only 2%. To further understand the BET equation and the relationship between the C value and the single point error it is useful to rewrite the equation (4.38), the BET equation, as

$$\frac{W}{W_m} = \frac{C(P/P_0)}{[1 + (C-1)P/P_0](1 - P/P_0)} \quad (5.20)$$

Using the method of partial fractions, the right side of equation (5.20) can be written as

$$\frac{C(P/P_0)}{[1 + (C-1)P/P_0](1 - P/P_0)} = \frac{X}{1 - P/P_0} - \frac{Z}{1 + (C-1)P/P_0} \quad (5.21)$$

Recognizing that $X = Z = 1$ is a solution, gives

$$\frac{W}{W_m} = \frac{1}{1 - P/P_0} - \frac{1}{1 + (C-1)P/P_0} \quad (5.22)$$

Equation (5.22) is the BET equation expressed as the difference between two rectangular hyperbolas. If the value of C is taken as infinity, equation (5.22) immediately reduces to equation (5.11), the single point BET equation. The hyperbolae referred to above are shown below in Fig. 5.2.

As indicated in Fig. 5.2, curve Y, the BET curve for an arbitrary C value, approaches curve X, the single point curve, as the value of C increases. In the limiting case of $C \rightarrow \infty$, the BET curve is coincident with the single point curve. For all other C values, the single point curve lies above the BET curve and their difference vanishes as the relative pressure approaches unity. Thus, as the value of C increases, the knee of the isotherm becomes sharper and moves toward lower relative pressures (see also Fig. 5.3). For lower C values, curves X and Y diverge and higher relative pressures must be used to make single point surface areas conform to those obtained by the multipoint method.

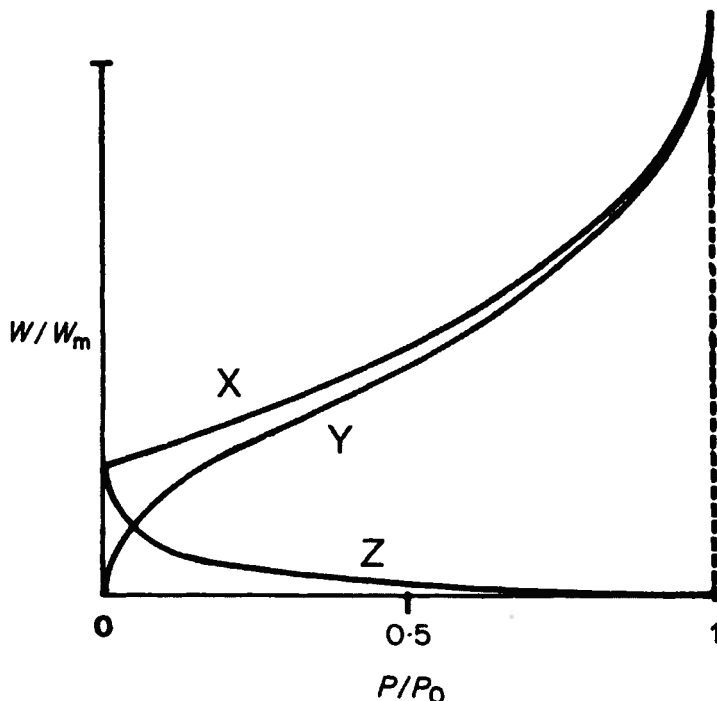


Figure 5.2 Plot of the hyperbola from equation (5.14) using an arbitrary C -value. Curve $X = 1/(1 - P/P_0)$; curve $Z = 1/(1 + (C - 1)P/P_0)$; curve $Y = X - Z$.

The extent of divergence of curves X and Y is controlled, in a mathematical sense, by the second term in equation (5.21). This term contains the C value.

Table 5.2 indicates that, regardless of the C value, using higher relative pressures *within the linear range* reduces the relative error. Similarly, Fig. 5.2 shows that at sufficiently high relative pressure the BET curve and the single point curve merge regardless of the C value. It would appear that all single point analyses should be performed at the highest possible relative pressures. Although theoretically sound, the use of relative pressures above 0.3 can lead to serious errors on the large number of samples that contain pores. In a later chapter, the influence of pores is discussed, but here it is sufficient to note that once condensation in pores commences, the BET equation, which deals only with adsorption, fails adequately to describe the state of the system. Ample evidence is available to indicate that many adsorbents possess pores which causes condensation at relative pressures as small as 0.3 and in some cases at even lower values. Therefore, relative pressures of 0.3 may be considered sufficiently high to

give good agreement with multipoint measurements on most surfaces while avoiding condensation in all but microporous samples.

When used for quality control, the error associated with the single point method can be eliminated or greatly reduced if an initial multipoint analysis is performed to obtain the correct C value. Then equation (5.14) can be used to correct the results. Even an approximate value of C can be used to estimate the single point error. However, on the great majority of surfaces, the C value is sufficiently high to reduce the single point error to less than 5%.

5.2.6 Applicability of the BET Theory

As already stated before, the BET theory continues to be almost universally used because of its simplicity, its definitiveness, and its ability to accommodate each of the five isotherm types. The mathematical nature of the BET equation in its most general form, equation (4.39) gives the Langmuir or type I isotherm when $n = 1$. Plots of W/W_m versus P/P_0 using equation (4.38) conforms to type II or type III isotherms for C values greater than and less than 2, respectively. Fig. 5.3 shows the shape of several isotherms for various values of C . The data for Fig. 5.3 are shown in Table 5.3 with values of W/W_m calculated from equation after rearrangement to

$$\frac{W}{W_m} = \left(1 - \frac{P}{P_0}\right) + \frac{1}{C} \left(\frac{P}{P_0} + \frac{P_0}{P} - 2\right) \quad (5.23)$$

The remaining two isotherms, types IV and V, are modifications of the type II and type III isotherms due to the presence of pores.

Rarely, if ever, does the BET theory exactly match an experimental isotherm over its entire range of relative pressures. In a qualitative sense, however, it does provide theoretical foundation for the various isotherm shapes.

Of equal significance is the fact that in the region of relative pressures near completed monolayers ($0.05 \leq P/P_0 \leq 0.3$) the BET theory and experimental isotherms do agree very well, leading to a powerful and extremely useful method of surface area determination. The fact that most monolayers are completed in the range $0.05 \leq P/P_0 \leq 0.3$ reflects the value of most C constants. As shown in Table 5.3, the value of W/W_m equals unity in the previous range of relative pressures for C values between 3 and 1000, which covers the great majority of all isotherms.

The sparsity of data regarding type III isotherms, with C values of 2 or less, leaves open the question of the usefulness of the BET method for determining surface areas when type III isotherms are encountered. Often

Table 5.3 Values of W/W_m and relative pressures for various values of C .

P/P_0	$C = 0.05$	$C = 0.5$	$C = 1$	$C = 2$	$C = 3$	$C = 10$	$C = 100$	$C = 1000$
0.02	0.001	0.010	0.020	0.040	0.059	0.173	0.685	0.973
0.05	0.003	0.027	0.052	0.100	0.143	0.362	0.884	1.030
0.10	0.006	0.058	0.111	0.202	0.278	0.585	1.020	1.100
0.20	0.015	0.139	0.250	0.417	0.536	0.893	1.200	1.250
0.30	0.030	0.253	0.429	0.660	0.804	1.160	1.400	1.430
0.40	0.054	0.417	0.667	0.952	1.110	1.450	1.640	1.660
0.50	0.095	0.667	1.000	1.330	1.500	1.820	1.980	2.000
0.60	0.172	1.060	1.490	1.870	2.040	2.340	2.480	2.500
0.70	0.345	1.790	2.330	2.740	2.910	3.190	3.320	3.330
0.80	0.833	3.330	4.000	4.440	4.620	4.880	4.990	5.000
0.90	3.330	8.330	9.090	9.520	9.680	9.900	9.990	10.000
0.94	7.350	14.700	15.700	16.200	16.300	16.600	16.700	16.700

in this case it is possible to change the adsorbate to one with a higher C value, thereby changing the isotherm shape. Brunauer *et al* [5], however, point to considerable success in calculating the surface area from type III isotherms as well as predicting the temperature coefficient of the same isotherms.

Despite of the success of the BET theory, some of the assumptions upon which it is founded are not above criticism. One questionable assumption is that of an energetically homogeneous surface, that is, all the adsorption sites are energetically identical. Further, the BET model ignores the influence of lateral adsorbate interactions.

Brunauer [6] answers these criticisms by pointing out that lateral interaction between adsorbate molecules necessarily increases as the surface becomes more completely covered. The interaction with the surface, however, decreases with increasing adsorption up to monolayer coverage since on an energetically heterogeneous surface the high energy sites will be occupied at lower relative pressures. In this situation, occupancy of the lower energy sites occurs nearer to completion of the monolayer.

Fig.5.4 illustrates how the lateral interactions and the surface interactions can sum to a nearly constant overall adsorption energy up to completion of the monolayer, an implicit assumption of the BET theory. This results in a constant C value from equation (4.22)

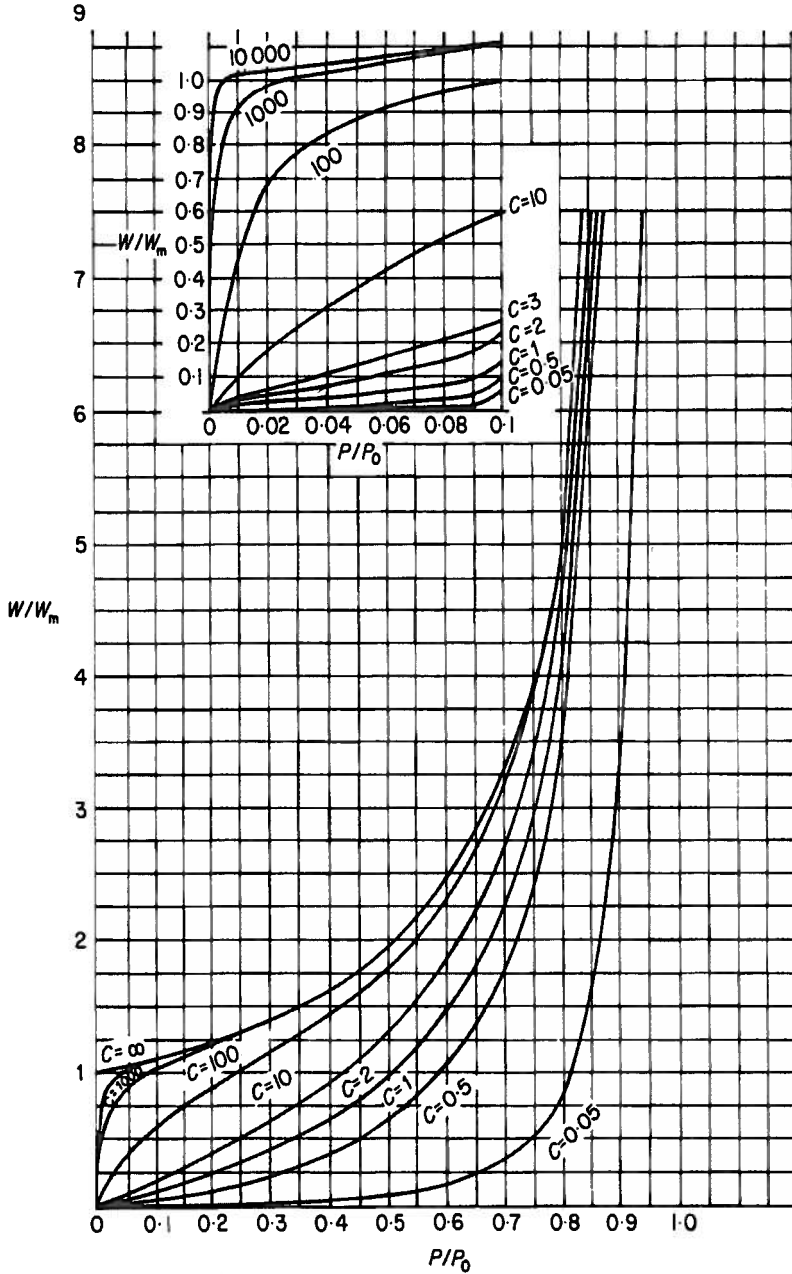


Figure 5.3 Isotherm shapes as a function of BET C values.

$$S_i = \frac{W_m \bar{N} A_x}{\bar{M}} \times 10^{-20} m^2 \quad (\text{cf. 4.13})$$

with W_m in grams, \bar{M} is the adsorbate molecular weight, \bar{N} is Avogadro's number (6.022×10^{23} molecules per mole) and A_x in square Ångströms per molecule. Division by the sample weight converts S_i to S , the specific surface area.

A reasonable approximation of the cross-sectional area of adsorbate molecules was proposed by Emmett and Brunauer [9]. They assumed the adsorbate molecules to be spherical and using the bulk liquid properties (at the temperature of the adsorption experiment) they calculated the cross-sectional area from

$$A_x = \left(\frac{\bar{V}}{\bar{N}} \right)^{\frac{2}{3}} \times 10^{16} \text{Å}^2 \quad (5.24)$$

where \bar{V} is the liquid molar volume. Equation (5.24) must be amended to reflect the molecular packing on the surface. Assuming that the liquid is structured as spheres with 12 nearest neighbors, 6 in a plane, in the usual close packed hexagonal arrangement shown in Fig. 6.1, and that the adsorbate has the same structure on the adsorbent surface, equation (5.24) becomes

$$A_x = 1.091 \left(\frac{\bar{V}}{\bar{N}} \right)^{\frac{2}{3}} \times 10^{16} \text{Å}^2 \quad (5.25)$$

The factor 1.091 in equation (5.25) arises from the characteristics of close packed hexagonal structures. If D is the distance between centers of adjacent spheres, the spacing between the centers of adjacent rows in a plane is $\sqrt{3} D/2$. The spacing between centers of adjacent planes is $\sqrt{2/3} D$ [10]. Allowing N_x and N_y to represent the number of spheres along the X and Y axes of a plane of spheres, the planar area, A_p , is given by

$$A_p = \frac{\sqrt{3}}{2} D^2 N_x N_y \quad (5.26)$$

If N_z is the number of planes or layers, then the volume, V , containing $N_x N_y N_z$ spheres is given by

$$V = \frac{\sqrt{3}}{2} \sqrt{\frac{2}{3}} D^3 N_x N_y N_z \quad (5.27)$$

Since $N_x N_y N_z$ represents the total number of spheres, N , in the volume, V , equation (5.27) can be expressed as

$$V = \frac{\sqrt{3}}{2} \sqrt{\frac{2}{3}} D^3 N \quad (5.28)$$

Then

$$\left(\frac{V}{N}\right)^{\frac{2}{3}} = \frac{3^{\frac{1}{3}}}{2^{\frac{2}{3}}} \left(\frac{2}{3}\right)^{\frac{1}{3}} D^2 \quad (5.29)$$

Substituting for D^2 into equation (5.26) gives

$$A_p = 1.091 N_x N_y \left(\frac{V}{N}\right)^{\frac{2}{3}} \quad (5.30)$$

The molecular cross-sectional area A_x then can be obtained by dividing the planar area, A_p , by $N_x N_y$, the number of molecules in a plane. Thus, dividing both numerator and denominator of the fraction, V/N , by the number of moles yields

$$A_x = 1.091 \left(\frac{\bar{V}}{\bar{N}}\right)^{\frac{2}{3}} \times 10^{16} \quad (\text{cf. 5.25})$$

That the adsorbate resides on the adsorbent surface with a structure similar to a plane of molecules within the bulk liquid, as depicted in Fig. 5.5 is a simplified view of the real situation on surfaces. Factors that make this model and therefore equation (5.25) of limited value include the following:

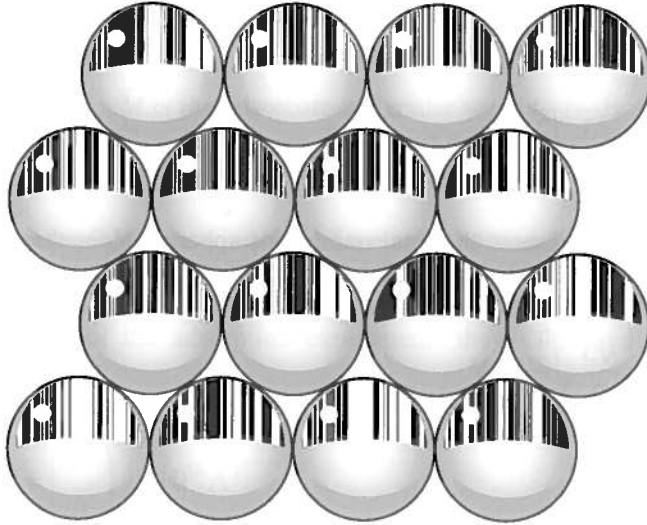


Figure 5.5 Sectional view of a close-packed hexagonal arrangement of spheres.

1. Weak interactions with the surface lead to lateral mobility of the adsorbate on the surface, which will tend to disrupt any tendency for the development of an organized structure, i.e., will prevent a definite arrangement of adsorbate on the surface.
2. Complex molecules, which rotate about several bond axes, can undergo conformational changes on various surfaces and thereby exhibit different cross-sectional areas.
3. Orientation of polar molecules produces different surface arrangements depending on the polarity of the adsorbent.
4. Strong interactions with the surface lead to localized adsorption, which constrains the adsorbate to a specific site. This type of 'epitaxial' adsorption will lead to decreasing measured surface areas relative to the true BET value as the surface sites become more widely spaced. The effective adsorbate cross-sectional area will then reflect the spacing between sites rather than the actual adsorbate dimensions.
5. Fine pores may not be accessible to the adsorbate, so that a substantial portion of the surface is inaccessible to measurement. This would be particularly true for large adsorbate molecules.

Based on the points discussed before it is obvious to assume a relationship between the BET C constant and the cross-sectional area. Indeed, Kiselev and Eltekov [11] established that the BET C value influences the adsorbate cross-sectional area. They measured the surface

area of a number of adsorbents using nitrogen. When the surface areas of the same adsorbents were measured using *n*-pentane as the adsorbate the cross-sectional areas of *n*-pentane had to be revised in order to match the surface areas measured using nitrogen. It was found that the revised areas increased hyperbolically as the *n*-pentane *C* value decreased, as show in Fig. 5.6.

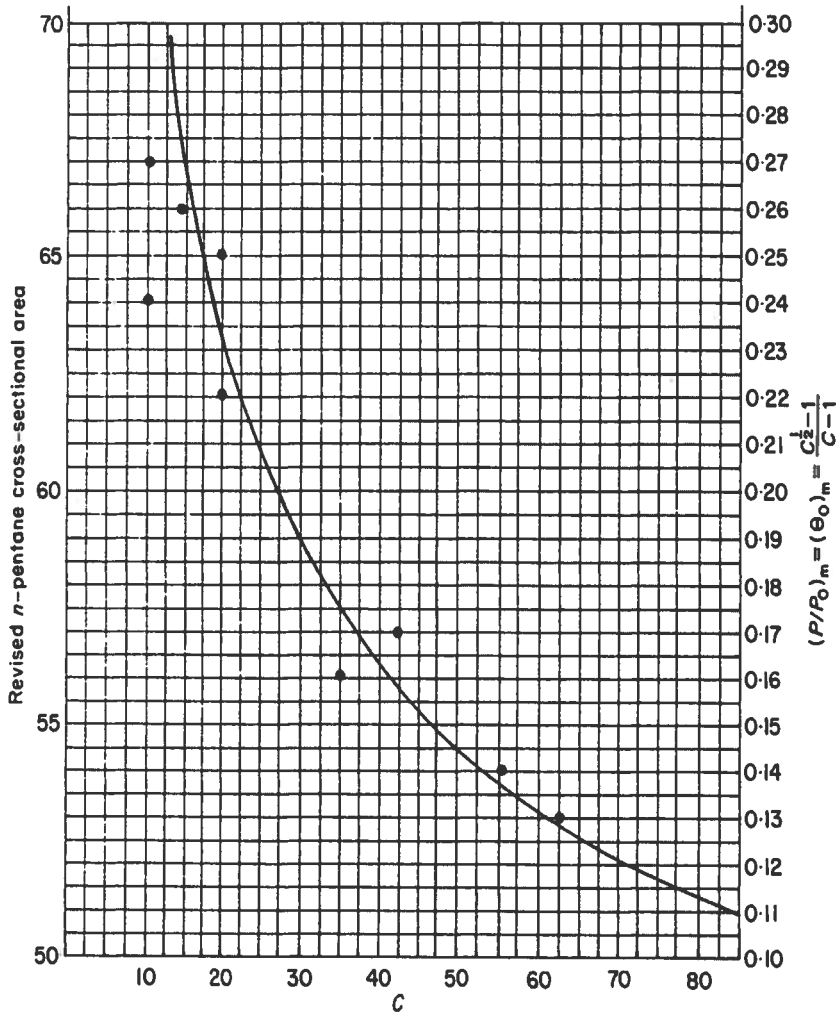


Figure 5.6 Variation of *n*-pentane cross-sectional area with the BET *C* constant (points) and $(\theta_0)_m$ (solid line).

A similar relationship between *n*-butane cross-sectional areas and the BET *C* constant has been reported [12]. A plot of the revised cross-sectional areas of *n*-butane versus the BET constant is shown in Fig. 5.7. Figs. 5.6 and 5.7 show that plots of $(\sqrt{C}-1)/(C-1)$ versus *C* give hyperbolae which also match the cross-sectional area data. A plausible explanation for the observation that the fraction of surface not covered by adsorbate, (θ_0), increases at low *C* values, leading to high apparent cross-sectional area, is that the two hydrocarbons used as adsorbates interact weakly with the adsorbent. Thus, they behave as two-dimensional gases on the surface. Therefore, their cross-sectional areas may reflect the area swept out by the adsorbate molecules during their residence time on the surface rather than their actual cross-sectional areas.

In those instances of very high *C* values, the fraction of surface uncovered by adsorbate again increases, as a result of epitaxial deposition on specific surface sites, which when widely spaced, would lead to high apparent cross-sectional areas. A complete plot of cross-sectional area versus the BET *C* value would then be parabolic in shape, with the most suitable values of cross-sectional areas lying near the minimum of the parabola. For the great majority of adsorbents, the *C* constant for nitrogen lies in the range from about 50 to 300. Interactions leading to *C* values as low as 10 or 20 are not found with nitrogen nor is nitrogen chemisorbed, which would lead to adsorption on specific sites. Thus, nitrogen is uniquely suited as a desirable adsorbate, since its *C* value is not found at the extremes at each end of the parabola.

Since $(\sqrt{C}-1)/(C-1) = (\theta_0)_m$ can be calculated from a BET plot, there exists a potential means of predicting the cross-sectional area variation relative to nitrogen. On surfaces that contain extensive porosity, which exclude large adsorbate molecules from some pores while admitting smaller ones, it becomes even more difficult to predict any variation in the adsorbate cross-sectional area by comparison to a standard [13,14].

Summarizing, it can be said that the effective cross-sectional area depends on the temperature, the nature of the adsorbate-adsorbate and adsorbent-adsorbate interaction and the texture of the adsorbent surface. The surface areas calculated from equation (4.13) usually give different results depending upon the adsorbate used. If the cross-sectional areas are arbitrarily revised to give surface area conformity on one sample, the revised values generally will not give surface area agreement when the adsorbent is changed. With regard to cross-sectional areas, it must be kept in mind that the area occupied by a molecule or atom can often be many times its true area and the terms *effective area* or *occupied area* are more appropriate and less misleading.

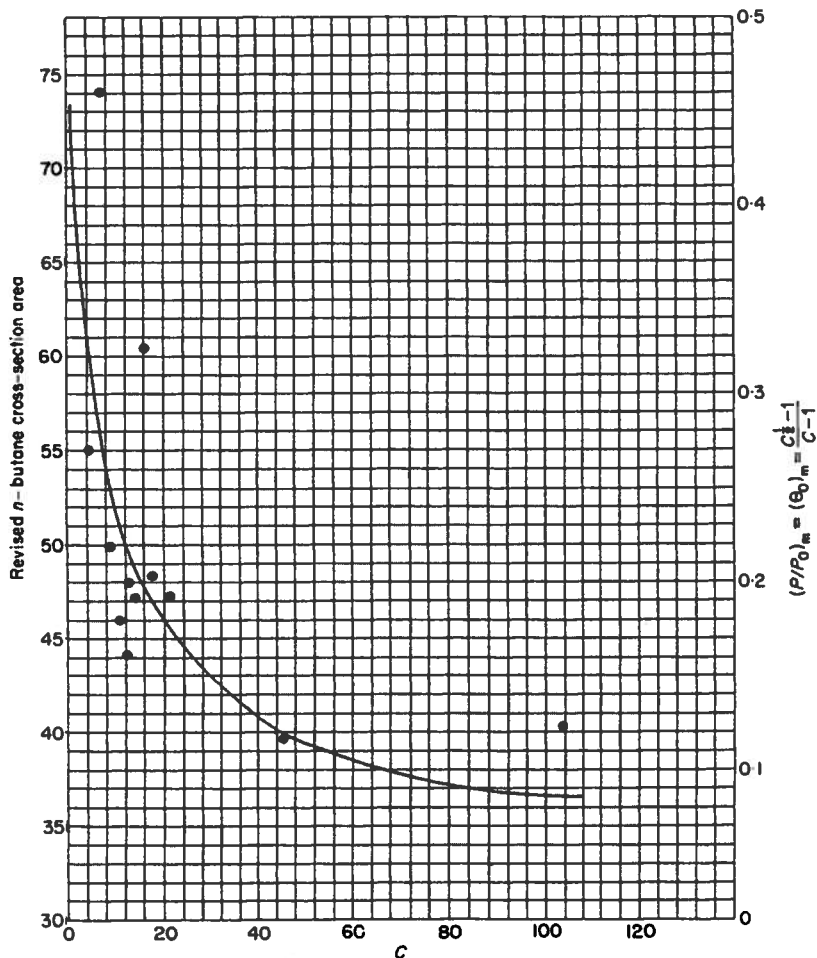


Figure 5.7 Variation of n-butane-cross-sectional area with the BET C constant (points) and $(\theta_0)_m$ (solid line).

Table 5.4 lists cross-sectional areas for some frequently used adsorptives. The data in the first column are taken from the work of McCellan and Harnsberger [15] who compared and discussed the cross-sectional areas reported for a wide range of adsorption systems. Very often the cross-sectional area was obtained by assigning a value to each adsorptive, as required, in order to make measured surface areas agree with the nitrogen value [16].

Table 5.4 Cross-sectional areas of some frequently used adsorptives.

Adsorptive Temperature	Cross-sectional area (\AA^2)[15]	Customary Value (\AA^2)
Nitrogen 77.35 K	13.0 - 20.0	16.2
Argon 77.35 K	10.0 - 19.0	13.8
Argon 87.27 K	9.7 - 18.5	14.2
Krypton 77.35 K	17.6 - 22.8	20.2
Xenon 77.35 K	6.5 - 29.9	16.8
Carbon Dioxide	14 - 22.0	
195 K		19.5
273 K		21.0
Oxygen 77.35 K	13 - 20	14.1
Water 298.15 K	6 - 19	12.5
n-Butane 273.15 K	36 - 54	44.4
Benzene 293.15 K	73 - 49	43.0

5.2.8 Nitrogen as the Standard Adsorptive for Surface Area Measurements

Due to the uncertainty in calculating absolute cross-sectional areas, the variation in cross-sectional areas with the BET C value, and the fact that on porous surfaces less area is available for larger adsorbate molecules, there is a need for a universal, although possibly arbitrary, standard adsorptive. The unique properties of nitrogen have led to its acceptance in this role with an assigned cross-sectional area of 16.2\AA^2 at its boiling point of 77.35 K. In addition the availability of liquid nitrogen, has also led to the situation that nitrogen is now internationally accepted as the standard BET adsorptive. This is demonstrated in the IUPAC recommendations [17], but also in numerous standards from international, and national standardization institutions (e.g., ISO, ASTM International).

The cross-sectional area of 16.2\AA^2 is based on the assumption that at 77 K the nitrogen monolayer is in a close-packed "liquid state", which appears to be quite accurate in the case for hydrocarbon surfaces. The fact, that nitrogen has a permanent quadrupole moment is important because it is responsible for the formation of a well-defined monolayer on most surfaces. However, in the case of surfaces of high polarity the nitrogen adsorption and the orientation of the adsorbate molecules on the surface is affected by specific interactions between the polar groups on the adsorbent surface and the quadrupole moment of the nitrogen molecule. The possibility of such a

problem was already mentioned in the paper by McClellan and Harnsberger [15]. Indeed, recent experimental sorption studies on highly ordered mesoporous silica materials such as MCM-41 (which consists of independent cylindrical-like pores), suggest strongly that the cross-sectional area of nitrogen on a hydroxylated surface might differ from the commonly adopted value of 0.162 nm^2 [18]. Similar observations were already made in the past and it was assumed that the quadrupole moment of the nitrogen molecule leads to specific interactions with the hydroxyl groups on the surface causing an orientating effect on the adsorbed nitrogen molecule [19]. But it was only in the last ten years that an accurate cross-sectional area, (i.e., 0.135 nm^2), valid for nitrogen adsorption on a hydroxylated silica surface, could be proposed [20]. This value was obtained by measuring the volume of N_2 adsorbed on silica spheres of known diameter. If one uses the standard cross-sectional area (0.162 nm^2) the BET surface area of hydroxylated silica surfaces can be overestimated by *ca.* 20 % [18].

In contrast to nitrogen, argon has no quadrupole moment and the above-mentioned problems do not occur when argon is used as the adsorptive. In contrast to argon adsorption at liquid argon temperature (i.e., 87.27 K), the use of argon adsorption at the liquid nitrogen temperature is more problematic. Firstly, argon is here *ca.* 6.5 K below the bulk triple point temperature ($T_r = 83.81 \text{ K}$), hence the bulk reference state is in doubt. However, for surface area analysis the saturation pressure of supercooled liquid argon ($P_0 = 230 \text{ torr}$) is used. In addition, argon sorption at 77 K is much more sensitive to the details of the surface structure, and type VI sorption isotherms (see chapter 3) have been observed on homogeneous surfaces [21].

5.2.9 Low Surface Area Analysis

Using highly accurate volumetric adsorption equipment, it is possible to measure absolute surface areas as low as approximately $0.5 - 1 \text{ m}^2$ with nitrogen as the adsorptive. In order to measure even lower surface areas the number of molecules trapped in the void volume of the sample cell needs to be reduced (see Chapter 14 for details). This can be achieved by applying krypton adsorption at liquid nitrogen temperature for the surface area analysis. Krypton at $\sim 77 \text{ K}$ is *ca.* 38.5 K below its triple point temperature ($T_r = 115.35 \text{ K}$), and it sublimates (i.e., $P_{0,\text{solid}}$) at *ca.* 1.6 torr. However, it has become customary to adopt the saturation pressure of supercooled liquid krypton for the application of the BET equation, i.e., one assumes that despite the fact that the sorption measurement is performed that far below the bulk triple point temperature, the adsorbed krypton layer is liquid-like. The saturation pressure of the supercooled liquid krypton is 2.63 torr, i.e., the number of molecules in the free space of the sample cell is significantly reduced (to $1/300^{\text{th}}$) compared to the conditions of nitrogen adsorption at liquid nitrogen temperature. Hence, krypton adsorption at $\sim 77 \text{ K}$ is much

COLORADO STATE

more sensitive, and can be applied to assess surface areas down to at least 0.05 m^2 .

Problems are of course associated with the fact that the nature and the thermodynamic state (solid or liquid?) of the adsorbed layer(s) is not well defined, and hence the reference state to calculate P/P_0 . Connected with this is some uncertainty with regard to the wetting behavior of the adsorbed krypton phase that far below the bulk triple point temperature (i.e., in the BET approach a complete wetting of the adsorbate phase is assumed). Whereas in the case of nitrogen adsorption (at its boiling temperature) for almost all materials a complete wetting behavior can be assumed, this situation may be different for of adsorption below the triple point temperature [21, 22]. This might also contribute to the fact that the effective cross-sectional area of krypton depends very much on the adsorbent surface and is therefore not well established.

The cross-sectional area calculated from the density of the supercooled liquid krypton is 0.152 nm^2 (15.2 \AA^2), but the higher cross-sectional area of 0.202 nm^2 (20.2 \AA^2) is commonly used [15, 23].

However, despite these deficiencies, it must be clearly stated that krypton adsorption at $\sim 77 \text{ K}$ is considered to be a very useful tool for routine surface area measurements of materials with low-surface area.

5.3 REFERENCES

1. Langmuir I. (1918) *J. Am. Chem.Soc.* **40**, 1368.
2. Brunauer S., Emmett P.H. and Teller E. (1938) *J. Amer. Chem. Soc.* **60**, 309.
3. Hill T.L. (1946) *J. Chem. Phys.* **14**, 268.
4. Lowell S. (1975) *Powder Technol.* **12**, 291.
5. Brunauer S., Copeland L.E. and Kantró D.L. (1967) *The Gas Solid Interface*, Vol. 1, Dekker, New York, chapter 3.
6. Brunauer S. (1961) *Solid Surfaces and the Gas Solid Interface*, Advances in Chemistry Series, No. 33, American Chemical Society, Washington, D.C.
7. MacIver D.S. and Emmett P.H. (1956) *J. Am. Chem. Soc.* **60**, 824.
8. Kruk M., Jaroniec M. and Sayari A. (1997) *J. Phys. Chem. B* **101**, 583.
9. Emmett P.H. and Brunauer S. (1937) *J. Am. Chem. Soc.* **59**, 1553.
10. Moelwyn-Hughes E.A. (1961) *Physical Chemistry*, 2nd edn, Pergamon Press, New York, p545.
11. Kiselev A.V. and Eltekov Y.A. (1957) *International Congress on Surface Activity II*, Butterworths, London, p228.
12. Lowell S., Shields J.E., Charalambous G. and Manzione J. (1982) *J. Colloid Interface Sci.* **86**, 191.
13. Harris B.L. and Emmett P.H. (1949) *J. Phys. Chem.* **53**, 811.
14. Davis R.T., DeWitt T.W. and Emmett P.H. (1947) *J. Phys. Chem.* **51**, 1232.
15. McClellan A.L. and Harnsberger H.F. (1967) *J. Colloid Interface Sci.* **23**, 577.
16. Livingston H.K. (1949) *J. Colloid Sci.* **4**, 450.
17. Rouquerol F., Rouquerol J. and Sing K.S.W. (1999) *Adsorption by Powders & Porous Solids*, Academic Press, London.
18. Galarneau A., Desplandier D., Dutartre R. and Di Renzo F. (1999) *Microporous-*

Mesoporous Mater. **27**, 297.

19. Rouquerol F., Rouquerol J., Peres C., Grillet Y. and Boudellal M. (1979) In *Characterization of Porous Solids* (Gregg S.J., Sing K.S.W. and Stoeckli H.F., eds.) The Society of Chemical Industry, Luton, UK, p107.
20. Jelinek L. and Kovats E.S. (1994) *Langmuir* **10**, 4225.
21. Dash J.G. (1975) *Films on Solid Surfaces*, Academic Press, New York.
22. Dominguez H., Allen M.P. and Evans R. (1998) *Mol. Phys.* **96**, 209.
23. Gregg S.J. and Sing K.S.W. (1982) *Adsorption, Surface Area, and Porosity*, 2nd edn, Academic Press, New York.

13 Physical Adsorption Measurement: Preliminaries

13.1 EXPERIMENTAL TECHNIQUES FOR PHYSICAL ADSORPTION MEASUREMENTS

The adsorbed amount as a function of pressure can be obtained by volumetric (manometric) and gravimetric methods, carrier gas and calorimetric techniques, nuclear resonance as well as by a combination of calorimetric and impedance spectroscopic measurements (for an overview see refs [1-3]). However, the most frequently used methods are the volumetric (manometric) and the gravimetric methods. The gravimetric method is based on a sensitive microbalance and a pressure gauge. The adsorbed amount can be measured directly, but a pressure dependent buoyancy correction is necessary. The gravimetric method is convenient to use for the study of adsorption not too far from room temperature. The adsorbent is not in direct contact with the thermostat and it is therefore more difficult to control and measure the exact temperature of the adsorbent at both high and cryogenic temperatures. Therefore, the volumetric method is recommended to measure the adsorption of nitrogen, argon and krypton at the temperatures of liquid nitrogen (77.35 K) and argon (87.27 K) [4].

The volumetric method is based on calibrated volumes and pressure measurements by applying the general gas equation. The adsorbed amount is calculated by determining the difference of the total amount of gas admitted to the sample cell with the adsorbent and the amount of gas in the free space. The void volume needs to be known very accurately. We discuss details with regard to this important matter in chapter 14.

Both volumetric and gravimetric methods allow adsorption to be measured under either static and quasi-equilibrium conditions. In quasi-equilibrium methods the adsorptive is continuously admitted to the sample at a certain, low rate. To obtain a scan of the desorption isotherm the pressure is continuously decreased. The most difficult point associated with the quasi-equilibrium procedure is that one needs to reach at any time of the experiment satisfactory equilibrium conditions. To check that equilibrium has been established the analysis should be repeated using slower gas rates (gas bleed rate). The validity of the analysis is strengthened if identical data are obtained at two different gas flows. If one can reach true equilibrium conditions, the main advantage of this method is that it provides isotherms of unsurpassed resolution. A detailed description of quasi-equilibrium

methods is given in refs. [5-7].

In contrast to this quasi-equilibrium method, the continuous flow method proposed by Nelson and Eggertson [8], gives rise to a discontinuous, point-by-point adsorption, as is the case for the volumetric static method. This flow method is based on a continuous flow of a mixture of a carrier gas (helium) and adsorptive (e.g., nitrogen) through the powder bed. The change in gas composition due to the adsorption of nitrogen is monitored by a thermal conductivity detector. The method is still frequently used for single point surface area measurements. Hence, we will discuss both the static volumetric- and the dynamic flow method in more detail later in this book (chapters 14 and 15), because these two methods are the most frequently used for the surface area and pore size characterization of porous solids.

13.2 REFERENCE STANDARDS

Adsorbents are usually characterized using parameters such as specific surface area, pore volume and the pore size distribution. These quantities can be derived by analysis of gas sorption isotherms by applying an appropriate theory used to treat the adsorption and/or desorption data.

However, the results obtained for the surface area, pore size etc. are dependent on the applied theoretical method for data analysis and, to some extent, on the chosen experimental method. In order to overcome these problems, the use of certified reference materials and standardized measurement procedures allow one to check and calibrate the performance of sorption analyzers and to compare results from different laboratories. More than twenty certified reference materials for surface area and pore size analysis are now available from the four internationally recognized standard authorities including BAM (Germany), IRRM (European Community), LGC (UK), and NIST (USA) [9]. These reference materials generally consist of powders of inert materials such as alumina, titania, silica/quartz, carbons and silicon nitrides.

Much work was done recently in standardizing measuring methods for the surface area and pore size characterization of porous solids. A comprehensive survey of standards on surface structure characterization can be found in the review of Robens *et al* [10]. Such standards are available from the national standardization organizations, but as a result of the globalization of research and industries, standardization is shifted more to the international organizations, e.g., ISO (International Organization for Standardization, ASTM International (American Society for Testing and Materials).

13.3 REPRESENTATIVE SAMPLES

Often, for the purposes of laboratory analysis, it is necessary to obtain a small quantity of powder from a larger batch. For maximum accuracy and reproducibility, it is necessary that the sample chosen be representative of the larger initial quantity. Here, the term representative means that the sample must possess the same particle and pore size distributions and specific surface area as the larger quantity from which it was obtained.

To some extent, under even slight agitation, particles tend to segregate with the finer ones settling toward the bottom of the container. When poured from a container into a conical pile, the smaller particles will collect towards the center. This behavior is caused by large particles rolling over the smaller ones and the small particles settling through the voids between the larger ones.

It is generally impossible to make a segregated sample completely homogeneous by shaking, tumbling or any other technique. Often these attempts only further enhance the segregation process. Devices such as the spinning or rotary riffler can be used to obtain representative samples. Rifflers operate on the principle that a sample need not be homogeneous in order to be representative.

Such a riffler (shown in Fig. 13.1) operates by loading the powder sample into a vibrating hopper, which delivers the sample down a chute into eight rotating collectors. Both the delivery and rotational rates can be controlled.

The sample, when loaded in the hopper, will be segregated. Therefore, at any depth ℓ there will exist a particle diameter gradient $\Delta D/\Delta \ell$. The powder settles as it is delivered to the collectors at the rate $\Delta \ell/\Delta t$. Then,

$$\frac{\Delta D}{\Delta \ell} \cdot \frac{\Delta \ell}{\Delta t} = \frac{\Delta D}{\Delta t} \quad (13.1)$$

which is the rate of change of particle diameters leaving the hopper. If ψ is defined as the change in particle diameter entering each collector per revolution, then,

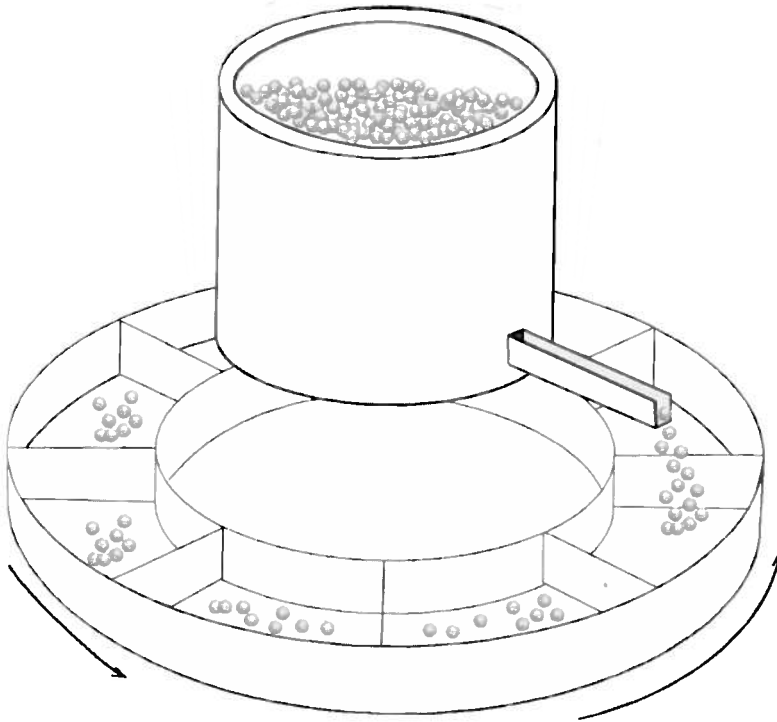


Figure 13.1 Schematic drawing of a spinning riffler.

$$\psi = \frac{1}{8} \frac{\Delta D}{\Delta t} \tau \quad (13.2)$$

where τ is the time per revolution. Substituting equation (13.1) into (13.2) gives

$$\psi = \frac{1}{8} \frac{\Delta D}{\Delta \ell} \cdot \frac{\Delta \ell}{\Delta t} \tau \quad (13.3)$$

Recognizing that $\Delta \ell / \Delta t$ is proportional to the feed rate, F , yields

$$\psi = K \frac{\Delta D}{\Delta \ell} F \tau \quad (13.4)$$

Equation (13.4) asserts that the change in particle diameter entering each collector can be made as small as necessary by decreasing the feed rate or

increasing the collector's rotational rate. However, Hatton [11] argues that it is preferable to slow the feed rate rather than increase the rotational rate to provide better representation.

When the entire sample has been delivered, each collector will contain powder exactly representative of the initial batch. Each collector will also contain a size gradient from top to bottom. Therefore, if the quantity required for analysis is less than the amount in any single collector, the process must be repeated. This is achieved by placing the contents of one collector back into the hopper and re-riffling. There are riffles available that can riffle samples of less than one gram to accommodate the need for small final samples.

Riffles can be equipped with an optional sieve that can be placed on top of the hopper to exclude particles above a required size. The advantage of this arrangement lies in the fact that a single particle of $100\ \mu\text{m}$ radius has the same weight as one million $1\ \mu\text{m}$ particles with only one-hundredth the surface area. If only a few of the large particles are present, they may not be properly represented in the final sample.

Often it is thought that the effectiveness of a riffler can be demonstrated by the uniformity of weight accumulated in each collector. This reasoning is incorrect if one considers that each collector will necessarily acquire a slightly different amount of sample if the collector diameters vary slightly. The only correct test for the effective performance of a riffler is to compare the contents of each collector in terms of particle size distribution or specific surface area.

Experiments with silica powder chosen from five depths in a two-pound container gave surface areas from top to bottom of 9.8, 10.2, 10.4, 10.5, and $10.7\ \text{m}^2/\text{g}$. When the same sample was poured into a conical pile, five random samples produced surface areas of 10.3, 11.0, 10.4, 10.0, and $10.6\ \text{m}^2/\text{g}$. However, when the sample was riffled in a spinning riffler with three size reductions, the subsequent analysis of the contents of five collectors gave 10.2, 10.1, 10.2, 10.2, and $10.1\ \text{m}^2/\text{g}$ as the specific surface area.

13.4 SAMPLE CONDITIONING: OUTGASSING OF THE ADSORBENT

In order to obtain correct data it is required to remove all physically adsorbed material from the adsorbent surface to ensure a reproducible initial state of the adsorbent surface, especially one in which pores are obstructed by foreign species. This can be accomplished by vacuum pumping or purging with an inert gas at elevated temperatures. Vacuum is attractive, because it prepares the surface under the same conditions that are required to start a static volumetric adsorption experiment (i.e., to start a such an

adsorption experiment the sample cell with adsorbent has to be evacuated). In addition, it also allows outgassing at lower temperatures than one would need if flow outgassing (purging) under atmospheric conditions were applied. A drawback of the vacuum method is certainly the problem of powder elutriation (see §13.5), which does not occur as readily in the flow method. An additional advantage of flow is that its setup is very easy (i.e., no expensive vacuum system is required).

The sample should be outgassed at the highest temperature that will not cause a structural change to the sample. In general, too low an outgassing temperature will cause lengthy preparation, and may result in lower than expected surface areas and pore volumes. In general, outgassing organics must be performed with care since most have quite low softening or glass transition points (e.g., magnesium stearate). In contrast, most carbon samples for instance can be outgassed quite safely at 573 K. Physisorbed water in nonporous or mesoporous materials will be lost at relatively low temperatures (< 473 K) under the influence of vacuum, but if adsorbed in narrow micropores, as they are present in some zeolites, high temperatures (up to 573 K) and long outgassing periods (often no less than 8 hours) are required. A special heating program is often needed, one which allows for a slow removal of most of the preadsorbed water at temperatures below 373 K accompanied by a stepwise increase in temperature until the final outgassing temperature is reached. This is done to avoid potential structural damage of the sample due to surface tension effects and so-called "steaming", i.e., hydrothermal alteration. In particular zeolites are sensitive to steaming, where the possibility of vaporization and re-condensation inside the pores can lead to structural changes.

In those instances where samples cannot be heated, the method of repetitive cycling [12] investigated by Lopez-Gonzales *et al* [13] can be utilized. They found that by repetitive adsorption and desorption the surface can be adequately cleaned to allow reproducible measurements. Usually three to six cycles are sufficient to produce a decontaminated surface. Presumably the process of desorption, as the sample temperature is raised, results in momentum exchange between the highly dense adsorbate leaving the surface and the contaminants. As the impurities are removed from the surface they will be carried out of the sample cell by the flowing gas. Thus the technique of repetitive cycling is an efficient means for removal of contaminants from the surface of a solid.

If the vacuum method is performed outgassing of the sample to a residual pressure of about 1 Pa (7.5×10^{-3} torr) to 0.01 Pa is considered to be satisfactory for most nonporous and mesoporous materials. This can be readily achieved by a combination of a rotary and diffusion pump in connection with a liquid nitrogen trap. The usual precautions, including a cold trap, should be taken to insure no contamination by the pump oil. However, as already mentioned, microporous materials such as zeolites

require an outgassing at much lower pressures, i.e., below 0.01 Pa. Nitrogen adsorption occurs here at relative pressures P/P_0 even below 10^{-7} for pores of diameter below ca. 6 Å. Hence, the sample should also be outgassed at these very low pressures. This can be achieved by using a turbomolecular pump which, if coupled with a diaphragm roughing pump, allows the sample to be outgassed in a completely oil free system.

13.5 ELUTRIATION AND ITS PREVENTION

Elutriation, or loss of powder out of the sample cell, is caused by gas flowing too rapidly out of the cell, and is in particular problematic for vacuum outgassing of materials such as the ones prepared by the sol-gel method.

Wider stems and sample cells with larger bulbs can be beneficial in reducing elutriation. Wider stems reduce the velocity of the gas leaving the cell when evacuation begins and thus it is less likely to entrain powder particles and transport them upwards and out of the cell. The presence of a filler rod significantly increases gas velocity because of the internal dimensions. Hence, outgassing should always be performed *without* a filler rod inserted into the sample cell. In problematic cases the analysis needs to be performed without a filler rod, but some loss of resolution and/or sensitivity may result (for more information about the proper choice of sample cells and filler rods etc. see also chapter 14.6).

In certain cases it might be required to pump down the sample very slowly by controlling (manually or in an automated way) the opening of the valve, which connects the sample cell to the vacuum line. Elutriation problems are also often encountered during degassing of damp, "light" powders. This condition can be reduced or eliminated by pre-drying the samples in a conventional drying oven and outgassing under vacuum at room temperature for some time before heating to the final temperature, where the outgassing of the sample should be ultimately performed.

In the most difficult cases, it might be necessary to insert a small glass wool plug (or a glass frit) into the cell stem, however this has the disadvantage that the quality of the vacuum surrounding the sample is no longer known.

13.6 REFERENCES

1. Keller J.U., Robens E. and du Fresne von Hohenesche C. (2002) *Stud. Surf. Sci. Catal.* **144**, 387.
2. Mikhail R.Sh. and Robens E. (1983) *Microstructure and Thermal Analysis of Solid Surfaces*, Wiley, Chichester.
3. Kaneko K., Ohba T., Hattori Y., Sunaga M., Tanaka H. and Kanoh H. (2002) *Stud. Surf. Sci. Catal.* **144**, 11.

4. Sing K.S.W., Everett D.H., Haul R.A.W., Mouscou L., Pierotti R.A., Rouquerol J and Siemieniewska T. (1985) *Pure Appl. Chem.* **57**, 603.
5. Rouquerol J., Rouquerol F., Grillet Y. and Ward R.J (1988) *Stud. Surf. Sci. Catal.* **39**, 67.
6. Rouquerol F., Rouquerol J. and Sing K.S.W. (1999) *Adsorption by Powders & Porous Solids*, Academic Press, London.
7. Rouquerol J. (1997) In *Physical Adsorption: Experiment, Theory and Applications*, (Fraissard J. and Conner C.W, eds.) Kluwer, Dordrecht, p17.
8. Nelson F.M. and Eggertsen F.T. (1958) *Anal. Chem.* **30**, 1387.
9. ^(a)BAM: Bundesanstalt für Materialforschung und –prüfung, Richard-Willstätter-Str. 11, D-12489 Berlin, Germany, www.bam.de; ^(b)NIST: National Institute of Standards and Technology, Gaithersburg, MD, USA, <http://ts.nist.gov/ts/htdocs/230/232/232.htm>; ^(c)LGC: LGC Promochem, Queens Rd, Teddington, Middlesex TW11 0LY, UK, www.lgcpromochem.com; ^(d)IRMM: Institute for Reference Materials and Measurements, Reference Materials Unit, attn BCR Sales, Retieseweg, B-2440 Geel, Belgium, www.irmm.jrc.be.
10. Robens E., Krebs K-F., Meyer K., Unger K.K. and Dabrowski A.(2002) *Colloids Surf. A: Physicochemical and Engineering Aspects*, 253.
11. Hatton T.A. (1978) *Powder Technol.* **19**, 227.
12. Harned H.S. (1920) *J. Am. Chem. Soc.* **42**, 372.
13. Lopez-Gonzales J. de D., Carpenter F.G. and Deitz V.R. (1955) *J. Res. Nat. Bur. Stand.* **55**, 11.

15 Dynamic Flow Method

15.1 NELSON AND EGGERTSEN CONTINUOUS FLOW METHOD

In 1951, Loebenstein and Deitz [1] described an innovative gas adsorption technique that did not require the use of a vacuum. They adsorbed nitrogen out of a mixture of nitrogen and helium that was passed back and forth over the sample between two burettes by raising and lowering attached mercury columns. Equilibrium was established by noting no further change in pressure with additional cycles. The quantity adsorbed was determined by the pressure decrease at constant volume. Successive data points were acquired by adding more nitrogen at the system. The results obtained by Loebenstein and Deitz agreed with vacuum volumetric measurements on a large variety of samples with a wide range of surface areas. They were also able to establish that the quantities of nitrogen adsorbed were independent of the presence of helium.

Nelson and Eggertsen [2], in 1958, extended the Loebenstein and Dietz technique by continuously flowing a mixture of helium and nitrogen through the powder bed. They used a hot wire thermal conductivity detector to sense the change in effluent gas composition during adsorption and desorption, when the sample cell was immersed into and removed from the bath, respectively. Fig. 15.1 illustrates a simplified continuous flow apparatus. Fig. 15.2 is a schematic of the flow path arrangement using a four-filament thermal conductivity bridge.

In Fig. 15.1, a mixture of adsorptive and carrier gas of known concentration is admitted into the apparatus at 'a'. Valve V_1 is used to control the flow rate. The analytical pressure is the partial pressure of the adsorptive component of the mixture. When the system has been purged, the detectors are zeroed by balancing the bridge (see Fig. 15.8). When the sample cell 'b' is immersed in the coolant, adsorption commences and detector D_B senses the decreased nitrogen concentration. Upon completion of adsorption, D_B again detects the same concentration as D_A and the signal returns to zero. When the coolant is removed, desorption occurs as the sample warms and detector D_B senses the increased nitrogen concentration. Upon completion of desorption, the detectors again sense the same concentration and the signal returns to its initial zero value. Wide tubes 'c' act as ballasts to (i) decrease the linear flow velocity of the gas ensuring its return to ambient temperature prior to entering D_B and (ii) to prevent air being drawn over D_B when the cell is cooled and the gas contracts.

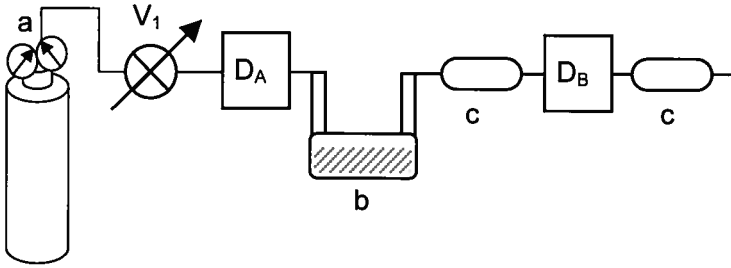


Figure 15.1 Simplified continuous flow apparatus

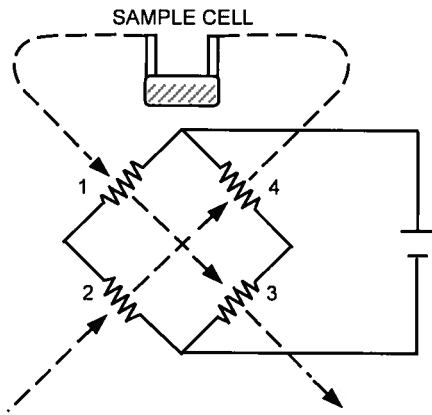


Figure 15.2 Gas flow path (dashed line) using a four-filament detector. D_A is formed by filaments 2 and 4, $D_B = 1$ and 3. This type of circuit is known as a Wheatstone bridge.

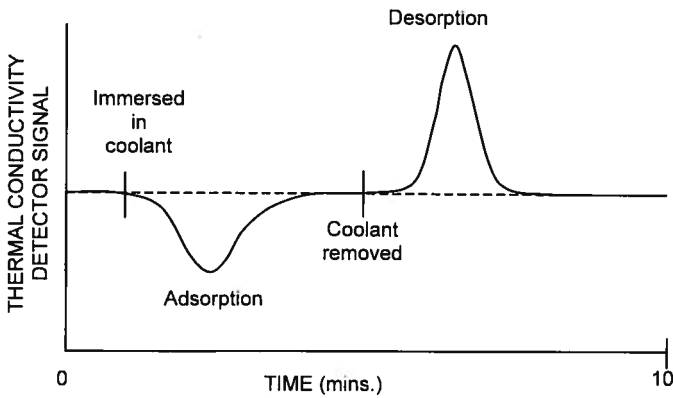


Figure 15.3 Adsorption and desorption peaks in a continuous flow apparatus.

Fig. 15.3 illustrates the detector signals due to adsorption and subsequent desorption. Figs. 15.4 and 15.5 illustrate a parallel flow arrangement which has the advantage of requiring shorter purge times when changing gas composition but is somewhat more wasteful of the mixed gases. The symbols shown in Fig. 15.4 have the same meaning as those used in Fig. 15.1.

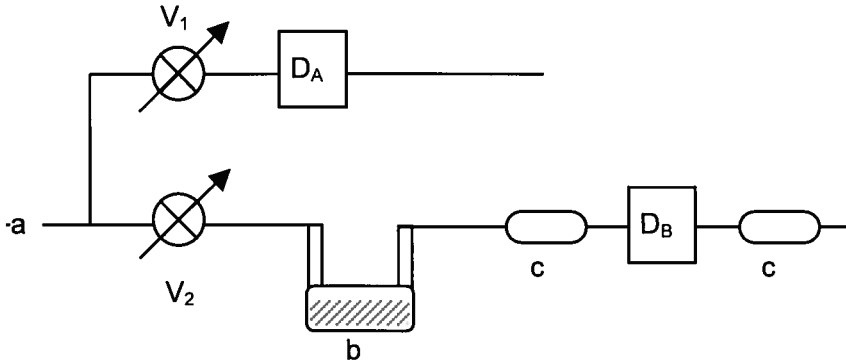


Figure 15.4 Parallel flow circuit.

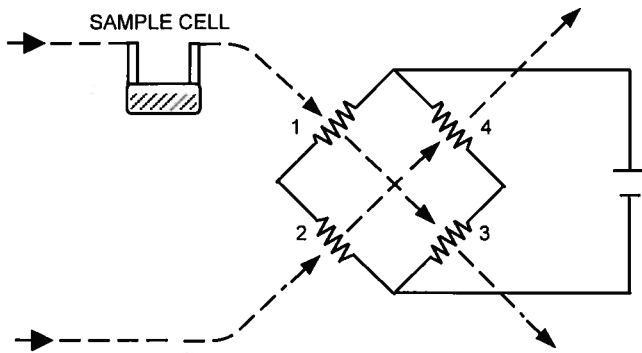


Figure 15.5 Parallel flow path using a four-filament bridge. D_A is formed by filaments 2 and 4 are, 1 and 3 comprise D_B . Dashed lines are gas flow paths.

15.2 CARRIER GAS (HELIUM) AND DETECTOR SENSITIVITY

To be effective, the carrier gas must fulfill two requirements. First, it cannot be adsorbed at the coolant temperature; second, it must possess a thermal conductivity sufficiently different from that of the adsorptive that small concentration changes can be detected. Usually helium is used as a carrier

gas; hence, some discussion regarding the possible influence of helium is necessary.

The forces leading to liquefaction and adsorption are the same in origin and magnitude. Gases substantially above their critical temperature, T_c , cannot be liquefied because their thermal energy is sufficient to overcome their intermolecular potential. Although the adsorption potential of a gas can be greater than the intermolecular potential, helium is, nevertheless, not adsorbed at liquid nitrogen temperature (~ 77 K) because this temperature is still more than 14 times the critical temperature of helium (~ 5.3 K).

Furthermore, in order to be considered adsorbed, a molecule must reside on the surface for a time τ at least as long as one vibrational cycle of the adsorbate normal to the surface. The time for one vibration is usually of the order of 10^{-13} seconds which, by equation (15.1), makes τ about 2×10^{-13} seconds at 77 K.

$$\tau = 10^{-13} \exp(100/RT) = 1.91 \times 10^{-13} \text{ sec} \quad (15.1)$$

The value of 100 cal/mol chosen for the adsorption energy of helium is consistent with the fact that helium has no dipole or quadrupole and is only slightly polarizable. Thus, it will minimally interact with any surface. Based upon reflections of a helium beam from LiF and NaCl cleaved surfaces, de Boer [3] estimated the adsorption energy to be less than 100 cal/mol. At 77K the velocity of a helium atom is 638 m/sec, so that in 1.91×10^{-13} sec it will travel $1.91 \times 10^{-13} \times 638 \times 10^{10} = 1.2 \text{ \AA}$. Thus, the condition that the adsorbate molecules reside near the surface for one vibrational cycle is fulfilled by the normal velocity of helium and not by virtue of its being adsorbed. Stated in alternate terms, the density of helium near a solid surface at 77 K is independent of the surface and is the same as the density remote from the surface. Molecular collisions with the adsorbed film by helium will certainly be no more destructive than collisions made by the adsorbate. In fact, helium collisions will be less disruptive of the adsorbed film structure since the velocity of helium is, on the average, 2.6 times greater than that of nitrogen at the same temperature, while a nitrogen molecule is 7 times heavier. Thus, the momentum exchange due to nitrogen collisions will be the more disruptive. The thermal energy of helium at 77 K is about 220 cal/mol. The heat of vaporization of nitrogen at 77 K is 1.335 kcal/mol, which may be taken as the minimum heat of adsorption. A complete exchange of thermal energy during collisions between a helium atom and an adsorbed nitrogen molecule would not be sufficient to cause desorption of the nitrogen.

To understand the effect of the carrier gas on the response of the thermal conductivity detector, consider the steady state condition that prevails when the resistive heat generated in the hot wire filament is exactly

balanced by the heat conducted away by the gas. This condition is described by equation (15.2)

$$i^2 R = ck(t_f - t_w) \quad (15.2)$$

where i is the filament current, R is the filament resistance, k is the thermal conductivity of the gas mixture, and t_f and t_w are the filament and the wall temperatures, respectively. The constant c is a cell constant that reflects the cell geometry and the separation of the filament from the wall, which acts as the heat sink.

When the gas composition is altered due to adsorption or desorption, the value of k changes by Δk , which in turn alters the filament temperature by Δt_f . Under the new conditions, equation (15.2) can be rewritten as

$$i^2 R = ck(k + \Delta k)(t_f + \Delta t_f - t_w) \quad (15.3)$$

Equating the right hand side of equations (15.2) and (15.3) gives

$$k(t_f - t_w) = (k + \Delta k)(t_f + \Delta t_f - t_w) \quad (15.4)$$

By neglecting the term $\Delta k \Delta t_f$, a second order effect, equation (15.4) rearranges to

$$\Delta t_f = \frac{\Delta k}{k}(t_w - t_f) \quad (15.5)$$

The change in filament resistance, ΔR , is directly proportional to the small temperature change Δt_f and is given by

$$\Delta R = \alpha R \Delta t_f \quad (15.6)$$

where α is the temperature coefficient of the filament, dependent on its composition, and R is the filament resistance at temperature t_f ; thus

$$\Delta R = \alpha R \frac{\Delta k}{k}(t_w - t_f) \quad (15.7)$$

Equation (15.7) requires that Δk be as large as possible for maximum response under a fixed set of operating conditions.

A fortunate set of circumstances leads to a situation in which the same molecular properties that impart minimal interactions or adsorption potentials also lead to the highest thermal conductivities. Molecules of large mass and many degrees of vibrational and rotational freedom tend to be more polarizable and possess dipoles and quadrupoles which give them higher boiling points and stronger interactions with surfaces. These same properties tend to reduce their effectiveness as thermal conductors.

Helium possesses only three degrees of translational freedom and hydrogen the same, plus two rotational and one vibrational degree. However, because of hydrogen's low weight, it has the highest thermal conductivity of all gases, followed by helium. Either of these two gases fulfills the requirement for adequately high thermal conductivities so that Δk in equation (15.7) will be sufficiently large to give good sensitivity with any adsorbate. Helium, however, is usually used in continuous flow analysis because of the hazards associated with hydrogen.

Fig. 15.6 is a plot of the thermal conductivity of mixtures of helium and nitrogen obtained on an apparatus similar to that described in the next section. Characteristically, the thermal conductivity of most mixtures does not vary linearly with concentration. The slope of the curve at any point determines the value of Δk and, therefore, the detector response. Fig. 15.6 also illustrates that the greater the difference between thermal conductivities of the adsorbate and carrier gas, the higher will be the slope and therefore the detector response.

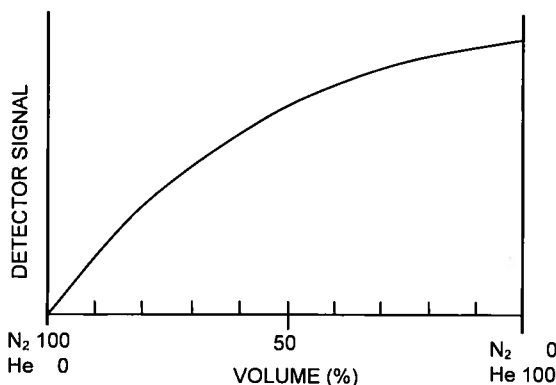


Figure 15.6 Thermal conductivity bridge response.

The shape of the curve shown in Fig. 15.6 is fortuitous in as far as the continuous flow method is concerned. For reasons to be discussed later, the desorption signal (see Fig. 15.3) is generally used to calculate the adsorbed volume. When, for example, 1.0 cm³ of nitrogen is desorbed into

9.0 cm³ of helium, the concentration change is 10%. However, when 1.0 cm³ of nitrogen is desorbed into 9.0 cm³ of a 90% nitrogen-in-helium mixture, the absolute change is only 1%. Therefore, the increase in slope at high nitrogen concentrations enables smaller concentration changes to be detected when data at high relative pressures are required.

Fig. 15.6 was prepared by flowing helium through one detector while varying the helium to nitrogen concentration ratio through the second detector.

15.3 DESIGN PARAMETERS FOR CONTINUOUS FLOW APPARATUS

The thermal conductivity (T.C.) detector consists of four filaments embedded in a stainless steel or brass block that acts as a heat sink. The T.C. detector is extremely sensitive to temperature changes and should be insulated to prevent temperature excursions during the time in which it takes to complete an adsorption or desorption measurement. Long-term thermal drift is not significant because of the calibration procedure discussed in the next section and, therefore, thermostating is not required. Fig. 15.7 shows a cross-sectional view of a T.C. block and the arrangement of the filaments relative to the flow path. The filaments shown are electrically connected, external to the block, and constitute one of the two detectors.

The filaments must be removed from the flow path, unlike the conventional 'flow over' type used in gas chromatography, because of the extreme flow variations encountered when the sample cell is cooled and subsequently warmed. Flow variations alter the steady state transport from the filaments, leaving them inadequate time to recover before the concentration change from adsorption to desorption is swept into the detector. When this occurs, the baseline from which the signal is measured will be unstable. By removing the filaments from the flow path and allowing diffusion to produce the signal, the problem of perturbing the filaments is completely solved. However, the tradeoff is nonlinear response characteristics. Since the thermal conductivity of the gas mixture is already non-linear with concentration, this additional nonlinearity poses no further problems, and is accommodated by calibration of signals (see §15.4).

A suitable electronic circuit provides power to the filaments and a means of zeroing or balancing the T.C. bridge, adjusting the filament current, attenuating the signal, and adjusting the polarity is shown in Fig. 15.8. Signals produced by adsorption or desorption can be fed to a data acquisition recorder for a continuous trace of the process, and/or to a digital integrator for summing the area under the adsorption and desorption curves.

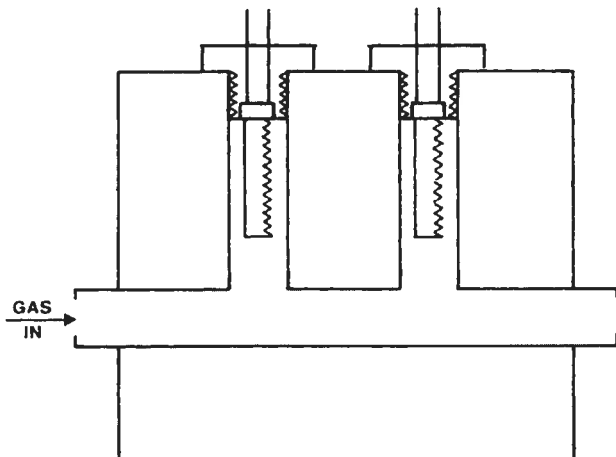


Figure 15.7 Thermal conductivity block with filaments located out of the flow path.

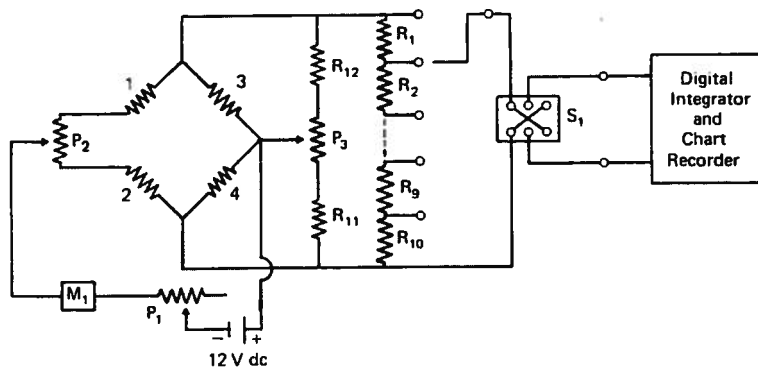


Figure 15.8 Thermal conductivity bridge electronic circuit. 12V dc power supply, stable to 1mV (ripple is not significant due to thermal lag of filaments); P_1 , 100 ohms for filament current control; M_1 milliammeter, 0-250 mA; P_2 , 2 ohms for coarse zero. Filaments 1 and 4 are detector 1, 2 and 3 are detector 2. P_3 , 1 ohm for fine zero; R_{11} , R_{12} , padding resistors ~64ohms; R_1 - R_{10} , attenuation resistors 1, 2, 4, ...512 ohms; S_1 (D.P.D.T.) switch for polarity. Attenuator resistors are $\frac{1}{4}$ % ww, lowest temperature coefficient; all others are 1%.

Fig. 15.9 is the flow schematic for a commercial continuous flow apparatus. Any one of up to four gas concentrations can be selected from from premixed tanks. Alternatively, adsorptive and carrier can be blended internally by controlling their flows with individual needle valves. A third choice is to feed mixtures to the apparatus from two linear mass flow controllers. Flow meters (operating under pressure to extend their range) indicate input flow rates. A flow meter at the very end of the flow path is

used to calibrate the flow meters. Pressure gauges indicate the input pressure under which the flow meters operate. An optional cold trap removes contaminants from the blended gas stream. After leaving the cold trap, but before flowing into detector D_A , the gas passes through a thermal equilibration tube that reduces the linear flow velocity and thereby provides time for warming back to ambient temperature.

After leaving D_A the flow splits, the larger flow goes to the sample cell at the analysis station, then to a second thermal equilibration tube and a flow meter used to indicate the flow through the sample cell. The smaller flow, controlled by its own needle valve merges with the sample cell effluent before entering detector D_B . The equilibration tubing downstream of D_B serves as a ballast to prevent air from entering D_B when the sample is immersed in the coolant. For high surface areas, the large quantities of desorbed gas can be diverted to a long path (far right). This prevents the gas from reaching the detector before the flow has returned to its original rate.

Splitting the flow as described above serves as a means of diluting the adsorption and desorption peaks in order provide infinitely variable signal height adjustment, in addition to using the stepwise electronic attenuator shown in Fig. 15.8.

A slow flow of adsorptive is directed to the 'out' septum and then to a sample cell positioned at the degas station. The gas flowing through this part of the circuit provides a both source of adsorptive for calibrating detector signals and as a purge for the degas station. Known quantities of adsorptive are injected into the analysis flow through the septum labeled 'in' to simulate a desorption signal for calibration purposes.

To measure the saturated vapor pressure, pure adsorptive is admitted to the P_0 station, when immersed in liquid nitrogen, until it liquefies. The equilibrium pressure is measured on the adjacent transducer.

A diverter valve at the analysis station ensures continuity of flow through the system even when the sample cell is removed.

In order to avoid contamination of the degassed sample when transferring from the degas station to the analysis station, the cells are mounted in spring-loaded self-sealing holders that close when disconnected and open when placed in position.

Sample cells consist of a wide variety of designs for various applications. Fig. 15.10 illustrates seven cells used for various types of samples. Their specific applications and limitations are given in more detail in Section 15.7. Each of the cells shown is made of Pyrex® glass. They are easily filled and cleaned. The cells range from four to five inches in length with stem inside and outside diameters of 0.15 and 0.24 inches, respectively.

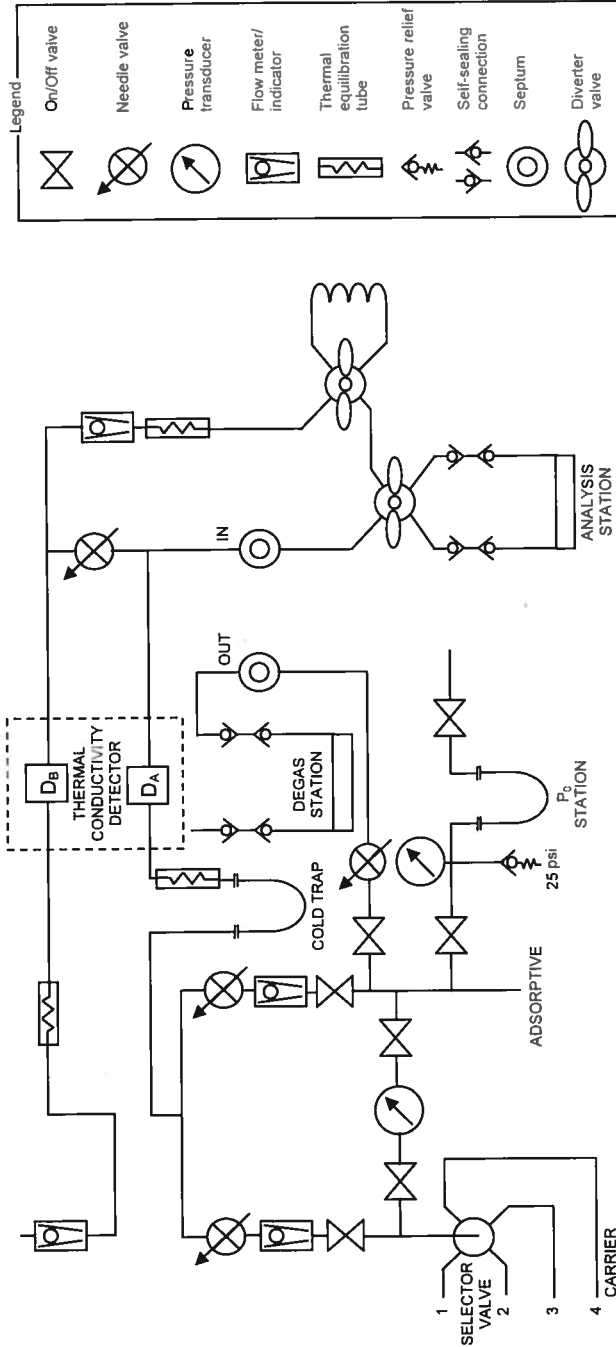


Figure 15.9 Flow diagram for a continuous flow system for adsorption measurements according to the Nelson-Eggertsen method. Not all commercial instruments are equipped with all the features shown.

15.4 SIGNALS AND SIGNAL CALIBRATION

The signal intensity created by an adsorption or desorption peak passing through the detector is dependent upon the attenuator setting, the filament current, and the design of the T.C. detector. Also, as stated previously, the detector response is nonlinear. These circumstances require that the adsorption or desorption signals be calibrated by introducing a volume of carrier or adsorbate gas into the flow stream. An expeditious and accurate method of calibration is the withdrawal of a sample of adsorbate from the 'out' septum (see Fig. 15.9) with a precision gas syringe and the injection of a known volume into the flow stream through the 'in' septum.

Usually the desorption peak is calibrated because it is free of tailing. By immersing the cell in a beaker of water immediately after removal from the liquid nitrogen, the rate of desorption is hastened. Heat transfer from the water is more rapid than from the air; therefore, a sharp desorption peak is generated. The calibration signal should be within 20% of the desorption signal height in order to reduce detector nonlinearity to a negligible effect.

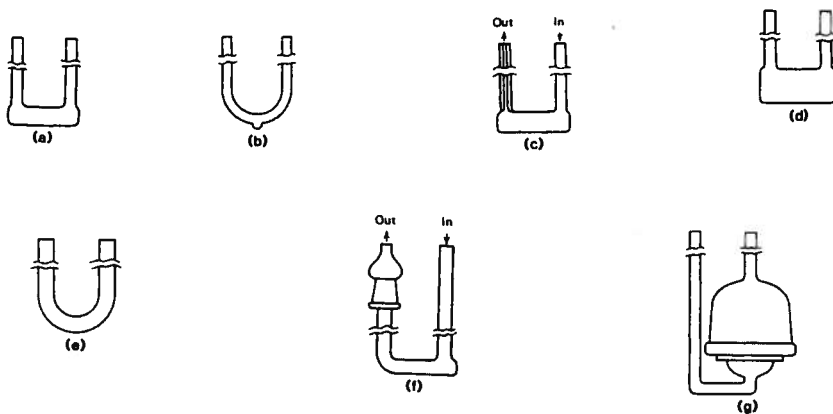


Figure 15.10 Sample cell designs (a) Conventional sample cell – for most powder samples with surface areas greater than 0.2 m^2 in the cell. For samples less than 0.2 m^2 , this cell can be used with krypton as the adsorbative. (b) Micro cell – used for very high surface area samples or for low area samples that exhibit thermal diffusion signals. Because of the small capacity of the micro cell, low area samples must be run on high sensitivity settings. (c) Capillary cell – useful for minimizing thermal diffusion signals. Because of the small capacity of the micro cell, low area samples must be run on high sensitivity settings. (d) Macro cell – used with krypton when a large quantity of low area sample is required. Also used for chemisorption when total uptake is small. (e) Large U-tube cell – for larger particles or bulk samples of high area with nitrogen or low area with krypton. (f) Pellet cell – used for pellets or tablets. High surface area with nitrogen or low area samples with krypton. (g) Monolith catalyst cell – for monolithic catalysts and other samples of wide diameter that must be measured as one piece.

The area under the desorption peak, A_d , and the area under the calibration peak, A_c , are used to calculate the volume, V_d , desorbed from the sample according to equation (15.8)

$$V_d = \frac{A_d}{A_c} V_c \quad (15.8)$$

where V_c is the volume of adsorptive injected. Equation (15.8) requires no correction for gas nonideality since the volume desorbed is measured at ambient temperature and pressure. Because desorption occurs at room temperature, it is complete and represents exactly the quantity adsorbed. For vapors adsorbed near room temperature, the sample can be heated to ensure complete desorption.

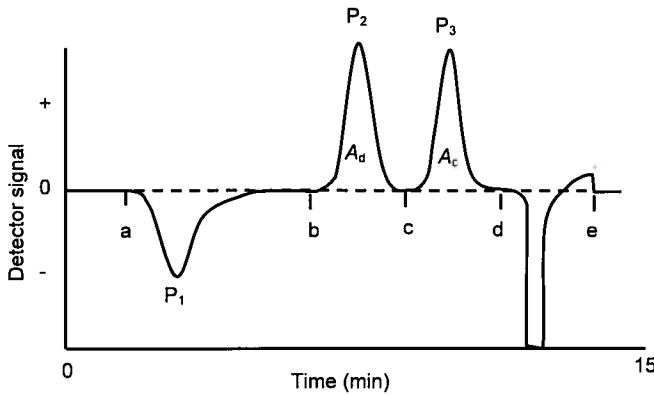


Figure 15.11 Complete cycle for one datum point.

A detailed analysis of the signal record, shown in Fig. 15.11, corresponding to a complete adsorption, desorption, calibration and concentration change cycle discloses that at point a, the sample cell is immersed in the coolant; this action produces the adsorption peak P_1 . Point b represents the removal of the coolant bath which leads to the desorption peak P_2 . The calibration peak P_3 results from the calibration injection made at point c. At d, a new gas concentration is admitted into the apparatus, which produces a steady base line at e where the detector is re-zeroed and the cycle repeated. The total time for a cycle is usually 15 minutes. Some timesavings can be achieved by combining the purge step (d-e) with the adsorption step (a-b). Familiarity with the apparatus usually allows the operator to choose the correct volume for calibration at particular attenuator and filament current settings or, alternatively, a calibration table can be prepared. If speed is essential, the flow rate can be increased to hasten the

cycle. However, this is at the risk of warming the adsorbent if excessive flow rates are used. Flow rates of 12-15 cm³/min allow ample time for the gas to equilibrate thermally before reaching the sample powder with all of the cells shown in Fig. 15.10. The presence of helium, with its high thermal conductivity, ensures rapid thermal equilibrium. Therefore, immersion depth of the cell is not critical provided that about 6-7cm (2½ inches) is in the coolant at the flow rates given previously.

Sample cells are not completely filled with powder; room is left above the surface for the unimpeded flow of gas. Although the gas flows over the powder bed and not through it, lower flow rates aid in ensuring against elutriation.

The areas under the adsorption and desorption peaks are usually not exactly the same. This observation is related to the changing slope of Fig. 15.6. Adsorption produces concentration changes to the right, in the direction of decreased sensitivity, while desorption produces signals in the direction of increased sensitivity.

If calibration of the adsorption signal is desired, it is necessary to inject a known quantity of helium. The amount of helium used to calibrate the adsorption signal will usually vary considerably from the amount of nitrogen required for the desorption calibration. This situation arises because, for example, if 1 cm³ of nitrogen is adsorbed out of a 10% flowing mixture, it will produce the equivalent of 9.0 cm³ of helium. Therefore, calibration of the adsorption signal will require nine times more helium than the corresponding volume of nitrogen needed to calibrate the desorption signal. If C_{N_2} and C_{He} are the concentrations of nitrogen and helium in the flow stream and if V_{He} is the volume of helium used for calibration, then the volume of nitrogen adsorbed, V_{ads} , is given by

$$V_{ads} = V_{He} \left(\frac{C_{N_2}}{C_{He}} \right) \left(\frac{A_{ads}}{A_{cal}} \right) \quad (15.9)$$

where A_{ads} and A_{cal} are the areas under the adsorption and calibration signals, respectively.

When small signals are generated, it is difficult to make accurate injections of the required small amounts of gas. Karp and Lowell [4] have offered a solution to this problem that involves the injection of larger volumes of adsorbate diluted with the carrier gas. When a volume containing a mixture of nitrogen and helium, V_{mix} , is injected into the flow stream, the equivalent volume of pure nitrogen, V_{N_2} , is given by

$$V_{N_2} = V_{\text{mix}} \left(\frac{X_{N_2} - X'_{N_2}}{X'_{He}} \right) \quad (15.10)$$

where X_{N_2} is the mole fraction of nitrogen in the calibration mixture and X'_{N_2} and X'_{He} are the mole fractions of nitrogen and helium in the flow stream.

The signals must propagate through the system at identical flow rates. Calibration at a flow rate other than the flow rate associated with the adsorption or desorption peaks can lead to serious errors because the width of the peaks and therefore the peak areas are directly proportional to the flow rate. A good two-stage pressure regulator and needle valve provide adequately constant flow rates over the short time required for desorption and calibration.

Precision gas calibrating syringes can be obtained in various size ranges with no more than 1% volumetric error. Constant stroke adapters provide a high degree of reproducibility. Often, in the BET range of relative pressures, the calibration volumes remain nearly constant because the increased volume adsorbed at higher relative pressures tends to be offset by the decrease in the detector sensitivity. Thus, the same syringe may be used for a wide range of calibrations, which results in the syringe error not effecting the BET slope and only slightly altering the intercept, which usually makes a small contribution to the surface area. A syringe error of 1% will produce an error in surface area far less than 1% for those BET plots with a slope greater than the intercept or for high C values.

15.5 ADSORPTION AND DESORPTION ISOTHERMS BY CONTINUOUS FLOW

To construct the adsorption isotherm, the adsorption, desorption, and calibration cycle shown in Fig. 15.11 is repeated for each datum point required. Errors are not cumulative since each point is independently determined. Relative pressures corresponding to each data point are established by measuring the saturated vapor pressure using any of the preceding methods or by adding 15 torr to ambient pressure. Thus, if X is the mole fraction of adsorbent in the flow stream, the relative pressure is given by

$$\frac{P}{P_0} = \frac{XP_a}{P_a + 15} \quad (15.11)$$

where P_a is ambient pressure in torr. At the recommended flow rates of 12-15 cm³/min, the flow impedance of the tubing does not raise the pressure in the sample cell.

The method used to construct the adsorption isotherm cannot be used to build the desorption isotherm. This is true because each data point on the adsorption curve reflects the amount adsorbed by a surface initially free of adsorbate. The desorption isotherm, however, must consist of data points indicating the amount desorbed from a surface that was previously saturated with adsorbate and subsequently equilibrated with adsorbate of the desired relative pressure. Karp *et al* [5] demonstrated that the desorption isotherm and hysteresis loop scans can be made in the following manner. First, the sample is exposed, while immersed in the coolant, to a flow of pure adsorbate. The flow is then changed to the desired concentration, leading to some desorption until the surface again equilibrates with the new concentration. The coolant is then removed and the resulting desorption signal is calibrated to give the volume adsorbed on the desorption isotherm. The above procedure is repeated for each datum point required, always starting with a surface first saturated with pure adsorbate.

To scan the hysteresis loop from the adsorption to the desorption isotherm, the sample, immersed in the coolant, is equilibrated with a gas mixture with a relative pressure corresponding to the start of the scan on the desorption isotherm. The adsorbate concentration is then reduced to a value corresponding to a relative pressure between the adsorption and desorption isotherms. When equilibrium is reached, as indicated by a constant detector signal, the coolant is removed and the resulting desorption signal is calibrated. Repetition of this procedure, each time using a slightly different relative pressure between the adsorption and desorption isotherms, yields a hysteresis scan from the adsorption to the desorption isotherm.

To scan from the desorption to the adsorption branch, pure adsorbate is first adsorbed, then the adsorbate concentration is reduced to a value giving a relative pressure corresponding to the start of the scan on the desorption isotherm. When equilibrium is established, as indicated by a constant base line, the adsorbate concentration is increased to give a relative pressure between the desorption and adsorption isotherms. After equilibrium is again established, coolant is removed and the resulting signal is calibrated to yield a data point between the desorption and adsorption isotherms. This procedure repeated, each time using a different final relative pressure, will yield a hysteresis loop scan from the desorption to the adsorption isotherm.

Figs. 15.12 and 15.13 illustrate the results obtained using the above method on a porous amorphous alumina sample. A distinct advantage of the flow system for these measurements is that data points can be obtained where they are desired and not where they happen to occur after dosing, as in the vacuum volumetric method. In addition, desorption isotherms and

hysteresis scans are generated with no error accumulation, void volume measurements, or nonideality corrections.

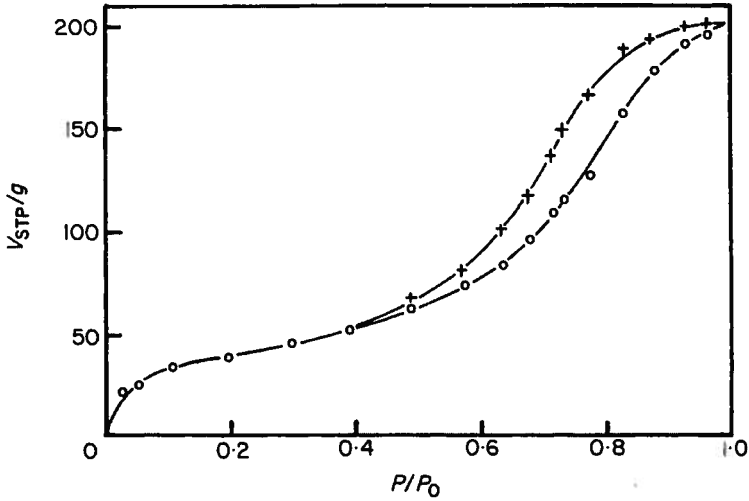


Figure 15.12 Adsorption and desorption isotherms of N_2 for 0.106 g sample of alumina
Adsorption \circ , Desorption $+$

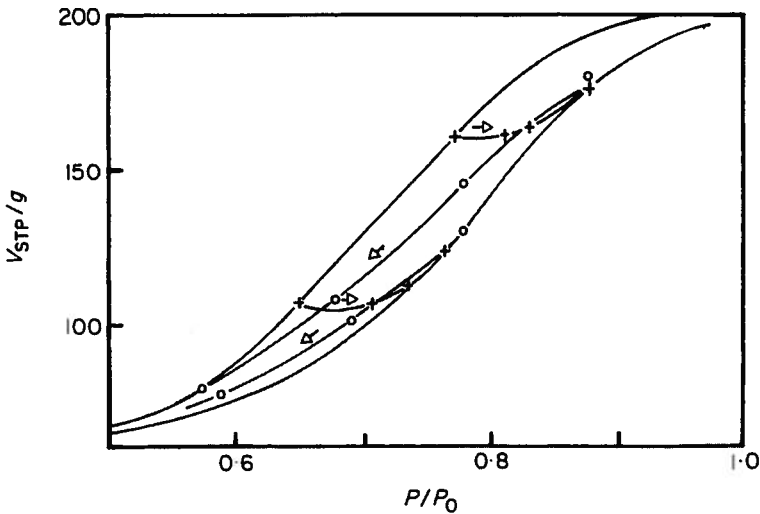


Figure 15.13 Hysteresis loop scan for same sample as Fig. 15.12. Adsorption \circ , Desorption $+$

15.6 LOW SURFACE AREA MEASUREMENTS

The thermal conductivity bridge and flow circuits shown in Figs. 15.8 and 15.9 are capable of producing a full-scale signal (1.0 mV) when 0.01 cm³ of nitrogen are desorbed into a 30% nitrogen and helium mixture. To achieve stable operating conditions at this sensitivity, the thermal conductivity block requires some time to equilibrate thermally and the system must be purged of any contaminants.

A desorbed volume of 0.001 cm³, using nitrogen as the adsorbate, will correspond to about 0.0028 m² (28 cm²) of surface area if a single adsorbed layer were formed. An equivalent statement is that 0.0028 m² is the surface area, measured by the single point method, on a sample which gives a high *C* value, if 0.001 cm³ were desorbed. Assuming that a signal 20% of full scale is sufficient to give reasonable accuracy for integration, then the lower limit for surface area measurement using hot wire detection is about 0.0006 m² or 6 cm². With the use of thermistor detectors, the lower limit would be still smaller.

Long before these extremely small areas can be measured with nitrogen, the phenomenon of thermal diffusion obscures the signals and imposes a higher lower limit [7]. Thermal diffusion results from the tendency of a gas mixture to separate when exposed to a changing temperature gradient. The sample cell is immersed partially into liquid nitrogen. Hence, when the gas mixture enters and leaves the sample cell it encounters a very sharp thermal gradient. This gradient exists along the arm of the tube for *ca.* 2 cm above and below the liquid level, and consequently gases will tend to separate. The extent of separation is proportional to the temperature gradient, the difference in the molecular weights of the two gases and their relative concentrations. The heavier gas tends to settle to the bottom of the cell and as its concentration builds up, a steady state is soon achieved and then the concentration of gas entering and leaving the cell is the same as it was initially. The build up of the heavier gas is only a fraction of a percent and even as low as a few parts per million. Therefore, it does not affect the quantities adsorbed in any measurable way.

However, when the bath is removed and the cell warms up the steady state is disturbed and the slight excess of heavier gas generates a signal followed by a signal due to the excess of lighter gas held up in the "in" arm of the cell. These signals are observed as a negative signal before or after the desorption signal and can generate errors in the integration of the desorption signal. This effect begins to manifest itself with nitrogen and helium mixtures when the total area in the cell is approximately 0.1 - 0.3 m²

In a static mixture of gases, the amount of thermal diffusion is a function of the time rate of change of the temperature gradient, the gas concentration, and the difference in masses of the molecules. In a flowing

gas mixture, in the presence of adsorption, it is difficult to assess the exact amount of thermal diffusion. Lowell and Karp [8] measured the effect of thermal diffusion on surface areas using the continuous flow method. Fig. 15.14 illustrates a fully developed anomalous desorption signal caused by thermal diffusion. As a result of the positive and negative nature of the signal, accurate integration of the true desorption peak is not possible.

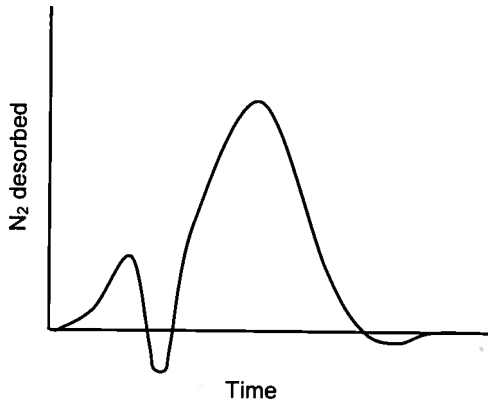










Figure 15.14 Signal shape from desorption of a small volume of nitrogen.

Table 15.1 shows the results of measuring the surface area of various quantities of zinc oxide using a conventional sample cell, Fig. 15.10a. When the same sample was analyzed using a micro cell, Fig. 15.10b, the results obtained were considerably improved, as shown in Table 15.2.

The onset of thermal diffusion depends on the gas concentrations, the sample surface area, the rate at which the sample cools to bath temperature, and the packing efficiency of the powder. In many instances, using a conventional sample cell, surface areas less than 0.1 m^2 can be accurately measured on well-packed samples that exhibit small interparticle void volume. The use of the micro cell (Fig. 15.10b) is predicated on the latter of these observations. Presumably, by decreasing the available volume into which the denser gas can settle, the effects of thermal diffusion can be minimized. Although small sample quantities are used with the micro cell, thermal conductivity detectors are sufficiently sensitive to give ample signal.

Another cell design that aids in minimizing the effects of thermal diffusion is the capillary cell, Fig. 15.10c. By using capillary tubing on the vent side of the cell, a sufficiently high linear flow velocity is maintained to prevent that arm from contributing to the problem. The large sample capacity of the capillary cell, compared to the micro cell, produces sufficient desorption signal to often make the thermal diffusion effect negligibly small.

Table 15.1 Data obtained using conventional cell (measured using the single-point BET method with 20% N₂ in He).

Weight	Actual area (m ²)	Measured area (m ²)	Deviation (%)	Signal shape at start of desorption peak
1.305	5.07	5.07	0	
0.739	2.87	2.87	0	
0.378	1.47	1.45	1.4	
0.177	0.678	0.686	-1.2	
0.089	0.345	0.327	5.2	
0.049	0.190	0.166	12.6	
0.0190	0.0730	0.0481	34.1	
0.0101	0.0394	0.0192	51.3	

Lowell [9] published a method to circumvent the problem of thermal diffusion by using an adsorbate with a low vapor pressure, such as krypton, at liquid nitrogen temperature. The coefficient of thermal diffusion $D(t)$ is given by [10]

$$D(t) = \frac{N_1/N_{tot} - N'_1/N_{tot}}{\ln T_1/T_2} \quad (15.12)$$

where N_1 and N'_1 are the adsorbate concentrations at the absolute temperatures T_2 and T_1 , respectively with $T_2 > T_1$. The term N_{tot} is the total molecular concentration of adsorbate and carrier gas. Because of krypton's low vapor pressure, its mole fraction in the BET range of relative pressures is of the order of 10^{-4} . This small value causes the difference between N_1/N_{tot} and N'_1/N_{tot} nearly to vanish, with the consequence that no obscuring thermal diffusion signals are generated.

Attempts to increase the size of nitrogen adsorption or desorption signals, by using larger sample cells, results in enhanced thermal diffusion signals due to the increased void volume into which the helium can settle. However, when krypton is used, no thermal diffusion effect is detectable in any of the sample cells shown in Fig. 15.10.

Table 15.2 Data obtained using U-tube cell.

Weight ZnO (g)	Actual Area (m ²)	Measured Area (m ²)*
0.0590	0.2280	0.2300
0.0270	0.1050	0.1020
0.0045	0.0175	0.0161

*This value is corrected by 15 cm² for the cell wall area, as estimated from the cell dimensions. Desorption peaks from an empty U-tube cell gave areas of 12- 17 cm².

The adsorption signals using krypton-helium mixtures are broad and shallow because the adsorption rate is limited by the low vapor pressure of krypton. The desorption signals are sharp and comparable to those obtained with nitrogen, since the rate of desorption is governed by the rate of heat transfer into the powder bed.

With krypton, the ability to use larger samples of low area powders facilitates measuring low surface areas because larger signals are generated in the absence of thermal diffusion. Also, as is true for nitrogen, krypton measurements do not require void volume evaluations or nonideality corrections, nor is thermal transpiration a factor as in the volumetric measurements.

15.7 DATA REDUCTION—CONTINUOUS FLOW

Table 15.3 can be used as a work sheet for calculating specific surface areas from continuous flow data. The data in the lower left corner are entered first and are used to calculate the other entries. In the example shown, nitrogen is the adsorbate.

Column 1 is the mole fraction of adsorbate in the flow stream. Column 2 is obtained as the product of P_a and column 1. Column 2, when divided by column 3, gives the relative pressure, which is entered in column 4 and from which columns 5 and 6 are calculated. Column 7 is the volume required to calibrate the desorption signal and column 8 is the corresponding weight of the calibration injection, calculated from the equation in the lower left side of the work sheet. The terms A_s and A_c are the areas under the signal and calibration peaks, respectively. Columns 11-13 are calculated from the

data in the previous columns. The data in column 13 are then plotted versus the corresponding relative pressures in column 5. The slope s and intercept i are calculated and the value of W_m is found as the reciprocal of their sum. Equation (4.13) is used to obtain the total sample surface area, S_t , and dividing by the sample weight yields the specific surface area, S .

15.8 SINGLE POINT METHOD

The assumption of a zero intercept reduces the BET equation to equation (5.3). This assumption is, of course, not realizable since it would require a BET C constant of infinity. Nevertheless, many samples possess sufficiently high C values to make the error associated with the single-point method acceptably small (see Chapter 5 and Table 5.2).

Using the zero intercept assumption, the BET equation can be written as

$$W_m = W \left(1 - \frac{P}{P_0} \right) \quad (\text{cf. 5.11})$$

from which the total surface area can be calculated by

$$S_t = W \left(1 - \frac{P}{P_0} \right) \frac{\bar{N}}{\bar{M}} A_x \quad (\text{cf. 5.12})$$

From the ideal gas equation of state

$$W = \frac{P_a V \bar{M}}{RT} \quad (15.13)$$

so that

$$S_t = \left(1 - \frac{P}{P_0} \right) \frac{P_a V \bar{N}}{RT} A_x \quad (15.14)$$

where P_a and T are the ambient pressure and absolute temperature, respectively, \bar{N} is Avogadro's number, A_x is the adsorbate cross-sectional area, and V is the volume adsorbed.

Table 15.3 Multipoint BET surface area data sheet.

Date: _____	Sample: <u>Titania</u>	Total Weight: <u>12.0434g</u>
Operator: _____	Outgas Procedure: <u>He purge, 1 hr., 150°C</u>	Tare: <u>11.3430g</u>
		Sample Weight: <u>0.7004g</u>

1	2	3	4	5	6	7	8	9	10	11	12	13	
X_{N_2}	P (torr)	P_0 (torr)	P/P_0	P/P_0	P_0/P	$(P_0/P) - 1$	V_c (cm^3)	W_c (g)	A_s	A_c	$W = \frac{A_s}{A_c} W_c$	$W[(P_0/P) - 1]$	1
0.050	37.68	768.6	0.0490	20.398	19.398	2.00	0.00230	1066	1083	0.00226	0.0438	22.81	
0.100	75.36	768.6	0.0980	10.199	9.199	2.20	0.00252	1078	1050	0.00259	0.0238	41.97	
0.200	150.7	768.6	0.1961	5.096	4.096	2.50	0.00287	1168	1098	0.00305	0.0125	80.05	
0.2995	225.7	768.6	0.2937	3.405	2.405	2.60	0.00298	1031	879	0.00350	0.0084	118.80	

Ambient pressure, $P_a = \underline{753.6}$ mm Hg
 Vapor pressure, $P_0 = \underline{768.6}$ mm Hg
 Ambient temperature, $T = \underline{295}$ K
 Adsorbate molecular weight, $\bar{M} = \underline{28.01}$
 Adsorbate area, $A_s = \underline{16.2 \times 10^{20}}$ m^2
 Calibration gas weight, $W_c = \frac{P_a \bar{M} V_c}{(6.235 \times 10^4) T}$

Plot $\frac{1}{W[(P_0/P) - 1]}$ vs. P/P_0
 Slope, $s = \underline{391.9}$
 Intercept, $i = \underline{3.52}$
 $W_m = \frac{1}{s+i}$
 $W_m = \underline{0.00253}$ g

Total surface area,
 $S_t = \frac{W_m (6.023 \times 10^{23}) A_c}{\bar{M}}$
 $S_t = \underline{8.81}$ m^2
 $S = S_t/W$
 $S = \underline{12.58}$ m^2/g

Using nitrogen as the adsorptive at a concentration of 0.3 mole fraction and assuming P_0 is 15 torr above ambient pressure, equation (15.14) can be expressed as

$$S_t = W \left(1 - \frac{0.3P_a}{P_a + 15} \right) \frac{P_a V \bar{N}}{RT} A_x \quad (15.15)$$

Assuming the ambient pressure P_a is 760 Torr and ambient temperature T is 295 K, equation (15.15) reduces to

$$S_t = 2.84V (\text{m}^2) \quad (15.16)$$

Thus, the total surface area contained in the sample cell is given by the simple linear relationship above when V is in cubic centimeters. By calibrating the desorption signal, A_{des} , with a known volume of nitrogen, V_{cal} , equation (15.16) can be rewritten as

$$S_t = 2.84 \frac{A_{des}}{A_{cal}} V_{cal} \quad (15.17)$$

where A_{des} and A_{cal} are the integrated areas under the desorption and calibration signals, respectively.

Modern commercial single point instruments contain a linearization network that corrects for the hot wire nonlinearity. This procedure allows a built-in digital integrator to integrate the signals linearly so that the surface area is given directly on a digital display. An advantage is that the analysis time for a BET surface area determination is extremely short, usually less than ten minutes [10].

15.9 REFERENCES

1. Loebenstein W.V. and Deitz V.R. (1951) *J. Res. Nat. Bur. Stand.* **46**, 51.
2. Nelson F.M. and Eggertsen F.T. (1958) *Anal. Chem.* **30**, 1387.
3. de Boer J.H. (1953) *The Dynamical Character of Adsorption*, Oxford University Press, London, p33.
4. Karp S. and Lowell S. (1971) *Anal. Chem.* **43**, 1910.
5. Karp S., Lowell S. and Mustacuiolo A. (1972) *Anal. Chem.* **44**, 2395.
6. Kourilova D. and Krevel M. (1972) *J. Chromat.* **65**, 71.
7. Lowell S. and Karp S. (1972) *Anal. Chem.* **44**, 1706.
8. Lowell S. (1973) *Anal. Chem.* **45**, 8.
9. Benson S.W. (1960) *The Foundation of Chemical Kinetics*, McGraw-Hill, New York, p188.
10. Quantachrome Instruments, Boynton Beach, FL.